*LA-12876-T*
*Thesis*

# *Engineered Materials for Application in Severe Metallurgical Environments: Tantalum–Carbon Alloy Development*

**Los Alamos**
NATIONAL LABORATORY

*Los Alamos National Laboratory is operated by the University of California for the United States Department of Energy under contract W-7405-ENG-36.*

*This report is based on a thesis that was accepted by the Materials Science Interdisciplinary Graduate Program, Colorado School of Mines, Golden, Colorado, in partial fulfillment of the requirements for the degree of Doctor of Philosophy in Materials Science. It is the independent work of the author and has not been edited by the CIC-1 Writing and Editing staff.*

LA-12876-T
Thesis

UC-704
Issued: February 1995

# *Engineered Materials for Application in Severe Metallurgical Environments: Tantalum–Carbon Alloy Development*

*Keith M. Axler, NMT-6, MS E510*

MASTER

Los Alamos
NATIONAL LABORATORY
Los Alamos, New Mexico 87545

# ABSTRACT

A suite of investigations has been completed to develop and demonstrate a construction material for use in severely corrosive metallurgical processing environments. The material is a tantalum-base alloy with inclusions of $Ta_2C$. Alloy development work involved multi-step thermal processing to invoke specific microstructural features. The kinetics of carbide formation from supersaturated solid solutions of carbon in tantalum were established. Performance evaluation of the alloy was conducted and the alloy has been demonstrated to outperform any previously studied metallic construction material used in pyrometallurgical processing of plutonium.

Specific microstructural features of the alloy have been identified which provide the extreme corrosion resistance. Grain boundary occupancy by the $Ta_2C$ phase is associated with the corrosion resistance to liquid metal. Precipitation from the supersaturated condition invokes a microstructure with the most significant grain boundary delineation by carbide inclusions and hence provides the most corrosion resistant attributes.

It has been experimentally proven that the precipitate growth rate is not dictated solely by the diffusion rate of the interstitial species and is more complex. The observed growth rate of carbide precipitates involves several competing effects.

An expression which describes precipitate growth within the grain boundary is presented:

$$W = \frac{\Delta X_o}{(X_b - X_e)} \sqrt{t \cdot 0.0337\, e^{-51300/RT}}$$

where W is the width of the precipitate, $\Delta X_o$ is the degree of supersaturation, $X_b$ is the mole fraction carbon in the precipitating phase, and $X_e$ is the equilibrium carbon mole fraction in the matrix at the aging (precipitation) temperature.

The engineered material investigated in this work has exceptional corrosion resistance to liquid metals due to occupancy of grain boundary regions by the extremely refractory phase $Ta_2C$. It has also been shown to possess enhanced corrosion resistance to high temperature chlorine. The plutonium operations in which this material has performed are among the most corrosive metallurgical processing environments. The demonstration of this material in the current study has illustrated its applicability for general use in high-temperature processing operations involving liquid metals and molten salts.

## TABLE OF CONTENTS

## LIST OF FIGURES

# LIST OF TABLES

# 1.0 INTRODUCTION

Traditional construction materials used in pyrometallurgical processing are limited by their interactions with the process environments. Materials' interactions generate interfering species and reduce product quality. In addition, corrosion of materials used in the construction of furnace hardware leads to failed processing runs.

This project was undertaken to identify, develop, and demonstrate an alternative construction material for service in plutonium pyrochemical operations. Evaluation of the processes was undertaken to define the specific attributes required in a viable candidate material. The reactive substances in the service environments established the criteria for thermodynamic stability and defined specific microstructural properties for corrosion resistance.

A successful alternative material has been demonstrated. The material consists of $Ta_2C$ inclusions within a tantalum-based matrix. A technique for the production of this material has been refined and its performance in pyrometallurgical environments has been extensively characterized. The material is formed by precipitation of $Ta_2C$ from supersaturated solid solutions of carbon in tantalum.

A detailed description of issues relevant to the selection of construction materials has been provided. Specific issues which established the criteria of performance are detailed. Results are presented on the performance testing and evaluation of the selected construction material.

In addition, information from the testing and evaluation of other carbon-tantalum alloys is presented.

This work also includes investigations of tantalum-carbon phase behavior and a quantitative treatment of carbon-tantalum alloy development on the microstructural level. The growth rate of the carbide inclusions from supersaturated solid solutions of carbon in tantalum has been quantitatively characterized. Through experimental investigations of carbide formation kinetics, processing parameters for the production of specific microstructural features within the selected material have been established.

## 2.0 DESCRIPTION OF PROBLEM ADDRESSED BY THE RESEARCH

An understanding of the thermodynamic properties and mechanical features of conventional pyrometallurgical hardware is necessary to realize the criteria for a viable alternative construction material. A description of specific limitations in traditional construction materials has been provided in prelude to a detailed description of the alloy development conducted within this investigation.

Traditional construction materials, such as metallic furnace hardware and ceramic crucibles, are not completely inert within the pyrochemical environments. This factor is reflected in the appearance of interfering species due to materials interactions which reduce process yields and inhibit product recovery. Construction materials include both metallic components such as tantalum or tantalum alloys, and ceramic bodies, typically MgO-based. These materials are contacted with liquid metals (calcium and plutonium in the present cases), molten halide salts, and reactive gases such as oxygen and chlorine.

Several processes can benefit from alternate construction materials for hardware and containment vessels. The alternate materials must provide extended service and remain inert within the pyrochemical environments. The requirements of the candidate materials are dictated by the service environment: high temperature exposures to liquid metals, molten salts, and corrosive gasses. In addition, viable candidate materials must withstand multiple thermal cycles.

Metallic hardware components used in pyrometallurgical processing provide limited service life due to the severe processing environments. Corrosion-induced failure of furnace components leads to unsuccessful termination of batch processes and the generation of radioactive waste. This research has included a campaign of postmortem examinations of pyrochemical hardware which failed in service to elucidate the deleterious materials interactions. The results of these failure analyses have established the effective corrosion mechanisms and subsequently defined the criteria for the candidate alternative construction materials.

The main-line pyrometallurgical plutonium processing operations are briefly described here to illustrate the service environments presented to the construction materials. Due to classification issues, specific operating parameters and identification of materials used in certain applications were not included in the following descriptions.

1) Multi-Cycle Direct Oxide Reduction (MCDOR): The conversion of $PuO_2$ to metal via reduction of the oxide with metallic calcium. The reaction proceeds within a flux of molten $CaCl_2$ which exhibits a solubility for the CaO reaction product. As CaO is generated insitu, it is removed from the reaction site into the salt flux. This is performed in a semi-continuous fashion with salt regenerations performed between incremental additions of metallic calcium and $PuO_2$. The salt regeneration involves delivery of chlorine gas into the molten salt system at elevated temperatures to convert CaO to $CaCl_2$ and provide a "clean" salt flux for dissolution of CaO formed in subsequent reduction steps. The conversion of CaO to $CaCl_2$ increases the total salt volume.

The limiting number of reduction/regeneration cycles corresponds to the maximum volume of the vessel. When the vessel is full, the run is terminated. Due to the brittle nature of the ceramic vessels, they must be broken open to recover the product materials. The discarded crucibles contribute to the volumes of radioactive processing waste.

In addition to the large containment vessel, the operation involves the use of a stirrer and gas delivery lance. The construction materials are exposed to molten salts, liquid plutonium and calcium, and high-temperature chlorine and oxygen. Corrosion induced failure of these hardware components also contributes to the generation of radioactive waste.

2) Molten Salt Extraction (MSE): The removal of americium from plutonium metal. The radioactive decay scheme for plutonium generates the daughter product americium. The in-growth of americium affects the shelf life of plutonium parts in the nuclear stockpile. Americium must be removed because it may effect plutonium phase stability and because of its high-energy neutron emission. MSE involves contacting molten plutonium with salt solutions containing $PuCl_3$ which is reduced by metallic americium. The subsequently formed americium chloride reports to the salt solution phase and the metallic plutonium reaction product liquates to the lower metal phase.

The reacted plutonium metal phase is recovered as a solidified button product which is then either cast into shape for service, or submitted for further purification by electrolysis. A crucible and stirrer are present in the system which are exposed to the liquid metal and salt.

3) Electrorefining (ER): This is the final purification step for weapons-grade plutonium. This operation involves the contact of molten plutonium with an electrolyte salt phase ($CaCl_2$ or an equimolar solution of KCl-NaCl). An anodic electrode is placed into the molten metal pool. The plutonium as the +3 ion migrates through the salt and is reduced at a cathodic metal surface. The metal drains from the electrode surface into a vessel where it is collected in a critically safe geometry. The metal accumulated after drainage from the cathodic surface is of high purity as the bulk of metallic impurities are retained at the anode. The electrolysis is terminated when the anode heal becomes highly concentrated in impurity elements. In addition to the containment vessels and stirrers, the cell contains electrodes, insulating sheaths, electrode support rods, transfer funnels, and ancillary fixtures. This is the most hardware-intensive operation with all the materials being exposed to the severe chemical system of molten salts, liquid plutonium, and sodium vapor/condensate which is a by-product of salt interactions.

4) Casting: The purified plutonium is finally cast into near-net shapes for service. This is conducted under vacuum by radio-frequency induction heating. The casting is conducted by a bottom-pour furnace which is remote controlled. The furnace crucible and the drain valve are exposed to the liquid metal. The extreme reactivity of the liquid metals induces short service lives for these metallic components. Any materials interactions at this stage of processing are extremely deleterious to ultimate product quality since the purification steps occur earlier on in the process scheme.

Reflected light images are presented herein to illustrate the corrosive effects of liquid plutonium on tantalum hardware during metallurgical processing. The photomicrographs in Figure 1 show the grain structure of a tantalum hardware component prior to service usage. The micrographs in Figure 2 reveal the same material after a corrosion-induced failure during the electrolytic purification of plutonium.

The removal of grain boundary material is illustrated by the presence of the plutonium (darker, intergranular regions). The plutonium migrated into the structure at the elevated service temperatures and is present as solidified tributaries between the tantalum grains. Within the most severe corrosion regions, the morphology of the tantalum grains is preserved, yet the grain boundary material is extensively removed. The retention of faceted grains throughout the reaction zone indicates an intragranular corrosion mechanism. This is generally associated with exposures to highly reactive liquid metals.

Figure 1. Reflected light photomicrographs of tantalum metal used in the fabrication of pyrometallurgical hardware.

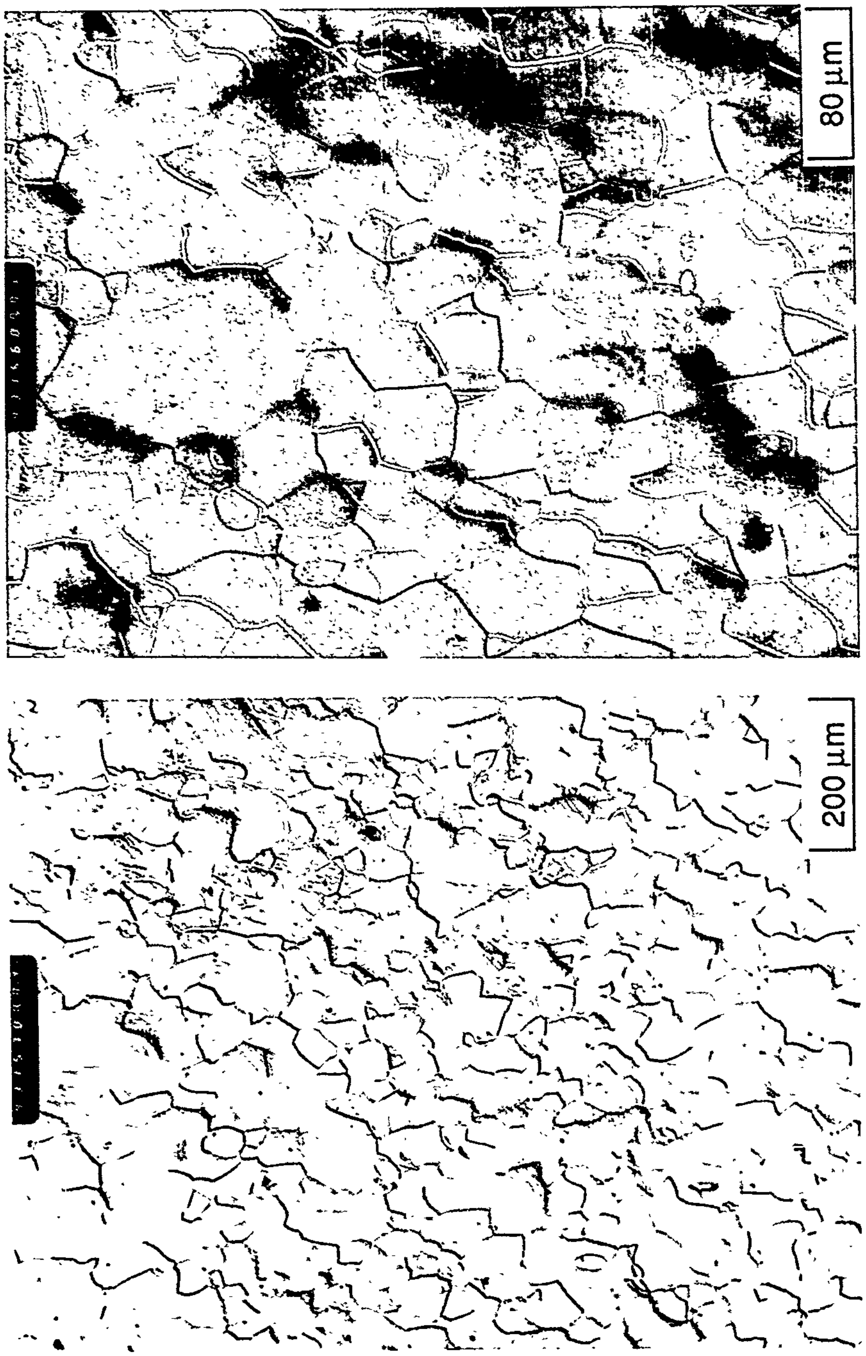

Figure 2. Reflected light photomicrographs of tantalum hardware showing the effects of corrosion by liquid plutonium. This part was an electrode support fixture used in plutonium electrorefining.

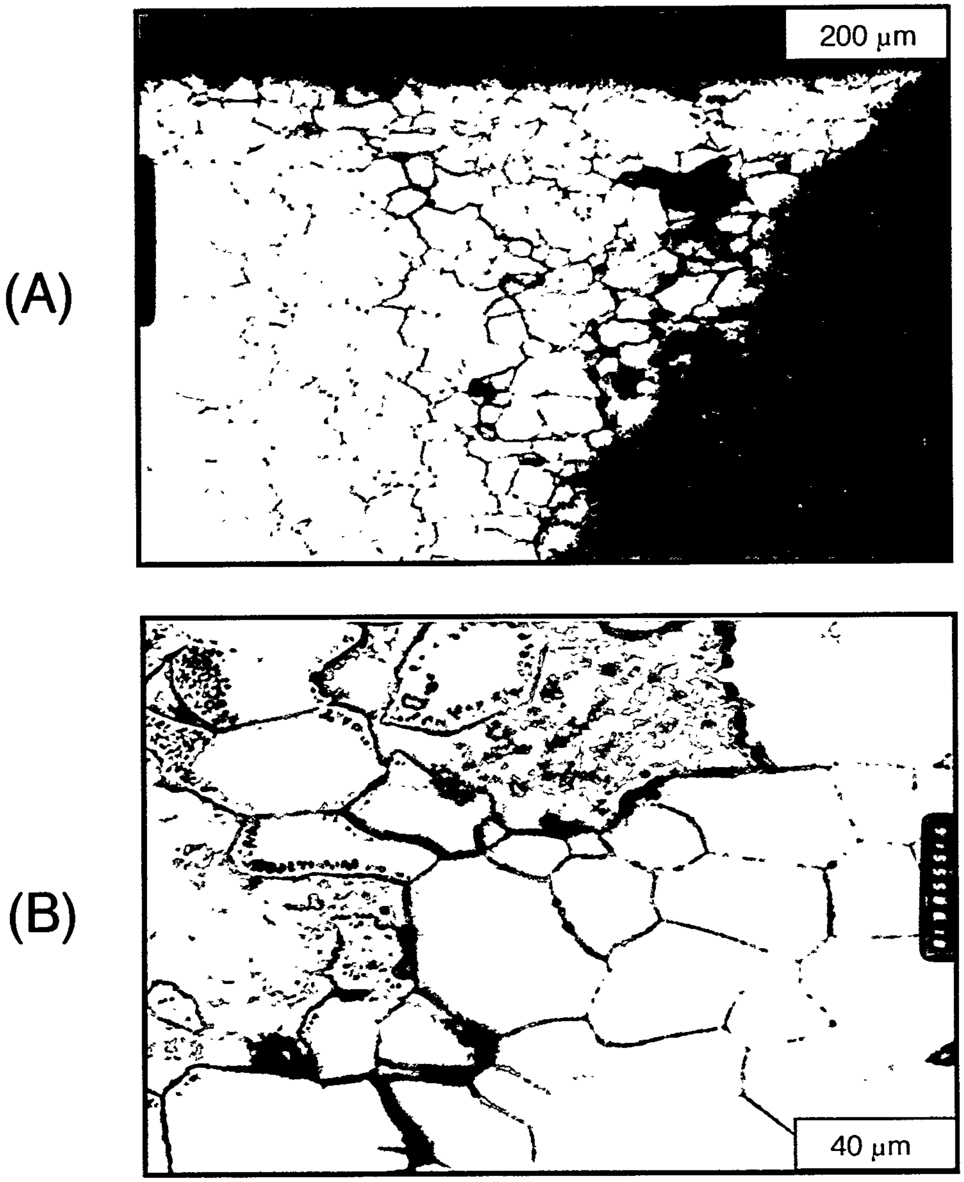

Molten halide salts were present in all exposure cases. Due to the relatively high thermodynamic stability of the tantalum chlorides, the salts were examined for possible reaction products which would indicate corrosion effects on tantalum. Chemical analysis of the salts revealed no appreciable amounts of tantalum reaction products. Mass spectrometric analysis of the off-gas detected no evidence of the volatile tantalum chlorides.

Also evidenced in Figure 2. is the bulk plutonium solidified in place on the hardware. The plutonium appears as a constant gray phase surrounding the tantalum-based phase which has faceted edges. Integral grains of tantalum are shown as suspensions within the plutonium. These are tantalum grains which were dislodged from the hardware due to severe grain boundary corrosion.

Multiple samples, in the order of 0.5gm each, were taken from the plutonium product phase and chemically analyzed. In the majority of individual samples, the values for tantalum detected in the plutonium were below the solubility limit. The solubility limit for tantalum in liquid plutonium is in the order of a tenth of an atomic percent at the operating temperature of the electrolytic purification, and the dissolution rate is kinetically limited over the time of the process. It is interesting to note that some specimens contained extremely large amounts of tantalum, far above the solubility limit.

The contribution of low-levels of tantalum to the homogenized plutonium samples was due to material removed from the grain boundaries of the bulk material where the solid is typically more disordered and energetic. The localized, anomalous tantalum values are considered to be associated with tantalum grains physically located in select aliquots of plutonium metal being analyzed and not present as the dissolved substance at elevated temperatures. By inspection of the micrographs it can be seen that the grain boundary material within the tantalum part was preferentially removed while the ordered, granular tantalum remained relatively preserved. Based on the amount of plutonium present in the system, if the tantalum part was uniformly dissolved until the solubility limit was reached, there would be only a negligible reduction in cross sectional thickness and the structural integrity would not be violated. However, in fact the part failed catastrophically in service. The chemical analyses support the interpretation of the metallography which suggests a grain boundary corrosion mechanism.

Metallic crucibles in general have historically proven to be unsuccessful due to wetting behavior with the liquid plutonium product phase. Established plutonium processing technology incorporates solidified metal transfer for product recovery, hence a viable containment vessel must provide for clean, discrete phase disengagement. This mechanical feature has been demonstrated in the selected carbon-tantalum alloy studied in this investigation as has been described in section 6.3.

A partial and temporary solution to the liquid metal wetting and corrosion problems involves an oxidizing pre-treatment of tantalum crucibles for select applications. This involves a deliberate partial oxidation of tantalum crucibles by heating in air. A thin oxide coating is produced, and oxygen is also taken into solid solution. These pretreated crucibles perform without wetting but several disadvantages are presented. The oxide film is not inert with respect to liquid plutonium. During service, plutonium oxide forms insitu forming a barrier layer which inhibits wetting of the crucible by liquid plutonium. The overall reaction to form this passivating layer is shown here.

$$2Ta_2O_{5(s)} + 5Pu^{o}{}_{(l)} \Rightarrow 5PuO_{2(s)} + 4Ta^{o}{}_{(s)}$$

Because of the removal of tantalum oxide via the insitu surface reaction, the crucibles require periodic oxidation treatments throughout their service life. Of course the crucibles are radioactively contaminated after their initial usage, and subsequent oxidation treatments must be conducted within a glove box enclosure. Unfortunately, each oxidation treatment creates a flocculant tantalum oxide dust within the glovebox which leads to blockage of the in-line air filtration system.

Another disadvantage is that the oxidation pre-treatment step embrittles the tantalum due to the introduction of dissolved oxygen. The loss of ductility leads to premature failure of the crucibles in service. The discarded crucibles account for another significant contribution to contaminated waste volumes.

The ceramic vessels used in pyrochemical operations are also eligible for a materials substitution. Large contaminated waste volumes are generated from the discard of ceramic containment vessels used in pyrochemical operations. These crucibles must be broken open to recover product, and therefore provide only a single-use service life. This mechanical method of product recovery presents an indirect but important human factor which can be addressed by materials substitution. As the ceramic vessels need to be broken open, the operator must separate crucible shards from product. When the operations are conducted within a radiological enclosure, this separation of materials adds time and subsequently increases radiation exposures to the operator. In addition, the crucible shards can puncture the glovebox gloves and cause a breach of containment.

By substituting a mechanically robust metallic candidate for the large single-use ceramic vessels, this crucible break-out and mechanical separation task can be eliminated from the processing scheme. This materials substitution could provide a greater than 50% reduction in radiation exposure times associated with product recovery.

The thermal profiles used in pyrometallurgical operations are dictated by the thermal shock resistance of the ceramic components, particularly the large containment vessels.

Since the ceramic bodies, typically MgO-based materials, provide only marginal thermal shock resistance, the heating and cooling rates are prescribed to accommodate this inherent limitation of the material. This leads to extended processing times for each batch run. By a materials substitution with a robust, stable metallic candidate, the processing scheme can be realized over dramatically reduced elapsed times.

## 3.0 IDENTIFICATION OF TANTALUM-CARBON ALLOYS AS ALTERNATIVE CONSTRUCTION MATERIALS

The development of alternative construction materials has been addressed in a number of projects linked to this research. The materials interactions involving traditional construction materials has been well documented in these previous studies [1,2 3,4,5] which have provided the foundation for this research. The observed materials interactions established the basis for viable substitute materials.

An evaluation of the corrosion mechanisms indicated the required microstructural properties for the candidate. The compositions of the processing systems established the criteria for thermodynamic stability, and the physical operations involved in service defined the required mechanical properties of a viable candidate construction material. Ideally, an engineered material could be identified which would possess the robust strength found in metallic candidates with the stability of a refractory ceramic. Traditional coated materials were unsuitable due to the combined exposures to liquid metals and reactive gasses. If the corrosion resistant properties were associated with a surface phase, such as in the case of coatings, a minimal cross sectional thickness reduction by transgranular gas-phase corrosion would ultimately remove the coating and subsequently expose the substrate. Based on the combination of operative corrosion mechanisms, specific microstructural features were identified for a viable candidate. The regions of the hardware most susceptible to liquid metal attack are the grain boundaries.

By producing a sufficiently refractory phase in occupancy of the grain boundaries, the corrosion effects of liquid metal could be obviated and, by virtue of the metal matrix composition, desired mechanical strength could be retained. In addition, by possession of a macroscopically uniform microstructural arrangement, the corrosion resistant properties would not be exclusively associated with the surface phase and would be retained after transgranular attack.

In comparison, coated materials loose their corrosion resistant properties after cross sectional thickness reductions equivalent to the width of the coating. Considering the high temperature exposures to oxygen and chlorine during pyrometallurgical service, some amount of cross sectional thickness reduction due to transgranular corrosion must always be expected.

A detailed treatment of the methodology used in the evaluation of alternative materials has been described in a previous work[6] by the author and is outlined within this section.

## 3.1 Strategy for selection of alternate materials

In general, the strategy for alternate materials selection can be described as a progressive approach. This starts with the development of an in-depth understanding of the materials application since the processing conditions and system compositions provide the criteria for the alternative material.

In general this is approached from a standpoint of thermodynamic stability and the mechanical strength of materials. However, in specific instances, other material attributes become important. For example, in certain glovebox operations, ergonomics dictates weight limitations for the larger hardware components. In those particular operations, containment vessels and hardware must be rapidly moved and are often handled at extended arms length. Therefore, a compromise in corrosion resistance may be accepted in order to realize a weight reduction by using a lower density construction material.

The electrical conductivity of candidate construction materials becomes an issue in electrolytic operations. For example, to implement a reusable containment vessel in plutonium electrorefining, a reconfiguration of the electrolytic cell was indicated. This was due to the introduction of an electrically conductive alternate construction material (C-sat.Ta) in substitution for an electrically insulating ceramic (MgO).

### 3.1.1 Substance thermodynamics and process system compositions

Preliminary selection of candidate materials is undertaken based upon their thermochemical properties with consideration of the service environment in which they must perform. This is accomplished by comparing the substance free energies of formation. In the initial stage of this investigation, a number of candidate materials were evaluated[7,8,9,10].

Following the aforementioned methodology, candidate materials were initially selected based upon their thermodynamic stabilities with respect to the pyrochemical systems of the service environments. The Gibbs free energies of formation for the substances in the candidate materials were compared to the formation energies of the possible interfering species. For example, in application for construction materials in plutonium oxide reduction processing, the formation energies for $Ta_2C$/TaC were compared to the potential carbide species PuC, $Pu_2C_3$, and $CaC_2$ on a gram-atom carbon basis. Those carbides were considered to possibly appear through materials interactions with the system hardware since the parent metal species, plutonium and calcium, were present in their elemental form within that processing system. In the plutonium pyrometallurgical operations described earlier, the formation of the interfering species PuC, $Pu_2C_3$, and $CaC_2$ were considered as potential reaction products with a carburized tantalum construction material. However, a review of the formation energies for these substances reveals that it would be unfeasible from a standpoint of chemical thermodynamics to expect their appearance via reduction of either of the tantalum carbides.

The relative stabilities of these substances are shown in Figure 3 which displays a Richardson diagram[11] construction for selected carbides.

Figure 3. Richardson diagram of formation energies for selected carbides. Note that for comparative purposes all values are presented on a gram-atom carbon basis. The diagram illustrates the relative stability of $Ta_2C$ compared to a number of recognized carbides.

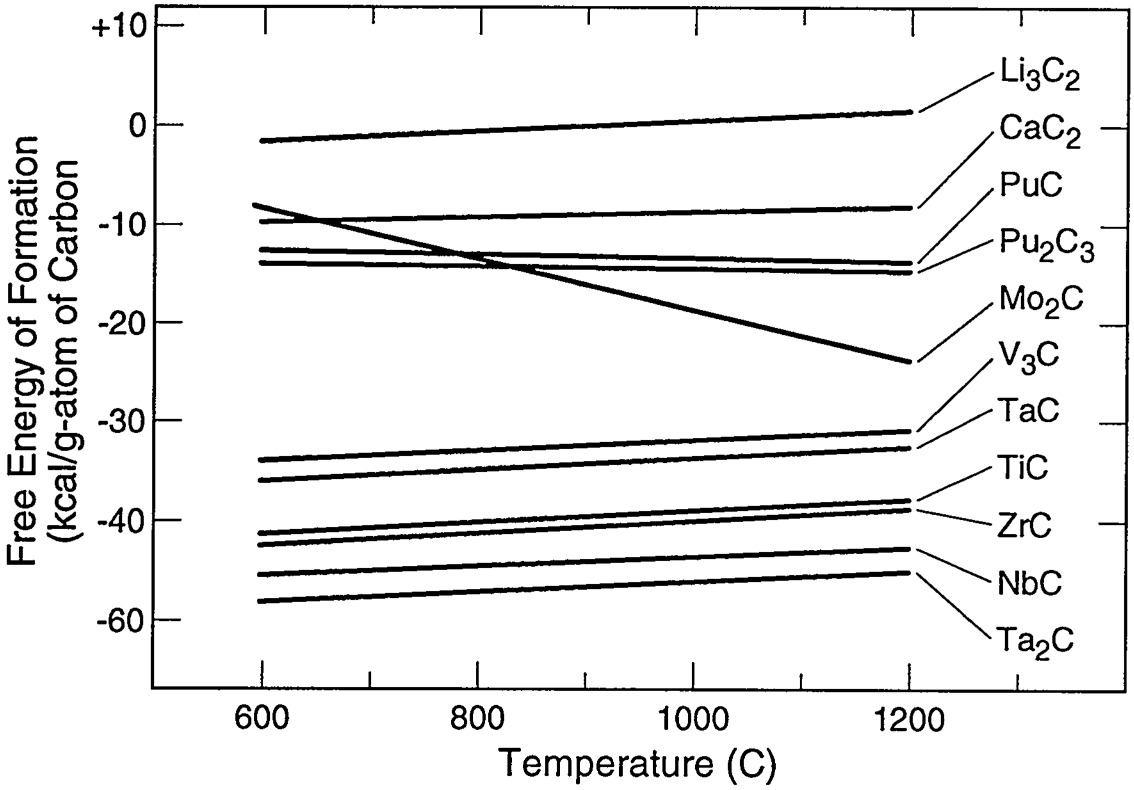

### 3.1.2 Computer Modeling

System thermodynamic modeling was used to predict materials interactions in complex, heterogeneous processing systems. This involved using free energy minimization of complete pyrochemical systems at elevated process temperatures. The results of the modeling were in the form of calculated equilibrium system compositions based upon the phase assemblages corresponding to the computer generated global free energy minimum.

Computer modeling was used as a guide to experimental materials testing. A campaign of computer modeling[12] has been completed to evaluate proposed candidate materials for viability as construction materials for pyrochemical crucibles. The candidate materials which appeared promising based on the results of the computer models were experimentally evaluated in actual pyrochemical service environments to confirm the modeled predictions and to evaluate specific mechanical/structural characteristics.

The modeling involved evaluating the effects on product speciation and phase assemblage when candidate materials are substituted into the system for the conventional construction materials. The usefulness of thermodynamic modeling in materials selection has been discussed in some of the authors previous work on the subject[13]. Virtually all of the reported work in this area has been conducted by the author and coworkers[14,15,16,17].

The technique used for modeling a metallurgical system from a standpoint of thermodynamics involves a computer-generated equilibrium composition based on the free energy minimum for a complex, heterogeneous chemical system.

The MTDATA computer codes were used in the system thermodynamic calculation. These codes are produced at the National Physical Laboratory, Teddington, UK and have been used before in published phase investigations of metallurgical interest[18]. The model calculates an equilibrium system composition and phase assemblage for complex, heterogeneous chemical systems. The modeling is based upon the principle that equilibrium compositions within multicomponent systems can be calculated from chemical thermodynamics. The benefit of this form of computer modeling is that one can predict effects on a chemical system from variations in processing conditions such as materials substitutions, reactant ratios, or operating temperature.

In the present case, the model was used to predict the final system composition for a batch-scale plutonium electrorefining run. The initial composition was entered into the model. This included metallic plutonium and an equimolar KCl-NaCl salt flux. The model was constrained to a fixed system pressure (760 torr), but the system volume was not constrained. The maximum system temperature was set at 850°C. The initial gas phase was pure argon as is the case in the actual processing scenario. In the model, a $Ta/Ta_2C$ alloy was introduced in materials substitution for MgO, the traditional containment material.

The results of computer modeling of the plutonium electrorefining system is presented in Table 1. The carbides of plutonium, considered to be interfering species, were not predicted in the equilibrium composition. The refractory carbide $Ta_2C$ was retained.

The model predicted a small amount of $PuCl_3$ forming via reaction with the molten salt. This is consistent with observed system behavior based on supporting information from chemical analyses. The model predicted the appearance of gaseous salts and sodium vapor which is also consistent with experimental evidence.

The same modeling was conducted with the MgO containment vessel, and the appearance of small amounts of metallic magnesium was predicted along with the highly stable PuOCl phase. This indicated crucible interactions. The appearance of the oxychloride species is the result of reactions between the plutonium, the salt, and the oxygen provided by the crucible interactions. The computer modeling was confirmed through experimental verification tests and chemical analyses which confirmed the final system composition and identification of interfering species.

### 3.1.3 Initial experimental testing

Experimental testing is conducted on a small scale to confirm the modeling predictions and characterize physical/mechanical attributes such as thermal shock resistance. In addition, full-scale tests were conducted without plutonium to determine wetting characteristics and reactivity with the molten salts.

Table 1. Predicted equilibrium composition for the plutonium electrorefining system based on computer modeling. The total system energy corresponding to the global free energy minimum was $-5.135\text{x}10^6$ calories. The equilibrium gas pressure was 760 torr, and the gas volume was $0.9\text{m}^3$.

| GAS PHASE COMPONENTS | | INDEPENDENT CONDENSED PHASES | |
|---|---|---|---|
| SUBSTANCE | MOLE NUMBER | SUBSTANCE | MOLE NUMBER |
| AR | 10.000 | $Ta_2C$ | 0.400 |
| KCl | 0.016 | KCl | 16.969 |
| $K_2Cl_2$ | 0.007 | NaCl | 16.981 |
| NaCl | 0.009 | $PuCl_3$ | 0.001 |
| $Na_2Cl_2$ | 0.004 | Pu | 2.899 |
| Na | 0.002 | Ta | 9.200 |
| K | 0.001 | | |

The approach of taking computer models in concert with experimental verifications proved to be an efficient strategy for preliminary evaluation of materials. Information in the initial tests helped predict the full-scale performance of candidate materials under investigation. A number of materials which appeared suitable from a thermodynamic standpoint were disqualified due to physical considerations.

### 3.1.4 Full-scale demonstration testing

Full-scale service testing of the carbon-tantalum alloys was conducted, and evaluation of performance was based upon postmortem examinations of the materials and product phases. The analytical services included optical metallography, electron probe microanalysis (EPMA) with Energy Dispersive Spectroscopy (EDS), X-ray diffraction (XRD), differential thermal analysis (DTA), and a suite of chemical analyses. Results of examinations are presented in section 6.

# 4.0 PREPARATION AND PERFORMANCE OF THE SELECTED TANTALUM-CARBON ALLOY

Through the results of computer modeling and experimental investigations, specific alloys within the tantalum-carbon binary alloy system were identified for potential applications. The alloy determined to be the most appropriate as a construction material for select pyrometallurgical operations is comprised of a 2-phase microstructure: the solid solution of carbon in the metal with a distribution of $Ta_2C$ inclusions. This engineered material is referred to as "C-sat.Ta".

## 4.1 Physical description of the tantalum-carbon alloy

The salient feature of the C-sat.Ta microstructure is extensive decoration of the grain boundary regions by $Ta_2C$ inclusions (see Figure 4). These carbides form by precipitation from supersaturated solid solutions of carbon in the tantalum-based substrate. In certain cases, carbon was partially retained in the solid solution phase. This was achieved by rapidly quenching the specimens from the carburization temperatures. (Based on the construction of the solvus line in the binary system tantalum-carbon, virtually all of the carbon would be driven from the solution phase if the material were cooled in a sufficiently slow manner).

The two micrographs appearing in Figure 4. display different metallographic preparations of the material. Micrograph 'A' shows C-sat.Ta in the ion etched condition.

Figure 4. Metallographic examination and microstructural features of C-sat.Ta alloy.

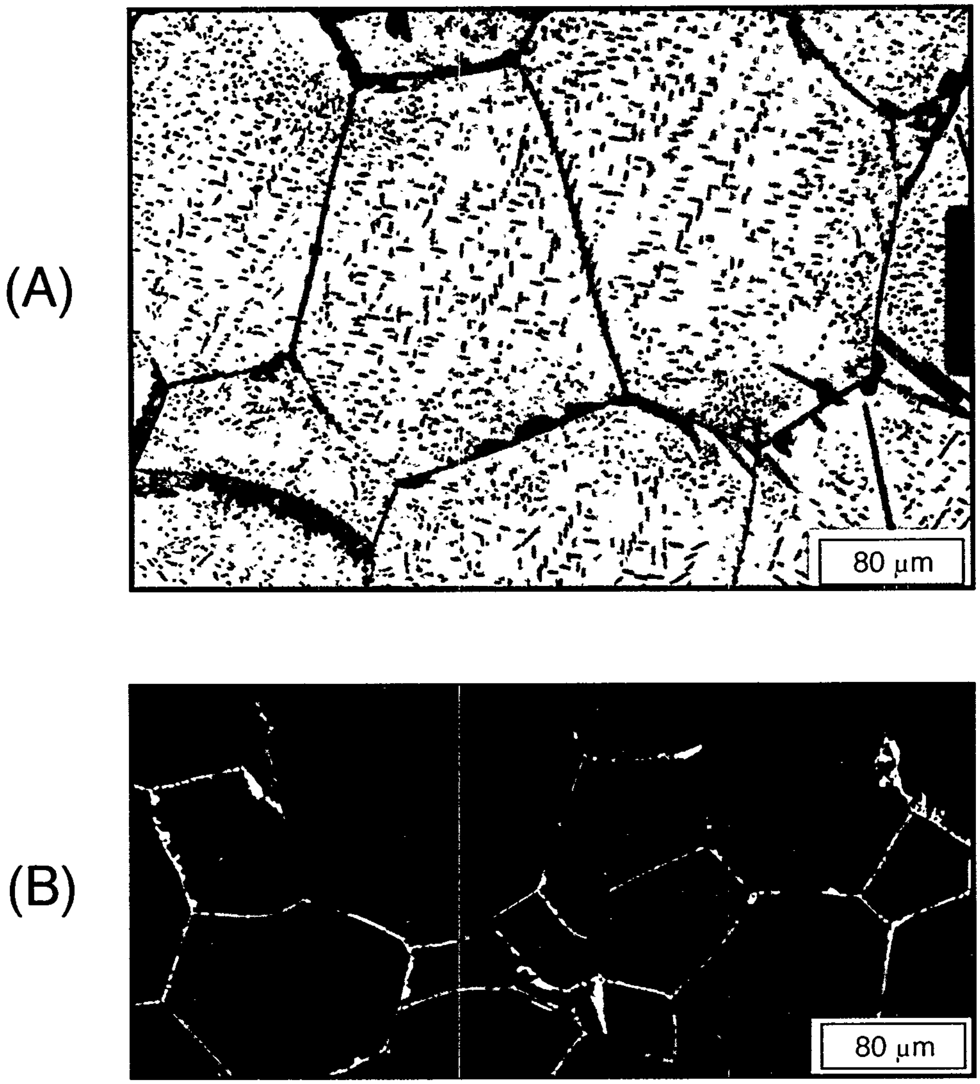

This procedure, traditionally used to resolve ceramic inclusions within metallic matrices, could not optically distinguish between carbides and certain mechanical artifacts. Microprobe examinations have revealed that the colonies along the grain boundaries in this image are $Ta_2C$, and that majority of the intragranular "inclusions" are not carbide but mechanical artifacts.

Micrograph 'B' shows the optimum metallographic preparation as developed at Los Alamos by Ramiro Pereyra. The image appearing here is reflected light photomicrograph of C-sat.Ta under bright-field illumination after an electrolytic etch at 35V DC. The etchant was 30% KOH in water. The carbides are highly resolved as the light phase within the darker metallic matrix. It is important to note that quantitative image analysis of these alloys was only possible after this preparation technique was developed. Image analysis resolves the carbide area fraction based on optical contrast in the image. This technique is only valid when the carbides are exclusively distinguished from the matrix phase.

Electron probe microanalysis was used to analyze specimens with regard to the composition of surface coatings and inclusions (precipitates). The instrument was the CAMECA Model MBX. The quantitative elemental studies were done with the microprobes' Energy Dispersive Spectroscopy (EDS) capability.

In this work, the EDS was supported by TASK-8 software[19]. This software was selected for its utility in quantitatively analyzing specimens containing elements with large differences in atomic number.

Microprobe examinations were conducted on numerous specimens to determine the composition of individual phases present. The examinations confirmed the composition of carbide precipitates as stoichiometric $Ta_2C$. The quantitative analysis was aided by the presence of the $Ta_2C$ coating (below the TaC surface layer) which provided a reference material in each specimen. Figure 5 shows images of the carbide coatings taken during microprobe examination. An X-ray point count was taken across the coating layers to determine their elemental compositions. The path of the scan is shown in Figure 5. Figure 6 shows the results of the X-ray scan revealing the tantalum and carbon content as a function of position within the coatings.

Two distinct carbide coatings were present after carburization of the metal. This was the case in all specimens prepared by either packed-bed methods or gas-phase carburization. The phase at the specimen surface was always identified as TaC, the most carbon rich intermediate composition in the binary system carbon-tantalum. This was anticipated as the surface of the material was always in contact with a reactant of high carbon activity, the graphite bed or the carbonaceous gas. A discrete layer of $Ta_2C$ was always observed between the TaC layer and the substrate. This is also consistent with the binary phase diagram construction as $Ta_2C$ is the most metal-rich intermediate and, in an equilibrium condition, must be retained adjacent to the metal.

Figure 5. Electron microprobe examination of carbide coated tantalum prepared in this investigation.

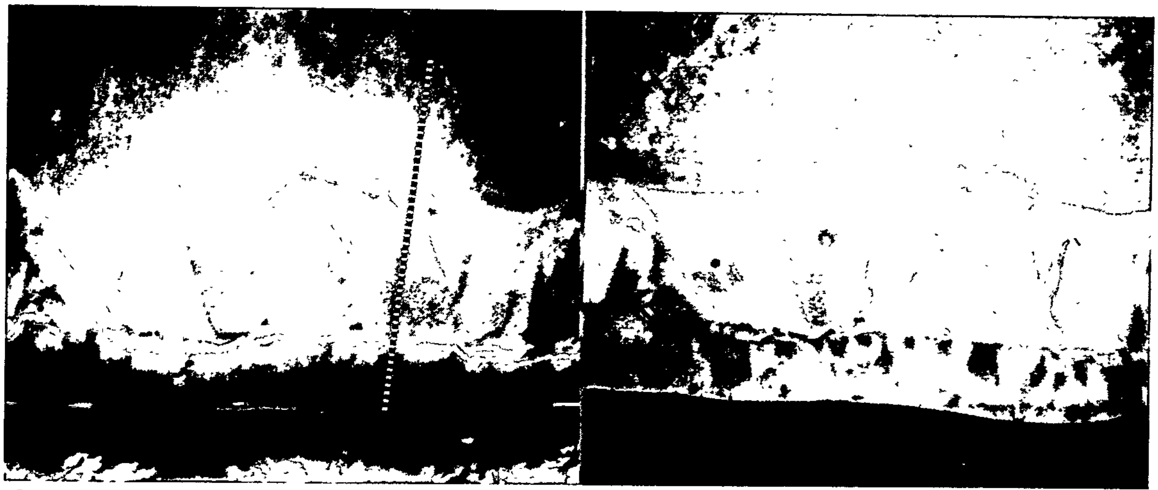

Secondary electron image showing the path of the quantitative scan . 1000X. |←→| =10 microns.

Backscattered electron image of the area at left. 1000X. |←→| =10 microns.

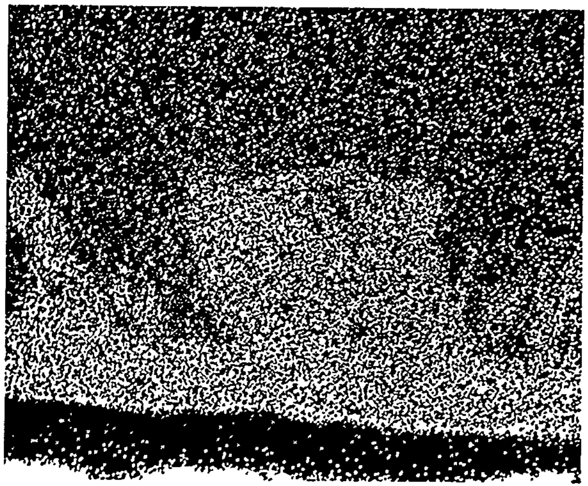

C X-ray image.

Figure 6. X-ray scan results from EDS analysis with electron microprobe. Note the carbides were identified as TaC and $Ta_2C$ based on their elemental compositions.

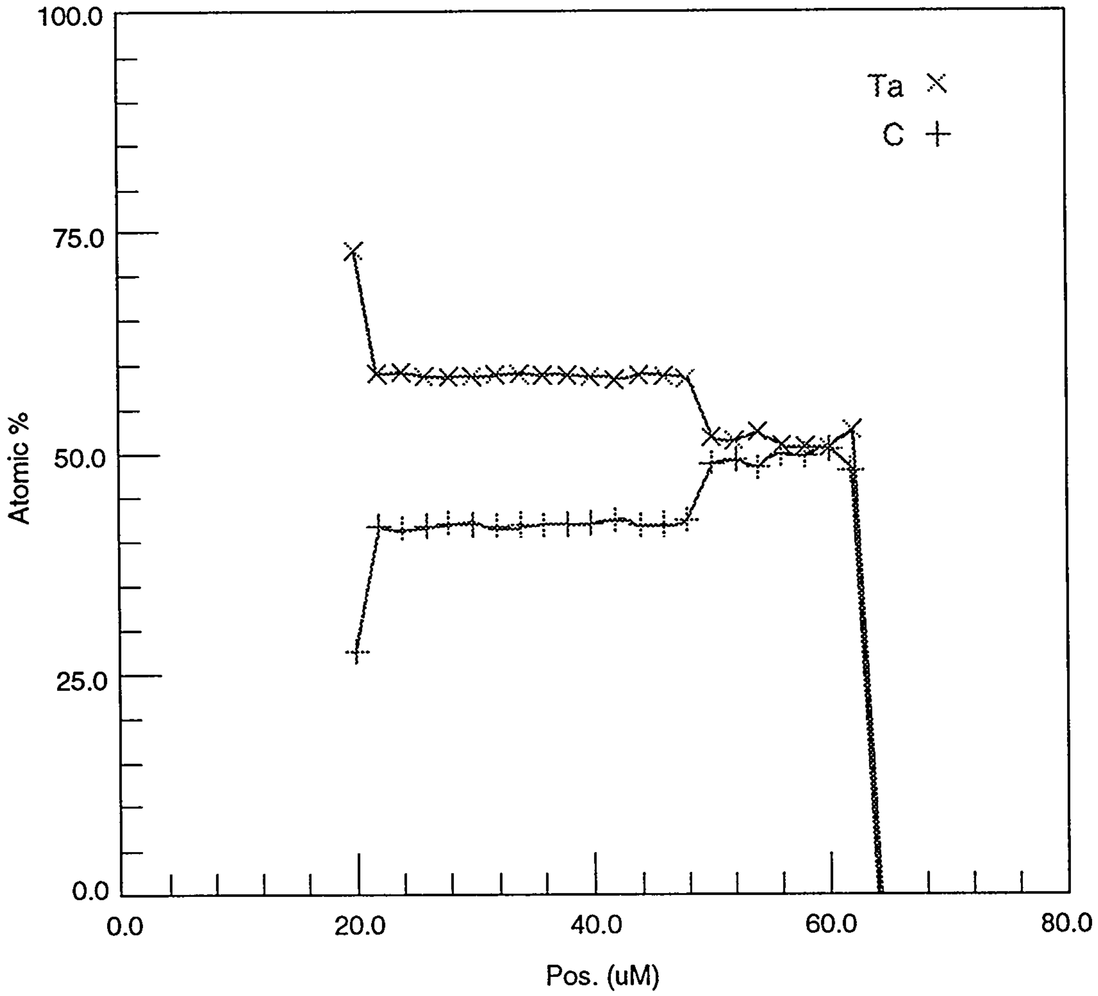

### 4.2 Performance of C-sat.Ta alloy

Both the precipitate colonies and the solid solution phase contribute enhanced corrosion resistance to the material. The carbides, which occupy the grain boundary regions, inhibit attack by liquid metal at elevated temperatures. It is this intergranular attack that represents the leading corrosion-induced mechanism leading to failure of hardware in plutonium pyrometallurgical processing. The solid solution phase, which contains carbon within the tantalum structure, exhibits greater resistance to transgranular corrosion mechanisms such as by reactive gasses. In a study[20] at Battelle, the transgranular corrosion rates were measured in exposures of bare tantalum and tantalum with dissolved carbon through exposures to oxygen at high temperatures.

In the tests conducted at 1200°C, the specimens with dissolved carbon exhibited a 15% reduction in corrosion rate. As described later, enhanced corrosion resistance to chlorine at elevated temperatures was demonstrated with additional performance data obtained in the present work.

Figure 7 shows reflected light images of a section removed from C-sat. Ta hardware which was used in plutonium pyrochemical operations. The dramatic enhancement of corrosion resistant properties is illustrated by comparison to the bare tantalum specimen after similar processing exposures (previously shown in Figure 1). The photomicrographs in Figure 7 show C-sat.Ta after multiple exposures to liquid plutonium in full-scale processing operations. Ion etching was employed to resolve the carbide phase within the metallic substrate. This caused the topography within the plutonium phase (upper region).

Figure 7. Microstructural examination of C-sat.Ta after extended service in plutonium pyrometallurgical operations.

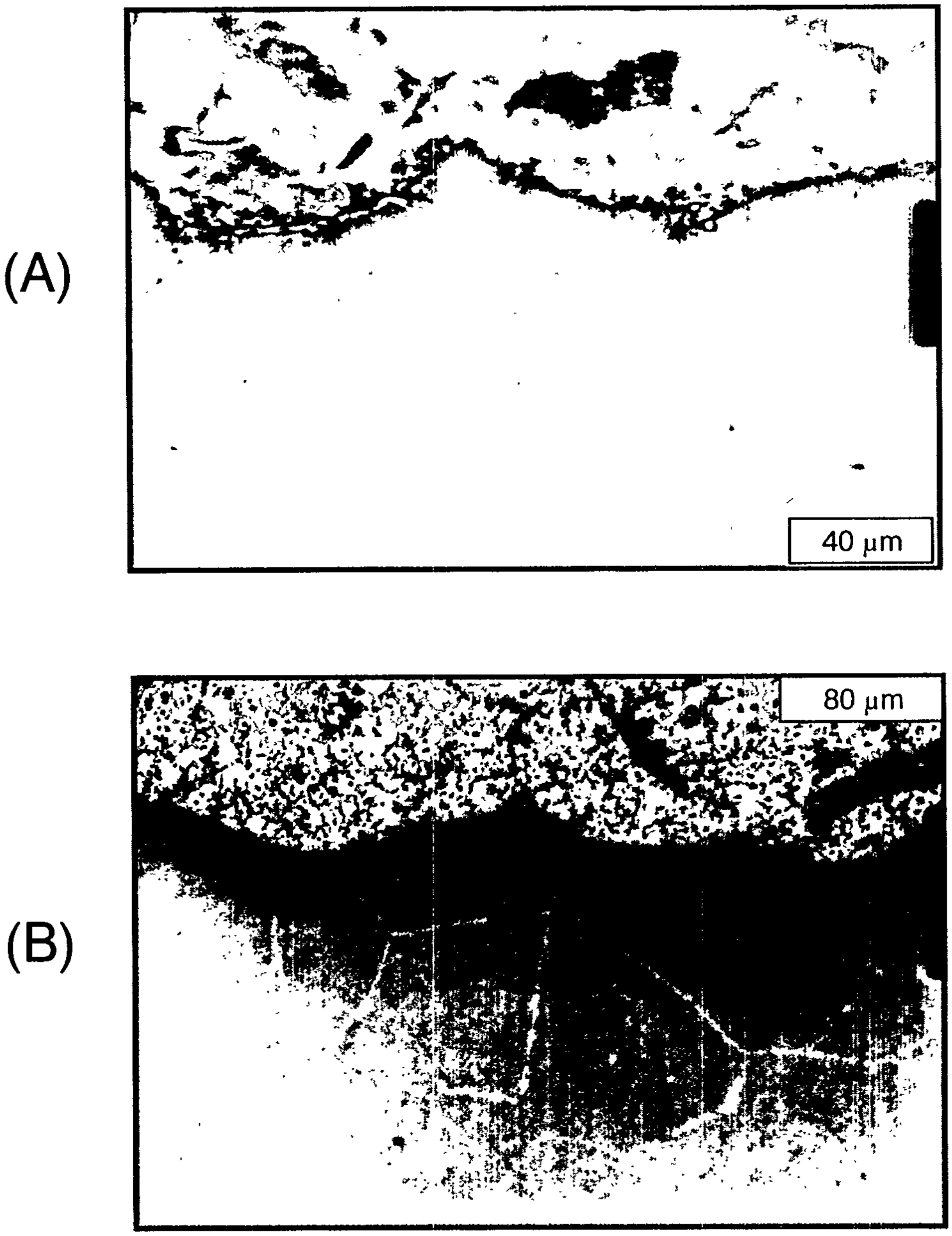

The grain boundaries are occupied by $Ta_2C$ precipitates (light phase) within the tantalum-based matrix. The carbides, which colonize along the grain boundaries, inhibited the corrosion by liquid plutonium.

## 4.3 Preparation of the C-sat.Ta alloy

The preparation of C-sat.Ta has been conducted via a multi-stage process:

1) Surface carburization of the metal to produce a carbide coating. This involves reactions with activated carbon bed media or with carbonaceous gasses such as methane.

2) High-temperature annealing to dissolve carbon from the carbide surface into the substrate - a saturation process to load the matrix with interstitial carbon.

3) Cooling to room temperature during which time the solution becomes supersaturated invoking the precipitation of carbide from within the bulk material.

4) Subsequent aging to redistribute the carbide population and produce specific size distributions of the carbide inclusions.

The investigations described herein include both performance testing of the selected alloy and a quantitative treatment of its microstructural development.

The alloy development work focuses on quantification of growth kinetics of $Ta_2C$ precipitates from supersaturated solid solutions of carbon in tantalum. The kinetic investigation provides information on the optimum preparation techniques for this material.

# 5.0 REVIEW OF PREVIOUS INVESTIGATIONS

Previous investigations have included studies of tantalum-carbon phase behavior, development of carbide coatings on tantalum-based substrates, kinetic studies of carbide formation, and testing/evaluation of the material in service environments. An extensive review of the open literature was completed in prelude to conducting the current investigation. The compendium of assembled information was not limited to a conventional literature search. Due to the sensitive and sometimes classified nature of select applications for tantalum-based materials, much information is withheld from public dissemination. In addition, a number of previous investigations remain unpublished. In consideration of these facts, a search of internal documents within the US national laboratories was completed, and the relevant controlled information within the LANL archives and the DOE classified data bases was reviewed. Additionally, the authors of relevant published investigations were contacted for purposes of discussing the current work.

## 5.1 Phase behavior in the system tantalum-carbon

A construction of the tantalum-carbon binary alloy phase diagram which reflects contributions from multiple, independent investigations appears in Figure 8. The most relevant published works are briefly described herein.

Figure 8. The tantalum-carbon binary phase diagram.

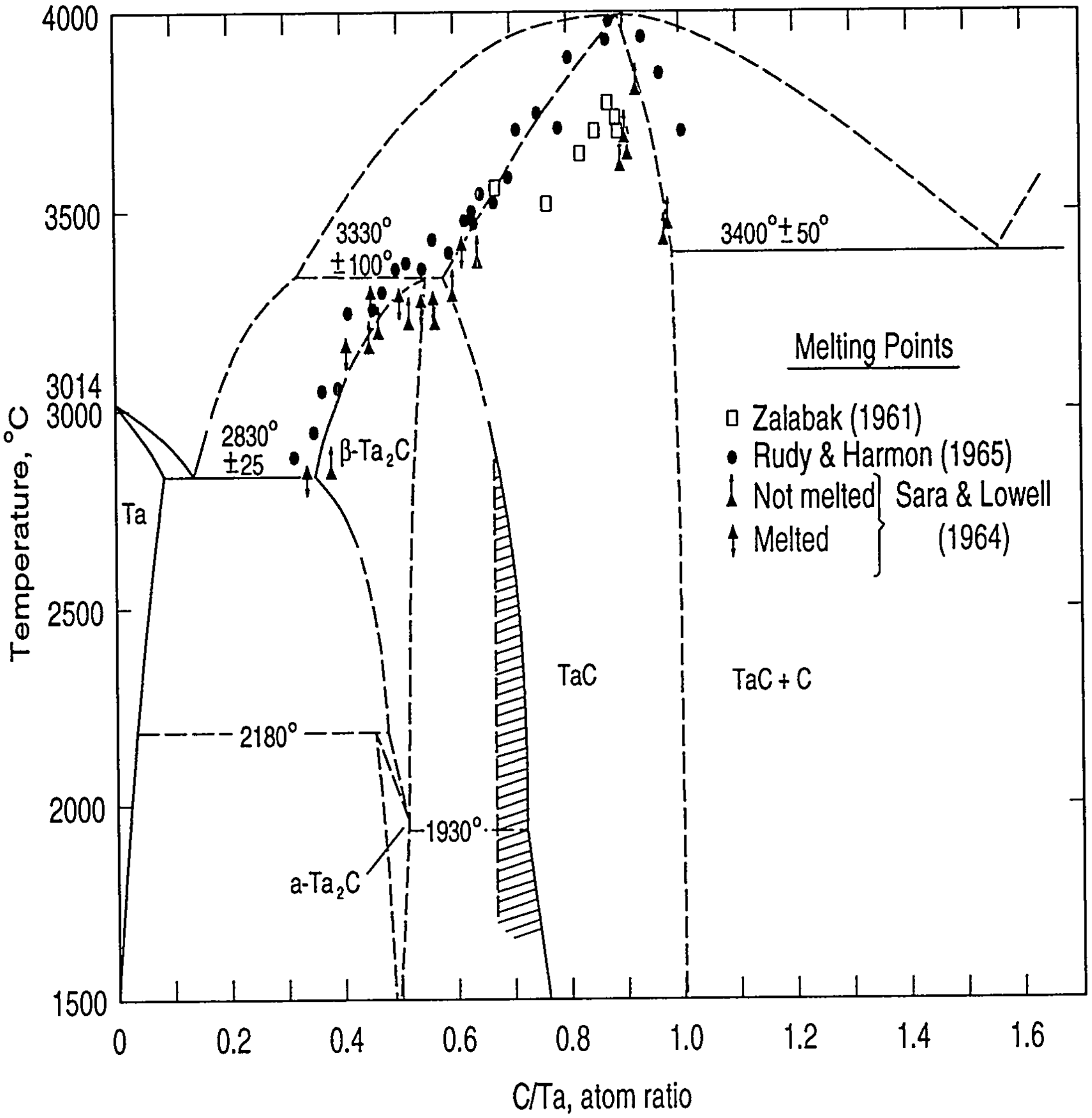

Early published works on the tantalum-carbon system were focused on the 1:1 intermediate phase, tantalum monocarbide. There are a plethora of investigations focused on the structural characterization of the monocarbide. The TaC compound is cubic, NaCl prototype, with a=4.45Å. The crystal structure was originally reported by Van Arkel[21] in 1924 and confirmed by other investigators[22,23,24,25,26,27,28,29].

The structure of $Ta_2C$ was first reported by Burgers and Basart[30] as the only crystallographic modification. The structure is hexagonal with a=3.097Å and c=4.94Å. Later, Ellinger[31] confirmed that structure for $Ta_2C$ and also did not mention polymorphism. In another study, the presence of a crystallographic modification was reported by Hauser[32] who explained that phase change is an order/disorder transition on the carbon sublattice. That work confirmed the original report of a hexagonal structure (for both forms of the intermediate phase). Later, Bowman and coworkers[33] studied the order-disorder transition in great detail.

A number of investigators have reported values for the melting point of the monocarbide with a considerable degree of inconsistency between those values. The discrepancies are attributed to two principal factors; the difficulty in performing accurate melting point determinations at such high temperatures and the difficulty of obtaining well-characterized single-phase specimens, the latter consideration being specially significant for the earliest datum which dates back to 1925.

To illustrate the inconsistency between investigations, the reported values for the melting point of the monocarbide are displayed in Table 2.

Table 2. Melting point determinations reported for TaC.

| MELTING POINT (T, $^{o}$C) | YEAR | REFERENCE |
|---|---|---|
| 3825 | 1925 | Freiderich and Sittig[34] |
| 3875 | 1930 | Agte and Alterthum[35] |
| 3540 | 1957 | Geach and Jones[36] |
| 3780 | 1958 | Brownlee[37] |
| 3550 | 1960 | Nadler and Kempter[38] |
| 3740 | 1961 | Zalabak[39] |
| "4000-4200" | 1964 | Bowman[40] |
| 3983 | 1965 | Rudy and Harmon[41] |

The first extensive work published on tantalum-carbon phase behavior was produced by Ellinger[42] in 1943. That work included a tentative construction of the diagram with estimated placement for the majority of phase boundaries. (A reproduction of that early diagram still appears in the compilations by Shunk[43] and Hansen[44])

Another construction of the diagram was published by Kieffer and Benesovsky[45] which expanded upon the Ellinger work and included further experimental data.

The most current construction of the tantalum-carbon binary phase diagram is the one produced by Rudy and Harmon[30]. The original work appeared in their published report from the Air Force Materials Laboratory. The diagram by Rudy and Harmon includes data on the alloy system produced by an adjunctive approach incorporating x-ray diffraction, chemical analysis, and differential thermal analysis (DTA). The authors noted that the phase behavior of the tantalum-carbon system was analogous to the niobium-carbon system for which the published binary phase diagram already existed[46]. They implied that the known phase behavior of the niobium-carbon system provided a template for their investigations with tantalum.

It is noted that in alloy development efforts conducted prior to the current work, the carburization behavior of niobium was investigated by the author. In that experimental campaign[47], analogous carburization behavior was observed in the niobium-based system over a lower temperature regime.

The binary diagram produced by Rudy and Harmon also appears later in a published compilation[48] by the same authors. Incidentally, Moffat[49] chose to reproduce that diagram but makes reference only to the latter compilation and not the original work.

The binary alloy phase diagram construction by Rudy and Harmon was selected for the principal reference in this work based upon the fact that it reflects the most recent experimental data and that the supplemental experimental details provided by the authors are in exceptional detail.

A description of salient features within the system tantalum-carbon is provided based predominantly on the work by Rudy and Harmon. Discrepancies between their work and the other published investigations on this system have been identified and are discussed here.

The phase diagram shows the $\alpha$-$Ta_2C$ phase decomposes by a peritectoid reaction to the tantalum solid solution phase and $\beta$-$Ta_2C$ at 2180°C. The $\beta$-$Ta_2C$ phase first appears at 1930°C by a eutectoid reaction involving $\alpha$-$Ta_2C$ and TaC. The limits of the $Ta_2C$ homogeneity range, as measured by Rudy and Harmon, are recorded in the compilation by Storms[50] published in 1967.

A large range of homogeneity is shown for the TaC phase extending from 49.8-36.5 mole % carbon. The composition converges at 47 mole % carbon where it melts congruently at 3983°C. Incidentally, TaC is one of the highest-melting known substances.

To characterize the solvus line, Rudy and Harmon used a technique which involved quenching specimens from the elevated temperatures to preserve the phase distribution. They stated that precipitation of the $Ta_2C$ phase, the most tantalum-rich intermediate, occurred at cooling rates of approximately 1000°C/sec from temperatures approaching that of the eutectic.

In utilizing that quenching technique at the highest temperatures, 3 mole % carbon was the maximum retained as the dissolved species within the matrix. Rudy and Harmon obtained solubility data by a technique described in detail by Axler and coworkers[51]. This technique involves measuring the area fraction of inclusions (in this case $Ta_2C$) within micrographs taken of specimens in the quenched condition. Since the micrographs can be taken as typical cross-sectional representations, the area fraction data acquired from those images correspond to volume fraction data.

When taken in concert with the known stoichiometry of the precipitates and matrix phase, the volume fraction data can be used to calculate the overall composition of the single solution present at the elevated temperature.

The terminal solubility of carbon in tantalum is of particular relevance to this work; therefore, all published works on solubility measurements have been reviewed. The techniques generally involved extended time exposures to a gas at selected temperatures followed by carbon assay of the reacted material.

A partial binary alloy phase diagram for Ta-C has been provided in Figure 9 which focuses on the region of interest to this work. This partial diagram presents a construction of the solvus line using the data of several independent researchers.

Figure 9. Region of interest within the tantalum-carbon binary diagram. The solvus line was constructed using the data of independent investigators.

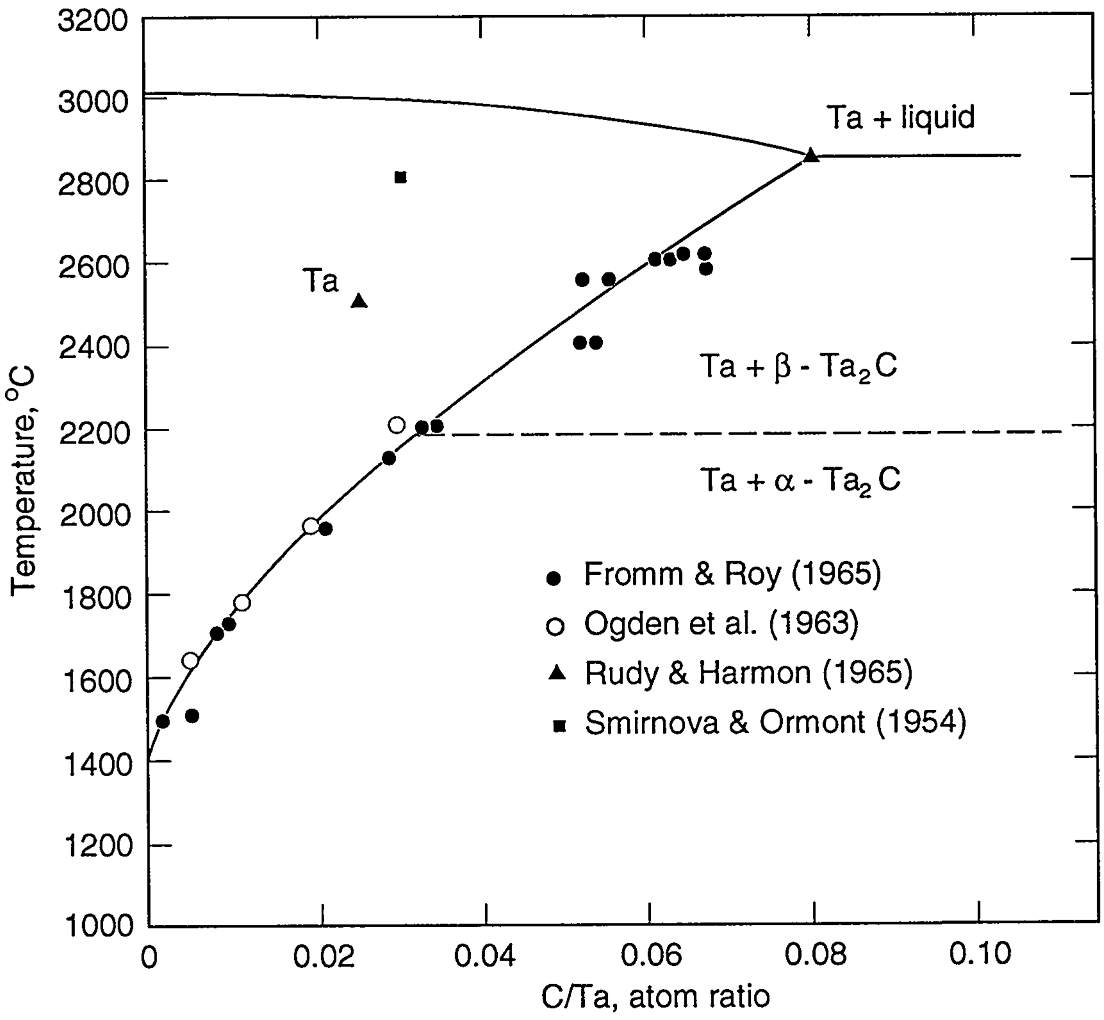

Although not represented in Figure 9, Horz et al.[52] conducted the most recent work on the solid solubility of carbon in tantalum. The solubility was measured indirectly by surveying the electrical resistivity changes in the metal during exposures to acetylene. In that work, solvus line data were not provided directly. Alternatively, expressions were provided for the solubility limit as a function of temperature over two ranges:

$$C_{\text{solid soln}} = 6630 \cdot \text{EXP}(-18200/T) \quad \text{at\%} \quad : 1500<T<1850^{\circ}\text{C}$$

$$C_{\text{solid soln}} = 464 \cdot \text{EXP}(-12700/T) \quad \text{at\%} \quad : 1850<T<2300^{\circ}\text{C}$$

It is noted that the expressions do not converge at the common temperature. The discontinuity in solubility behavior is dubious. Horz associated the discontinuity with the polymorphic transformation of $Ta_2C$. No other investigators report the transition at 1850°C. Furthermore, no other work indicated a pronounced change of solid solubility associated with the crystallographic modification of that intermediate phase.

According to the lower temperature expression provided by Horz et al., the solubility at 1800°C would be 0.269 at% (0.0027 C:Ta). This value is considerably higher than the value of 0.11% which appears in the solvus construction in Figure 9.

The 0.11% value for carbon solubility at 1800°C, obtained by Ogden, shows excellent agreement with the interpolated solvus construction including the work by Fromm and Roy.

However, the temperature measurements by Fromm and Roy may be criticized. In that work, 5mm diameter rods were reacted with graphite via radio frequency induction heating. The temperatures were recorded via single-color pyrometry, and brightness (surface) temperatures were taken as the true temperatures. According to the details provided in the published work, emmissivity corrections were not made.

In the early works[53,54,55] the independent investigators seem to be in agreement with a value of approximately 0.3 at % carbon in tantalum at the eutectic temperature. Later works, including those by Rudy and Harmon (discussed above), Smirnova[56], Storms[57], and Fromm and Roy[58] seem to agree on a considerably higher value of approximately 3 at %.

Fromm and Roy presented a well detailed account of their experimental investigation. They measured the solubility of carbon in tantalum by examining the composition of carburized rods of arc-melted tantalum prepared from powder and swaged to uniform diameter.

In that work, carburization of the metal was conducted at temperatures up to 2940°C. The carburization processing at temperatures above 2100°C was accomplished by inductively heating tantalum rods in close contact with graphite sleeves. This method provides uniform temperature of the specimen rods by virtue of the susceptibility of graphite to radio frequency (RF) fields.

To elucidate the dissolved carbon content, Fromm and Roy removed the coating by mechanical means, and chemical analysis for carbon was performed on the remaining material.

The analysis involved the complete digestion of the material in an acid solution, then examinations via spectroscopic methods. By employing this method, the tantalum/carbon ratio reflected contributions from both the precipitated carbide inclusions as well as the amount retained in the solid solution. Although the inclusions represent carbon expelled from solution during cooling, the total carbon in the dissolved specimens was considered dissolved at the quenching temperature.

The phase behavior on the carbon rich side is less complex. Another eutectic reaction occurs on the carbon-rich side of the diagram where the single liquid of 61 mole % carbon transforms to carbon and TaC upon cooling. The details of the system with compositions approaching the carbon axis were essentially omitted from the investigation by Rudy and Harmon.

All the published phase diagram constructions show the monocarbide to be in equilibrium with essentially pure carbon. Apparently, the solid solubility of tantalum in carbon can be neglected. The lack of rigorous characterization of the carbon-rich region of the diagram can be easily understood considering that predominant interest in the system has been historically focused on the highly refractory intermediate phases.

The paper by Rudy and Harmon presented a detailed discussion of metallographic interpretations. Metallographic examinations of their quenched samples revealed a two-phase microstructure with randomly distributed precipitate colonies within the matrix grains.

There was an observed tendency for $Ta_2C$ precipitates to agglomerate at the grain boundaries and depleted diffusion zones were observed adjacent to the grain boundaries. Rudy and Harmon also noted that in specimens quenched more slowly (approximately 10°C/sec), the intragranular precipitates appeared in "oriented patterns". The orientation of intragranular precipitates receives thorough treatment in the current work.

It is important to note here that Rudy and Harmon may include erroneous metallographic interpretations. In their work, micrographs are shown which include features within the grains considered to be intragranular precipitates. The features may have been associated with mechanical artifacts. Specimens produced in the current study with identical microstructural images were examined by electron microprobe. The analysis revealed that these artifacts were not carbide precipitates and were compositionally indistinguishable from the adjacent tantalum matrix.

Ramiro Pereyra has developed a highly refined metallographic preparation[59] which obviates the appearance of mechanical artifacts. Details of that preparation are presented within this document.

At temperatures approaching the solidus, the temperature dependence for carbon solubility in tantalum increases. A solubility of 2.5 mole % is reported to correspond with specimens quenched from 2500°C, while increasing to the terminal value of 7.5 mole % at 2843°C.

That maximum value corresponds to the temperature of the eutectic between tantalum and the most tantalum-rich intermediate phase, $Ta_2C$. The composition of that eutectic is shown to be 12 mole % carbon.

## 5.2 Production of the tantalum carbide coatings

The application of coatings to tantalum and tantalum-tungsten alloys was investigated by Krikorian and coworkers in 1967[60]. That work included a study of diffusion kinetics for carbon through the carbide phases. A further study of carbide formation kinetics was conducted as part of the investigations by Wallace and coworkers[61] A compilation on the diffusion within metal carbide phases was published by DePoorter and Wallace[62]. That work included a mathematical treatment of the principles of diffusion in the solid state.

A comprehensive work on the diffusion of carbon in the tantalum carbides was published by Resnick et al.[63]. In that work, the growth rate of both TaC and $Ta_2C$ were measured between 1800 and 2700°C.

Diffusion kinetics for carbon within the intermediate phases were estimated from the layer growth rates. The authors state the assumption that the layer growth is a function of the diffusion of carbon exclusively (no contribution due to the diffusion of tantalum). This is reasonable for formation of surface phases involving a gas phase reactant.

The other assumption stated by Resnick and coworkers was that the composition does not vary within each of the intermediate phases. The author remains dubious of that assumption since TaC has a fairly wide range of homogeneity.

The diffusion of carbon in tantalum was experimentally studied by Powers and Doyle[64]. In that work, the interstitial carbon compositions were measured indirectly using a mechanical relaxation technique originally developed[65] to measure interstitial solute concentrations in $\alpha$-iron. Published diffusion data for the system has been compiled in Table 3.

Table 3. Diffusion data for carbon within the phase of the tantalum-carbon binary alloy system.

| PHASE | $D_o$ ($cm^2$/sec) | $E_{ac}$ cal/mole·°K | REFERENCE |
|---|---|---|---|
| $Ta_{(solid\ soln)}$ | 0.0061 | 38510 | Powers & Doyle[64] |
| $Ta_{(solid\ soln)}$ | 0.0012 | 40300 | Son et al.[66] |
| $Ta_{(solid\ soln)}$ | 0.0067 | 38600 | Horz[67] |
| $Ta_2C$ | 7.0 | 89000 | DePoorter[62] |
| TaC* | 0.18 | 85000 | Resnick[68] |

* Values for stoichiometric TaC. A compositional dependence exists for carbon diffusion over the homogeneity range.

Extensive studies were conducted by previous researchers on the kinetics of precipitate *nucleation* in the analogous systems V-C[69,70] and Nb-C[71]. Powers and Doyle[72] studied the precipitation of carbide in the Ta-C system during a work on the internal friction measurements on solid solutions. They conducted internal friction measurements on solid solutions of both nitrogen and carbon in tantalum. The behavior of the tantalum-nitrogen system was consistent with expectations of linear dependence of the Snoek peak[73] with concentration of the solute species. However, anomalous results with carbon in tantalum were attributed to precipitation during aging.

In that work, specimens of 0.005 wt% carbon were quenched from 1800°C and subsequently aged at temperatures in the range of 400°C. The nucleation of carbide from the solid solution phase was observed during those agings. In that work, the investigators were able to retain solid solutions of less than 0.005 wt% carbon in tantalum during aging in the same temperature regime. They reported no quantitative information on the observed precipitation phenomenon. Dahmen has published work on the crystallographic nature of carbide nucleation[74]. The studies focused on the mechanism of growth and did not include rate measurements.

### 5.3 Application of the tantalum carbides

The first use of carburized tantalum in plutonium processing was conducted by Leary and Mullins[75] in an effort to produce ultra-pure plutonium metal. They used TaC-coated tantalum in plutonium electrorefining as the cathodic electrode surface in a materials substitution for bare tungsten.

That hardware was produced by forming the electrode to the net shape, followed by gas phase carburization. Both TaC and $Ta_2C$ surface coatings were used. In the cases with TaC surface coatings, $Ta_2C$ was present as an intermediate phase below the surface and adjacent to the metal substrate. During the electrorefining process, liquid metal drains from the cathodic surface; hence the coated hardware was not contacted with plutonium product metal during its solidification. Therefore, adhesion problems were a non-issue. The plutonium metal refined in the work with the tantalum carbide (TaC) cathode remains as the highest purity metal ever documented.

Other undesirable mechanical factors arise in the use of carbide-coated cathodes. Spallation of the coating was observed after multiple thermal cycles. Once the cathode was used it was radioactively contaminated and could not be removed from the service location for further carburization. The spallation problems made the material unsuitable for extended service.

Physical adhesion was an intractable problem when product metal was allowed to solidify in place on carbide-coated tantalum crucibles (crucibles possessing a continuous carbide surface).

In early stages of this research[76], carbide-coated crucibles were demonstrated to be non-wetting with solidified pyrochemical salts. In addition, no significant adhesion problems were observed in compatibility tests conducted with $CaCl_2$-based and salt systems and equimolar KCl-NaCl.

Based on the satisfactory results with in-situ solidification of salts, studies were extended to systems containing molten salts and liquid plutonium. This was conducted to evaluate the materials performance in full-scale implementation. Undesired adhesive properties were observed between the carbide surface layers and the solidified product metal. Metallographic examinations of the interface revealed that the severe wetting observed with bare tantalum did not occur. However, clean phase disengagement between product and crucible was not achieved due to physical adhesion. In that work, the postmortem examinations, including optical metallography and electron microprobe, indicated no reaction products involving the contained plutonium/salt system. There were no reaction zones, and the lack of phase disengagement was due to physical adhesion associated with the texture of the carbide surface, not to surface energy reduction.

The first reported demonstration of carbon-saturated tantalum (C-sat.Ta) for the containment of liquid plutonium was performed by Andelin and coworkers[77] in 1967. They reported a dramatic improvement in the corrosion resistance of tantalum in the saturated condition during long term contact with liquid plutonium.

It is interesting that the saturation processing was actually a serendipitous result of the back diffusion of pump oil during the long term exposure tests conducted with tantalum containment cells. Regardless of the unintended nature of circumstances, that work indicated the potential for C-sat.Ta.

# 6.0 PERFORMANCE TESTING AND EVALUATION OF CARBON-TANTALUM ALLOYS

The positive indications of the computer modeling and the reported experiences of previous investigators justified experimental testing of alloys within the carbon-tantalum system. The experimental campaign involved examinations of three distinct alloys; the parent metal substrate with TaC coating, the parent metal with $Ta_2C$ coating, and the C-sat.Ta. All preparations were done by preparing surface coatings via carburization. The $Ta_2C$ coated material and the C-sat.Ta specimens were then subsequently heat treated to digest the coating into the substrate (saturation processing). The $Ta_2C$ coating was produced by heat treating the material until the gold color was gone. The color change indicated that the TaC was no longer present at the surface. Microprobe examinations confirmed that the $Ta_2C$ coating was left as the surface phase. The C-sat.Ta alloy was formed by more extended saturation times. The parts were heat treated in inert environments until the coating was completely dissolved into the substrate and carbide was only present as the precipitated species after cooling from the saturation temperature.

## 6.1 Thermal cycle tests

The first experimental tests involved cycling the materials over the thermal profile of a typical processing operation. The maximum temperature was $900^{o}C$ and the specimens were suspended in a flowing argon atmosphere. All coatings retained their integrity over 5 thermal cycles.

However, spallation was observed in all the coated specimens after 25 thermal cycles. The C-sat.Ta showed no effects due to thermal cycles in the initial testing or in any usage to date.

### 6.2 Salt release and liquid metal containment tests

Crucibles were produced with internal tapers for containment testing with pyrochemical salts. Small scale crucibles in the order of 100ml capacity were machined to a 7° internal taper. Larger, full scale crucibles were spun with a 3.5° internal taper. The large scale crucibles were prepared with the TaC surface coating and also with the $Ta_2C$ surface. The $Ta_2C$ coating was produced by a partial coating dissolution technique described later in this report.

Figure 10 shows a photograph of a large scale carburized crucible (TaC surface layer retained) used in these tests. The small scale crucibles were filled with salt and reacted at 900°C. The NaCl-KCl equimolar salt composition released without effect. The $CaCl_2$ was difficult to release. The salt was broken away from the crucible and visual examination revealed no reaction zone. Figure 11 shows the $CaCl_2$ released from the same crucible appearing in Figure 10. The crucible after the salt release is shown in Figure 12.

The containment tests were repeated with the salt and metallic calcium. Microprobe examinations were conducted and no reaction zones were found. The calcium as well as the solidified salt disengaged from the coated surfaces.

Figure 10. A large-scale tantalum crucible with TaC coating produced by packed bed reaction at 1553°C.

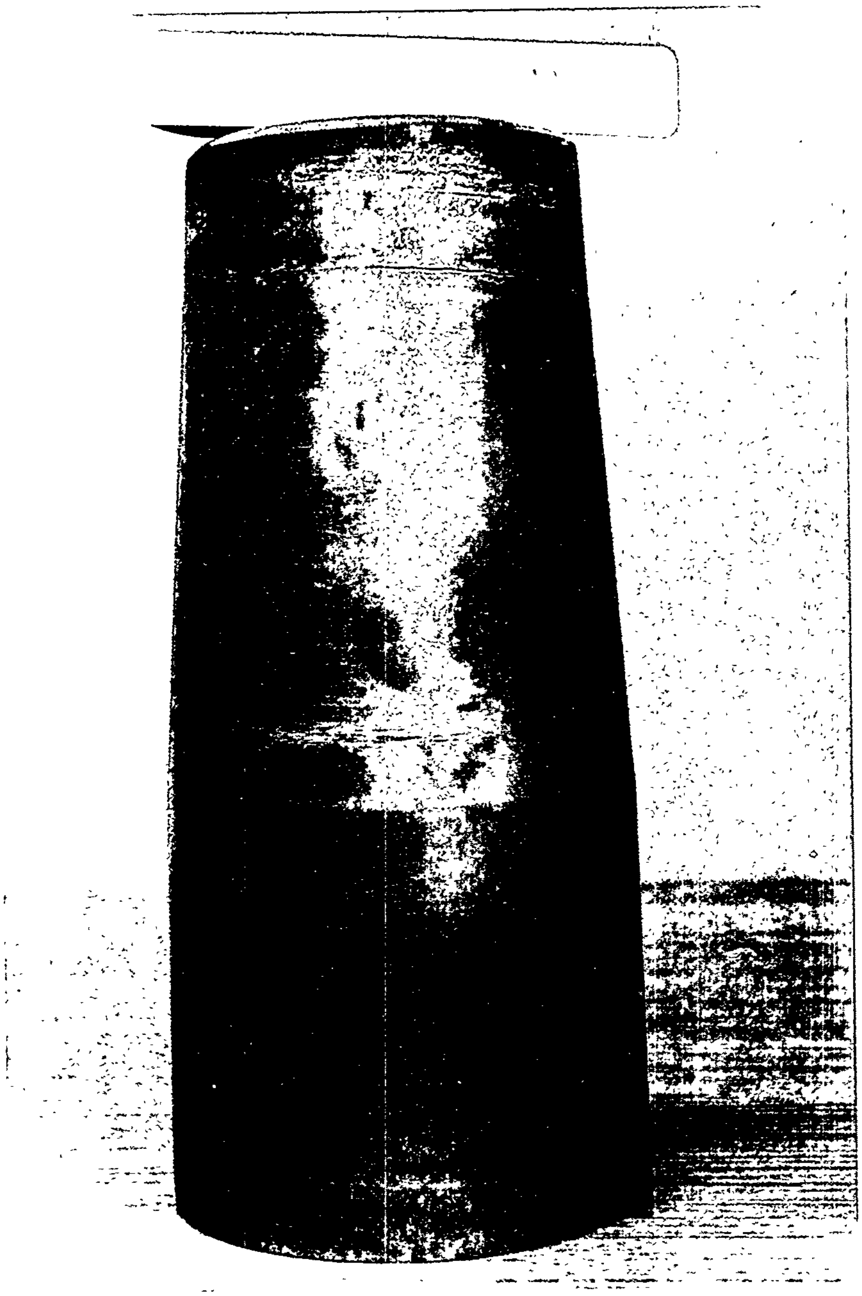

Figure 11. The integral plug of $CaCl_2$ released from the TaC coated crucible after contact at 900°C.

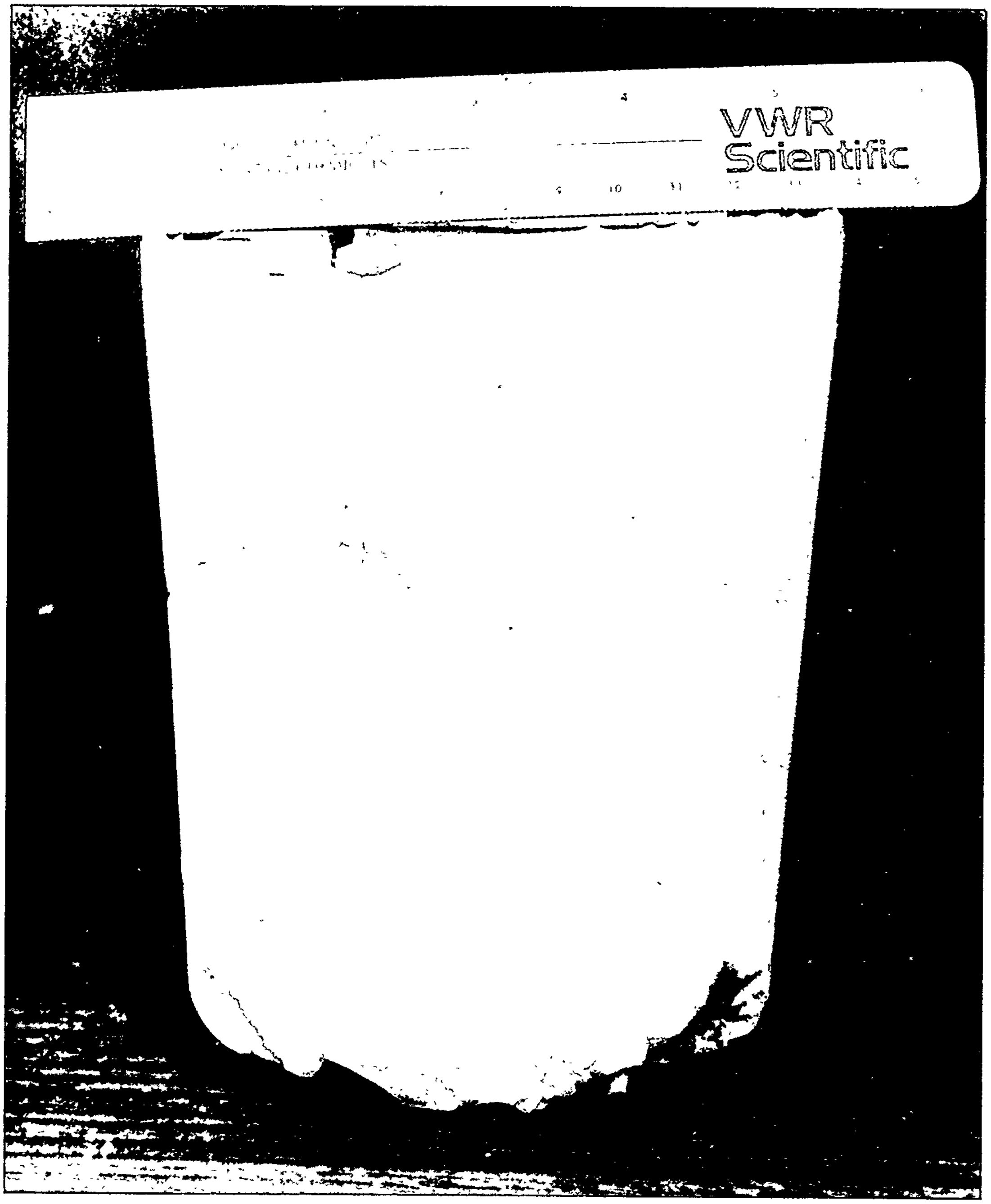

Figure 12. Interior of large-scale crucible after salt release. Note that the salt disengaged successfully and the coating was preserved.

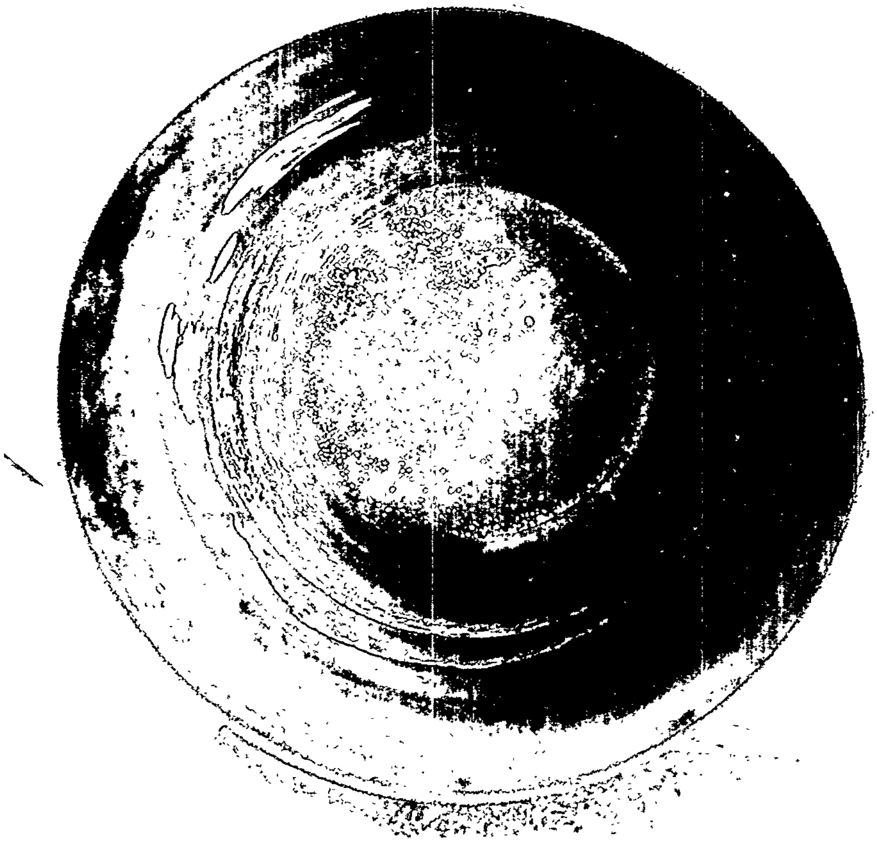

## 6.3 Exposure tests with liquid plutonium

The coated crucibles were subjected to plutonium and salt containment tests at 900°C. The coated crucibles did not perform well when liquid plutonium was allowed to solidify in place. The TaC coated crucible released the salt without difficulty. The solidified metal product was also easily removed. The recovered metal was an integral button. However, the TaC coating adhered to the solidified plutonium and was removed from the crucible surface. Microprobe examinations were conducted on both the metal button and the crucible in the post-mortem condition. The results showed that the coating separated at the TaC/$Ta_2C$ interface. The TaC was bound to the plutonium and the $Ta_2C$ layer remained on the inner crucible where the metal resided as liquid. The crucible after the plutonium/salt containment test is shown in Figure 13. In Figure 14 the plutonium button product is shown with remnants of the TaC layer adhering to the surface.

In the case of the Ta2C coated crucible, the salt released with clean disengagment, but the liquid plutonium metal wet the inner crucible wall and the crucible was destroyed in recovering the solidified metal product.

Straight-wall TaC and $Ta_2C$ coated crucibles and a C-sat.Ta crucible were processed for simultaneous plutonium containment over extended time. All three crucibles were loaded with plutonium and heat soaked for 200hr at 765°C. After the exposure tests, both coated crucibles were lined with solidified plutonium which wet the internal surface at elevated temperatures. Phase disengagement was not realized in removal of plutonium from the coated cells.

Figure 13. The TaC coated tantalum crucible after high-temperature containment of molten salt and plutonium. Note that coating disengaged from part of the inner crucible surface.

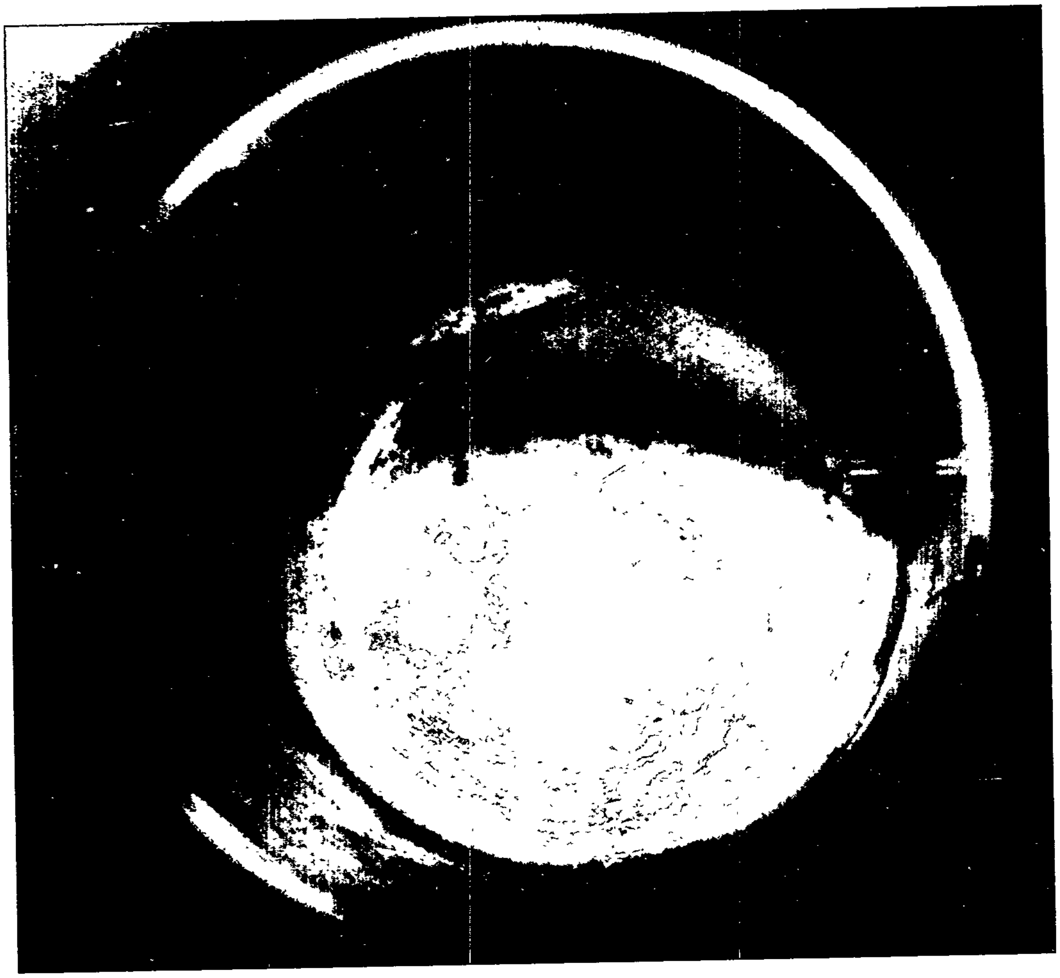

Figure 14. The plutonium button product with remnants of the TaC layer adhering to the surface.

The bulk plutonium separated by shrinkage due to the allotropic transformations upon cooling. However, the $Ta_2C$ crucible was lined with intractable plutonium layer. The TaC crucible showed the same behavior as before where the TaC coating reported to the solidified metal product.

The C-sat.Ta crucible showed no indications of wetting by liquid metal, and discrete phase disengagement was realized. A small quantity of plutonium was found on the wall due to physical adhesion. The plutonium released from the crucible and metallographic examinations confirmed clean phase disengagement. No other material has been found to be as impervious to liquid plutonium that the C-sat.Ta demonstrated in this investigation. A photograph showing the three crucibles is provided in Figure 15. The C-sat.Ta cell is adjacent to the removed plutonium plug. The TaC cell is in the middle and the $Ta_2C$ coated cell is on the far right.

## 6.4 Service demonstration in pyrometallurgical operations

Based on the results of the initial testing campaign, the coated materials were disqualified from consideration as viable construction materials. Service demonstration testing was continued on the C-sat.Ta alloy. The first demonstration of this material for service hardware in plutonium processing was conducted in this work and was reported in a previous publication[78]. The initial demonstration was conducted in the most severe plutonium processing environment: full-scale reduction processing to convert $PuO_2$ to metal. The service conditions included multiple high-temperature exposures to liquid plutonium and calcium metal, molten salts, and chlorine gas at elevated temperatures.

Figure 15. The three crucibles simultaneously exposed to molten plutonium for 200hr at 765°C. From left to right: C-sat.Ta, TaC coated tantalum, $Ta_2C$ coated tantalum. Satisfactory phase disengagement was achieved in the case with C-sat.Ta only.

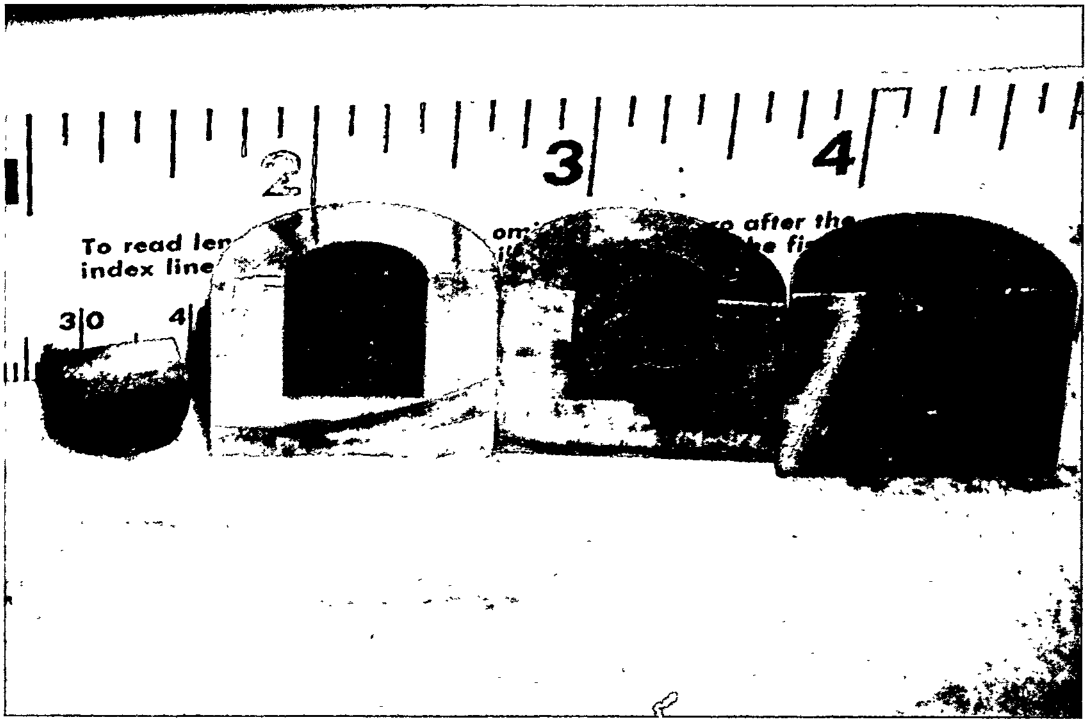

Gas phase corrosion investigations[79] were conducted on the C-sat.Ta stirrer tested in this campaign. The performance data acquired in the service tests established preliminary quantitative information on the corrosion resistance of C-sat.Ta to chlorine gas.

Results were obtained in a comparison of corrosion rates observed with bare tantalum and the C-sat.Ta alloy subjected to similar exposures. In these tests, the materials were subjected to ~1600min exposures to 99.5% pure chlorine (Matheson Gas Products) at 850°C. The chlorine attack was evidenced by the appearance of transgranular corrosion features. The demonstration also involved exposures to a molten $CaCl_2$-based salt phase and liquid plutonium metal.

Cross sectional thickness reductions were measured on metallographically mounted specimens. In the regions of most severe attack, the C-sat.Ta alloy showed a >60% improvement in retained cross sectional thickness. Based on interpretations of micrographs, the corrosion effects of chlorine were transgranular. Therefore, the enhanced corrosion resistance cannot be attributed solely to the grain boundary occupancy by carbide inclusions. The constitution of the granular regions presented greater transgranular corrosion resistance than that of the unalloyed material.

The pictures in Figure 16 show the condition of the C-sat.Ta stirrer blade after the demonstration test. For comparison, a blade from the same relative position was removed from a standard tantalum stirrer after similar exposures in service.

In the mentioned study of oxidation resistance at Battelle, the retention of carbon within the matrix composition was identified as a corrosion inhibiting agent. However, in that work, only the overall carbon to tantalum ratios were recorded and associated with variations in performance. No distinction was made regarding dissolved carbon vs. precipitated carbides within the alloy system. Within the present work, it was demonstrated that retention of a supersaturated alloy condition was not practicable for parts of operable dimensions. Therefore, although not distinguished, the composition of alloys examined in that previous work were in all probability two-phase microstructures as were examined here.

It is reasonable to assume that the improved corrosion resistance to high-temperature corrosive gases, including both chlorine and oxygen, could be an attribute of dispersed carbide inclusions within the granular regions.

Figure 16. The C-sat.Ta stirrer blade after the demonstration test (top photograph). The material on the blade is solidified plutonium which was held on by physical adhesion. The effects of transgranular corrosion are visually apparent at the edges. Some plutonium metal solidified in place and appears adjacent to the transgranular reaction zone. A section removed from a standard tantalum stirrer blade is shown for comparison (bottom photograph). NOTE: To facilitate comparison, both photographs are at the same magnification.

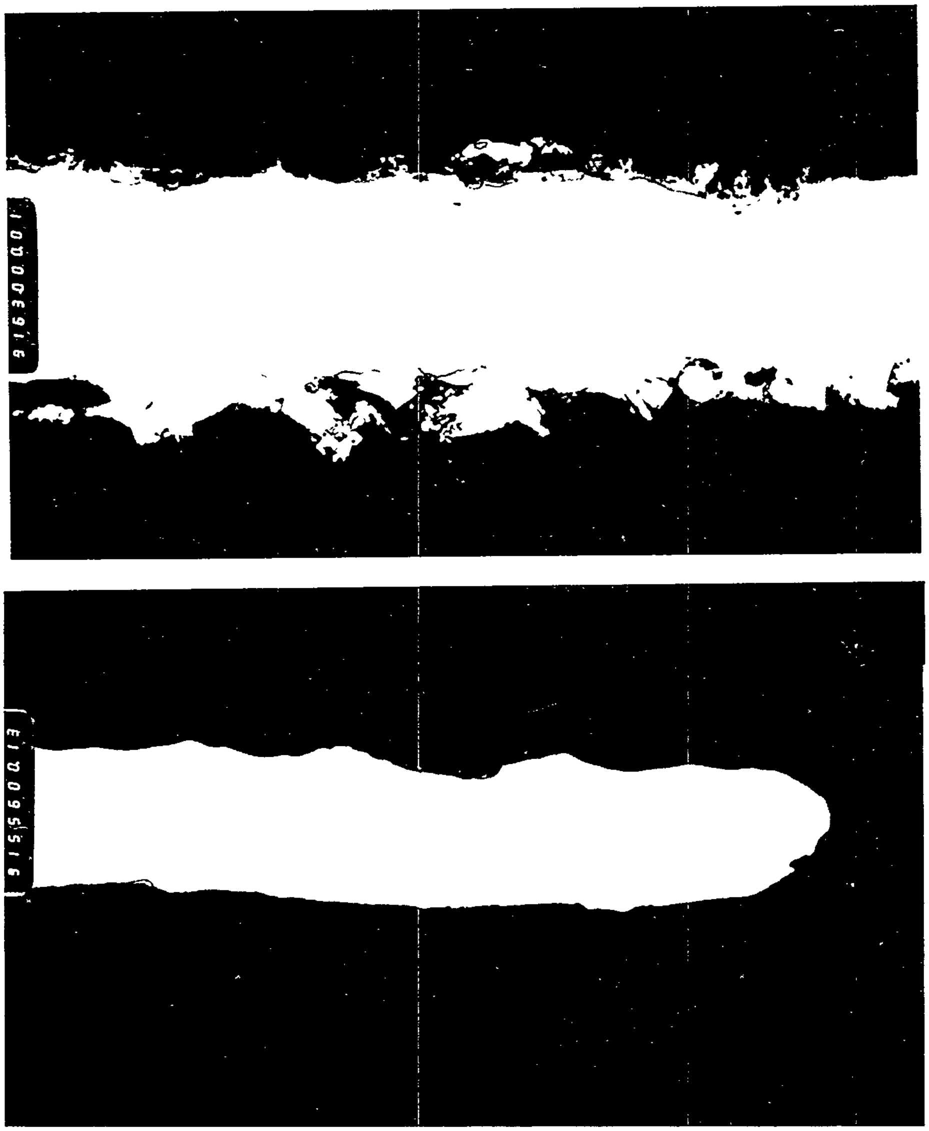

# 7.0 CARBIDE GROWTH KINETICS

A strategy has been developed to elucidate kinetic data on the growth of carbide precipitates from the supersaturated condition. Specifically, specimens possessing the carbon solubility at a high carburization temperature (1800°C) were heat soaked to allow complete saturation of carbon into the substrate while preserving excess carbide coating at the surface. Once the matrix was fully loaded with interstitial carbon, the specimens were rapidly quenched. The carbon in solution at the elevated temperature reported to the equilibrium microstructure as nucleated carbide inclusions. Metallographic examinations were conducted to confirm uniform microstructures for all specimens in the quenched condition. The coating and the non-uniform adjacent zone were machined off each specimen prior to subsequent aging treatments. The subsequent processing involved first re-equilibrating the specimens at the initial elevated temperature, quenching to a secondary temperature, and then allowing incremental elapsed times for aging. The system re-nucleated upon quenching to the aging temperature where it was supersaturated. The precipitates became enlarged over time at the aging temperature.

After a prescribed elapsed aging time, the specimens were rapidly quenched to room temperature and the precipitate size in each specimen was quantitatively surveyed metallographically. This experimental strategy was based on the principles described by Avrami[80]. It is well-suited for this particular alloy system where supersaturated conditions can be achieved at relatively high aging temperatures.

## 7.1 Instrumentation, materials and equipment

The furnace used in the production of specimens for the precipitation studies was an RF induction heater designed and constructed at the Basic Industrial Research Laboratory (BIRL) of Northwestern University, Evanston, IL. The furnace was evacuated via a 2-stage pumping station equipped with a rotary vane mechanical pump (Leybold-Heraeus model S60A) and a high-vacuum Roots-type blower (Leybold-Heraeus "RUVAC" model D60). Both pumps were charged with Fomblin Y25/5 oil.

Gas mixture compositions and flow rates were controlled by MKS brand "μ-bar" thermal mass flow controllers. Radio frequency analysis was conducted in real time using a Tektronix model 2246 100MHz oscilloscope. Gas compositions over the specimens were surveyed in real time using an INFICON IPC200 quadrupole mass spectrometer. Specimen temperature was measured with an IRCON "Mirage" two-color pyrometer with a 0.01 second response time.

The two-color pyrometer was linked to a temperature measurement control system by Square-D. This temperature measurement control system accepts emissivity data pairs from two wavelengths and corrects the brightness temperature according to the emissivity data entry. Furnace temperatures and thermal profiles were controlled using a EUROTHERM programmable furnace controller.

Specimens were examined with a Leco model 300 metallograph. Direct optical measurements of metallographic images were made using a measuring magnifier equipped with filar reticle (Bausch and Lomb model 81-34-35).

Reflected light images for image analysis were taken with a Kodak "Mega-Plus" model 4.2 camera and captured with Image 1.44VDM-F software produced by the National Institute of Health.

The image analysis was conducted with Photoshop version 2.5 (Adobe Systems, Inc.) on a Macintosh Quadra 950 computer. The images collected in this campaign approached a volume of 300Mb. To manage this quantity of computer data, the Quadra was linked to an optical disk storage system, the "Pinnacle Micro" model PMO-1300.

To confirm the accuracy of image analyses conducted with the Photoshop software, 54 images were analyzed a second time using a dedicated image analyzer, the Princeton Gamma Tech "Imagist". The analyses all agreed to within 0.2%.

The tantalum used in this campaign has been acquired from Fansteel. It is 0.318cm diameter rod stock, arc-cast and annealed, 99.9% minimum purity. The rod was cut into 3.0cm long specimens using a low speed diamond saw. The manufacturer provided the results of a batch analysis which are presented in Table 4. An extensive elemental analysis has been conducted at LANL to determine the metallic composition (see Table 5). The two analyses are in good general agreement. The value for nickel was higher in the Los Alamos analysis but was reported as less than 100ppm in both cases.

Table 4. Manufacturer's analysis of reactant tantalum used in these experiments.

| ELEMENT | LEVEL (PPM) | ELEMENT | LEVEL (PPM) |
|---|---|---|---|
| CARBON | 14 | OXYGEN | 59 |
| NITROGEN | 24 | HYDROGEN | <5 |
| TUNGSTEN | <50 | NIOBIUM | <10 |
| ZIRCONIUM | <10 | MOLYBDENUM | <10 |
| TITANIUM | <10 | IRON | 50 |
| NICKEL | 20 | SILICON | <10 |
| MANGANESE | <10 | CALCIUM | <10 |
| ALUMINUM | <10 | COPPER | <10 |
| TIN | <10 | CHROMIUM | <10 |
| VANADIUM | <10 | COBALT | <10 |
| MAGNESIUM | <10 | TANTALUM | BALANCE |

Table 5. Metallic content of tantalum based on analyses conducted at Los Alamos.

| ELEMENT | LEVEL (PPM) | ELEMENT | LEVEL (PPM) |
|---|---|---|---|
| SILVER | <1 | ARSENIC | <10 |
| BARIUM | <500 | BERYLLIUM | <2 |
| BISMUTH | <1 | CADMIUM | <1 |
| CERIUM | <200 | COBALT | <1 |
| CHROMIUM | <10 | CESIUM | <200 |
| COPPER | 15 | DYSPROSIUM | <200 |
| ERBIUM | <200 | EUROPIUM | <200 |
| GALLIUM | <500 | GADOLINIUM | <500 |
| GERMANIUM | <4 | HAFNIUM | <2 |
| MERCURY | <7 | LANTHANUM | <100 |
| LITHIUM | <2 | LUTETIUM | <100 |
| MAGNESIUM | <30 | MANGANESE | <5 |
| MOLYBDENUM | <1 | NIOBIUM | 8 |
| NEODYMIUM | <500 | NICKEL | 94 |
| LEAD | 5 | PALLADIUM | <1 |
| PRASEODYMIUM | <100 | PLATINUM | <5 |
| RUBIDIUM | <1 | RHENIUM | <200 |
| RHODIUM | <100 | RUTHENIUM | <1 |
| ANTIMONY | 2 | SELENIUM | <20 |
| SAMARIUM | <500 | TIN | 2 |
| STRONTIUM | <10 | TERBIUM | <100 |

Table 5.(Continued) Metallic content of tantalum based on analyses conducted at Los Alamos.

| | | | |
|---|---|---|---|
| TELLURIUM | <10 | THORIUM | <100 |
| TITANIUM | <5 | THALLIUM | <500 |
| THULIUM | <100 | URANIUM | <1 |
| VANADIUM | <5 | TUNGSTEN | 11 |
| YTTERBIUM | <500 | ZINC | 7 |
| ZIRCONIUM | 6 | TANTALUM | BALANCE |

## 7.2 Specimen preparation

The discussion presented herein focuses on the specimens produced to study the precipitate growth mechanism, specifically, to extract kinetic data on carbide growth behavior from supersaturated solid solutions of carbon in the tantalum matrix.

### 7.2.1 Description of the targeted microstructure

The carbide generated from an undercooled condition of the solid solution phase is $Ta_2C$, the most metal-rich intermediate composition in the tantalum-carbon alloy system. In general, the strategy involves the preparation of solid solutions by dissolving carbon into the tantalum matrix and subsequent aging treatments at a lower temperature (where the matrix phase is supersaturated) to invoke the production/growth of the carbide.

By conducting incremental aging treatments varying in time and temperature, the rate of precipitate growth can be surveyed and modeled.

The experimental campaign was comprised of a suite of processing treatments designed to provide rate data at 3 temperatures. This involved multi-stage thermal processing for each specimen.

### 7.2.2 Temperature measurement

High precision temperature measurement was required in this work. Therefore, before the specimens were processed for the kinetic data, a temperature measurement technique was refined. Based on the temperature regime of the campaign and on the configuration of the radio frequency induction heater, two-color infrared pyrometry was selected.

In the majority of previously published studies of high-temperature phase behavior of the tantalum-carbon system, radio frequency (RF) induction heating was used similar to this work. However, outdated temperature measurement techniques were used in all previously published investigations of this system. Specifically, traditional "single-color" pyrometry was used. This conventional method of temperature measurement requires emissivity corrections to the brightness temperature as recorded off the specimen surfaces.

The emissivity of a material at a specific wavelength is extracted by the following relationship:

$$\frac{1}{T_{\mathrm{blackbody}}} - \frac{1}{T_{\mathrm{surface}}} = \frac{\lambda \ln(e_\lambda)}{C_2}$$

where $e_\lambda$ is the emissivity at the pyrometer's wavelength, and $C_2$ is the second radiation constant (1.43847 cm-°K). Typically, the brightness temperature is compared to the temperature recorded from within a black body hole in the specimen and the emissivity correction factor is generated from the above expression.

There are several inherent limitations of traditional single-wavelength pyrometry; If partial obstructions such as dust or condensate enter the cone of vision, a false temperature measurement is inevitable.

The emissivity of the deliberate surfaces such as the sight window itself must be accommodated in corrections to the apparent intensity. Additionally, since the temperature is measured solely by intensity at a single wavelength, if the target region moves partially out of view, the total intensity is reduced and again an incorrect measurement results.

To eliminate the inherent problems with traditional pyrometry, a dual-detector, two-color IR pyrometer (IRCON Inc.) was used in this work. With a 10ms response time, this pyrometer was ideally suited for recording temperatures during rapid quench rates.

This specific two-color pyrometer incorporates two separate IR detectors viewing the same area at the same time and surveying two wavelength being emitted from the target simultaneously. It is the ratio of radiant energies at the two wavelengths that is used to directly measure the specimen temperature. The principles of two-color pyrometry and the operation of this specific instrument are described in detail by Lappe[81].

Using a two-color pyrometer, the acquisition of emissivity correction data for individual wavelengths is superfluous. Alternatively, an emissivity slope correction is conducted to refine the temperature measurement accuracy. This is not specific to either wavelength individually but involves a constant correction factor applied to the measured signal ratio to correct the instrument calibration for slight inequalities in the spectral emissivity of the specimen at the wavelength pair.

The pyrometer used in this study accepts a minimum cone of vision terminating on a 1mm surface. Therefore, if a black-body hole was machined into each specimen, it would need to be a minimum of 1mm diameter, a significant fraction of the specimens' 0.318cm total diameter. Due to the reduced wall thickness around the black-body, the temperature measurements via this technique would not be representative of the bulk material[82]. Alternatively, temperature measurements would need to be taken off the specimen surfaces. This required acquisition of emissivity data for the surface phases. Although published data exist for the emissivity of tantalum and its carbides, this quantity is strongly dependent on surface texture and therefore was measured for the specific materials used in this campaign.

To resolve any problems relating to optical temperature measurements of the surfaces, emissivity slope correction factors were determined for both tantalum and TaC, the two surfaces presented to the pyrometer during the experimental work on precipitation kinetics. This was conducted by reading both the black-body and surface brightness temperatures off a specifically machined specimen. This dedicated specimen was a 1.27cm diameter tantalum rod of the same constitution as the smaller specimens used in the subsequent parts of this campaign. The emissivity specimen, like all the tantalum specimens, was polished to a #32 surface finish to ensure identical textures throughout the materials used in this campaign.

A 1.2mm diameter black-body hole was machined 2cm into the depth of the dedicated emissivity specimen. This accounted for a relatively small fraction of its 1.27cm total diameter.

The wavelengths selected in this work were 0.7 and 1.0 microns. The selection of short (near infrared) wavelengths meant that sufficient optical thicknesses of the surface phase were present after minimal elapsed carburization times. (According to carbide surface formation kinetics published by Krikorian et al., more than a micron of TaC thickness would be present within the first four minutes at 1800°C). The advantage of using two relatively close wavelengths was to minimize temperature measurement errors which might have occurred due to wavelength-specific interference by unanticipated partial obstructions such as dust. The quartz glass used in the sight window is considered nearly a gray-body absorber and therefore did not present any wavelength-specific attenuations.

An inherent advantage of two-color pyrometry is that graybody obstructions do not affect the accuracy of the temperature measurements. Since the temperature is measured by the ratio of the intensities at two wavelengths, if the partial obstruction attenuates both wavelengths equally, the measurement is unaffected.

The brightness (surface) temperature measurement was effectively corrected by simultaneously measuring the emissivity effects at a pair of wavelengths using the "E-slope" function of the pyrometer. Corrections were established for both the bare tantalum and for TaC (the outermost carbide layer after carburization of the specimen). The E-slope was experimentally determined by alternating the sight picture between the black body (E-slope = 1) and the surface. The E-slope was adjusted until the measured temperatures matched. This was done over a range of temperatures from 1600-2050°C.

As anticipated, the correction factor was unchanged over the range of temperature surveyed. A value of E slope=1.055 was found for both the metal and the carbide surfaces. These observations are consistent with the extremely similar emissivities[83] of those materials.

### 7.2.3 Selection and refinement of carburization technique

Prior to selecting the carburization technique best suited for the kinetic studies, a review was conducted to assess the current methods of preparation for tantalum carbide surface coatings. In preliminary work, both gas phase carburization and packed bed carburization was demonstrated.

The selection of the gas phase process was based on the advantage of being able to retain the specimens at elevated temperatures while removing the carbonaceous reactant media via remote methods (the use of mass flow controllers).

In the packed bed method of carburization, the specimen would need to be recovered, which would involve cooling to room temperature, and physically removed from the carbon bed media in order to conduct subsequent thermal processing under inert conditions.

In the demonstration work with packed bed carburization, the specimens were reacted with activated carbon powder (DARCO-G60 produced by American Norit Co. and distributed by J.T. Baker, Inc.). The specimens were press fit into the carbon powder media which was contained within graphite fixtures and heated under flowing argon at temperatures ranging from 1400 to 1600°C. Due to the lack of solid solubility at 1400°C, the specimens prepared at that temperature did not possess any internal precipitates of the $Ta_2C$ carbide phase. The carbide precipitates were observed in the specimens processed at higher temperatures. A comparison of specimens prepared at 1600°C by both packed-bed and gas phase carburization revealed indistinguishable microstructures. The carbide precipitates form from the supersaturated condition produced upon cooling from temperatures over which solid solubility is measurable. The absence of these carbide precipitates in specimens processed at 1400°C indicate the solubility of carbon in tantalum is insignificant at that temperature. Any carbon contained in the solid solution phase at that temperature was retained without the formation of a carbide interstitial phase during cooling to room temperature.

The reaction with methane at the specimen surface is presented below:

$$CH_4 + Ta^\circ \Rightarrow Ta_2C + 2H_2$$

which is followed by the further reaction with the substrate:

$$TaC + Ta^\circ \Rightarrow Ta_2C$$

### 7.2.4 Hydrogen evolution during carburization

The reaction with methane indicates a high effective hydrogen activity at the surface. However, negligible dissolution of hydrogen has been observed in gas-phase carburization by previous workers[84]. The lack of concurrent hydrogen dissolution can be understood with consideration of the retrograde solubility reported by independent investigators.

Figure 17 shows the solubility of hydrogen in tantalum as a function of temperature. Figure 18 shows a construction of the tantalum-hydrogen binary phase diagram. In that phase diagram, the miscibility gap and isobars were experimentally determined[85], although the individual data sets are not presented.

### 7.2.5 Details regarding coating thicknesses

A computer spreadsheet was generated to calculate the carburization times for tantalum specimens of specified geometry (see Table 6).

Figure 17. Temperature dependence of hydrogen solubility in tantalum metal. Note the inverse relationship between temperature and solubility. The data reflect two independent investigations ( ○ Mallett and Campbell[86], △ Seifert and Gotta[87]).

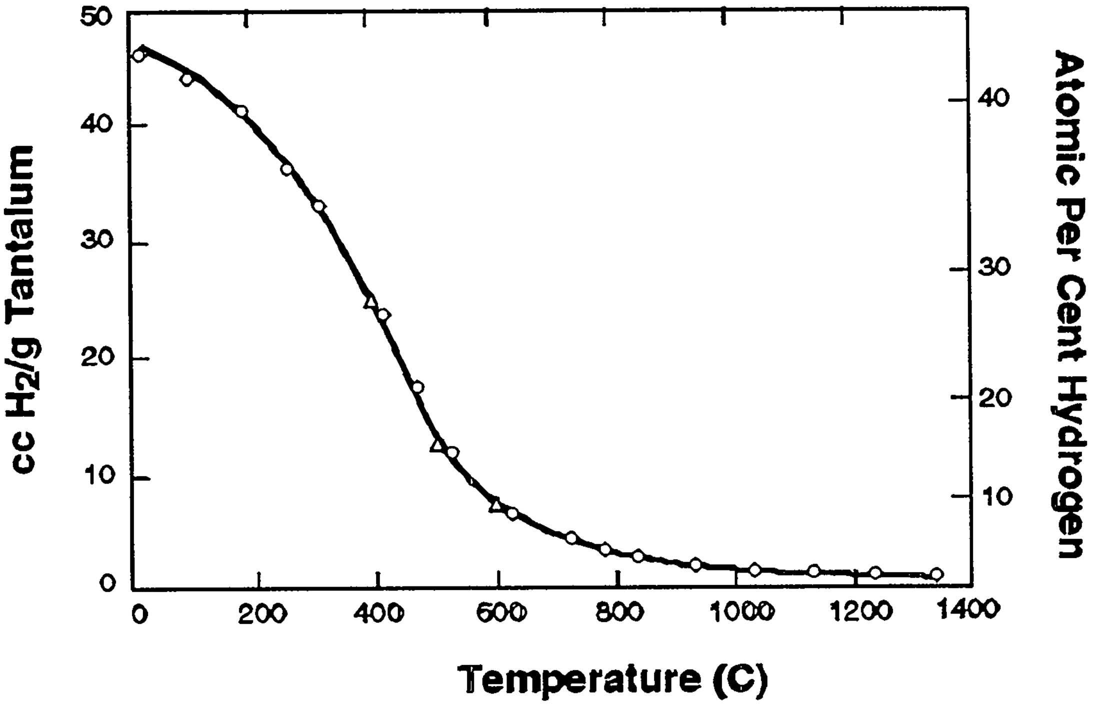

Figure 18. Partial phase diagram for the tantalum-hydrogen system.

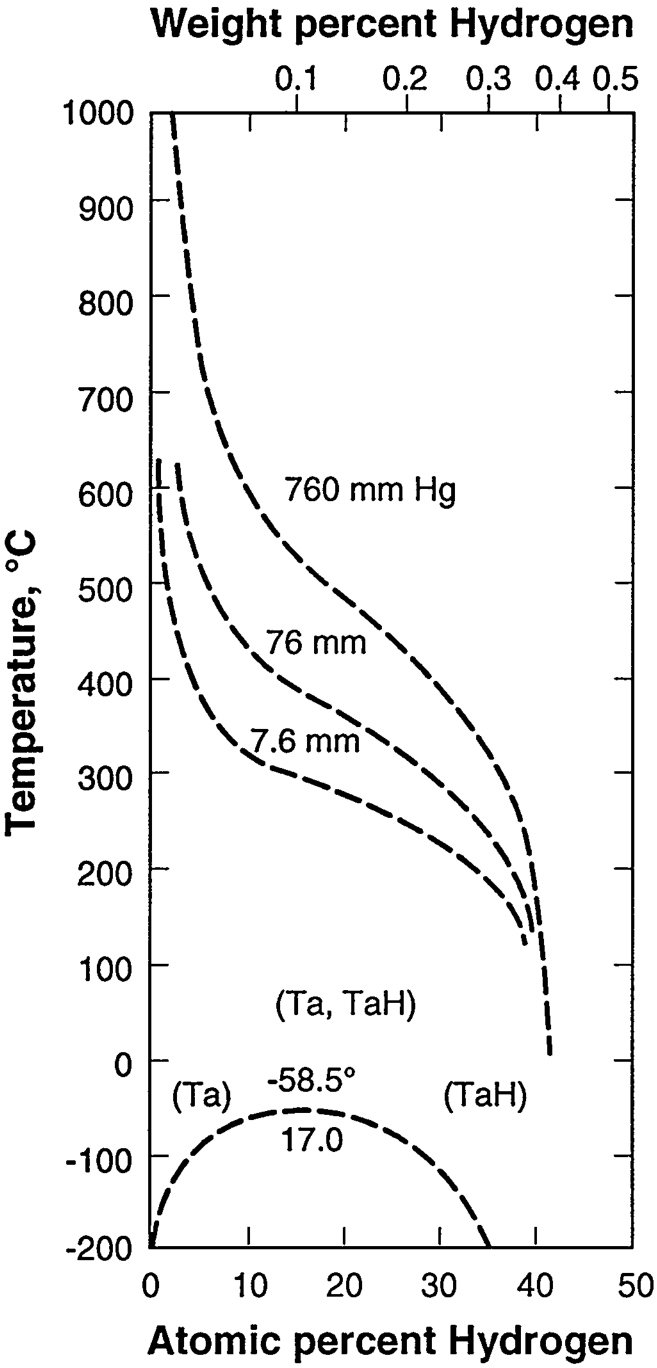

Table 6. Calculated carburization times based on Krikorian[60] data on carbide layer growth rates for TaC and $Ta_2C$. The larger specimen (1.27cm dia.x 3.0cm ht) is for the emissivity measurements. The smaller specimens (0.318cm dia. x 3.0cm ht.) are to be used in the campaign to acquire kinetic data on carbide precipitation growth. Saturation processing was not conducted on the larger diameter specimen used for TaC emissivity measurements. These values neglect the thickness reductions associated with simultaneous coating dissolution.

| SPECIMEN DIAMETER (cm) | TEMP. (°C) | TIME (hrs) | TaC LAYER MICRONS | $Ta_2C$ LAYER MICRONS | C:Ta MOLE RATIO |
|---|---|---|---|---|---|
| 1.27 | 1800 | .25 | 5.96 | 3.39 | 0.018 |
| 1.27 | 1800 | .50 | 8.43 | 4.79 | 0.025 |
| 1.27 | 1800 | .75 | 10.3 | 5.87 | 0.030 |
| | | | | | |
| 1.27 | 1700 | .25 | 3.85 | 2.10 | 0.011 |
| 1.27 | 1700 | .50 | 5.44 | 2.97 | 0.016 |
| 1.27 | 1700 | .75 | 6.67 | 3.64 | 0.019 |
| | | | | | |
| 0.318 | 1800 | .25 | 5.96 | 3.39 | 0.281 |
| 0.318 | 1800 | .50 | 8.43 | 4.79 | 0.397 |
| 0.318 | 1800 | .75 | 10.3 | 5.87 | 0.486 |
| | | | | | |
| 0.318 | 1700 | .25 | 3.85 | 2.10 | .180 |
| 0.318 | 1700 | .50 | 5.44 | 2.97 | .254 |
| 0.318 | 1700 | .75 | 6.67 | 3.64 | .311 |

The coating thicknesses were taken in concert with the specimen surface areas to calculate the predicted moles of carbide present after carburization. The calculations in the template were extracted from data from the work of Krikorian et al.[60] which involved packed bed carburization. The rate constants for layer growth of both carbides according to Krikorian are presented below:

$$\boldsymbol{K}(\alpha\text{-Ta}_2\text{C}) = 1.94\text{EXP}(-77.6\text{kcal/mole/RT})\ \text{cm}^2/\text{sec}$$

$$\boldsymbol{K}(\text{TaC}) = 1.27\text{EXP}(-71.2\text{kcal/mole/RT})\ \text{cm}^2/\text{sec}$$

The preservation of the coatings during the saturation step has been considered. Based on the vaporization behavior of the carbides[88], no significant loss of the coatings was anticipated to occur during the saturation heat soaks. The possibility of de-carburization[89,90] has also been considered. De-carburization involves reactions which can occur between the carburized surface and oxygen, if present, as an impurity within the furnace atmosphere. To obviate this potential problem, an excess coating was generated on each specimen, and metallographic examinations confirmed the presence of excess coating after carburization/saturation processing.

The presence of an excess coating will provide several desired effects:

1) To negate de-carburization problems by providing sacrificial carbide (as mentioned above). Although the furnace atmosphere will be inert gas, a minimal amount of de-carburization can be anticipated by the trace amounts of oxygen which may be present.

With a sufficient excess of coating, some can be lost due to de-carburization without jeopardizing the processing run.

2) To invoke a fixed carbon activity at the substrate/coating interface during the diffusion-controlled saturation process.

3) To provide sufficient optical thickness of the surface coating (TaC) to ensure accuracy in pyrometric temperature measurements.

### 7.2.6 Saturation processing details

Estimated saturation times were calculated using values of $D_o$ and $E_{activation}$ presented in the paper by Powers and Doyle[55]. Independent confirmation of that work has been provided by Fromm and Roy[48] who used the Powers and Doyle diffusion data to calculate saturation times in a study of the solubility limit for carbon in tantalum.

The sufficient level of saturation was established by consideration of the compositional gradient as a function of time during the diffusion process.

A plot appears in the text by Crank[91] describing concentration distributions for a diffusing species within a cylindrical system. The plot shows the concentration as a function of radial position within the cylindrical geometry as a function of time. This has been reproduced in Figure 19.

Figure 19. General plot valid for concentration of a diffusing species within a cylindrical system. In this plot, 'a' is the radius of the cylinder, 'r' is radial position.

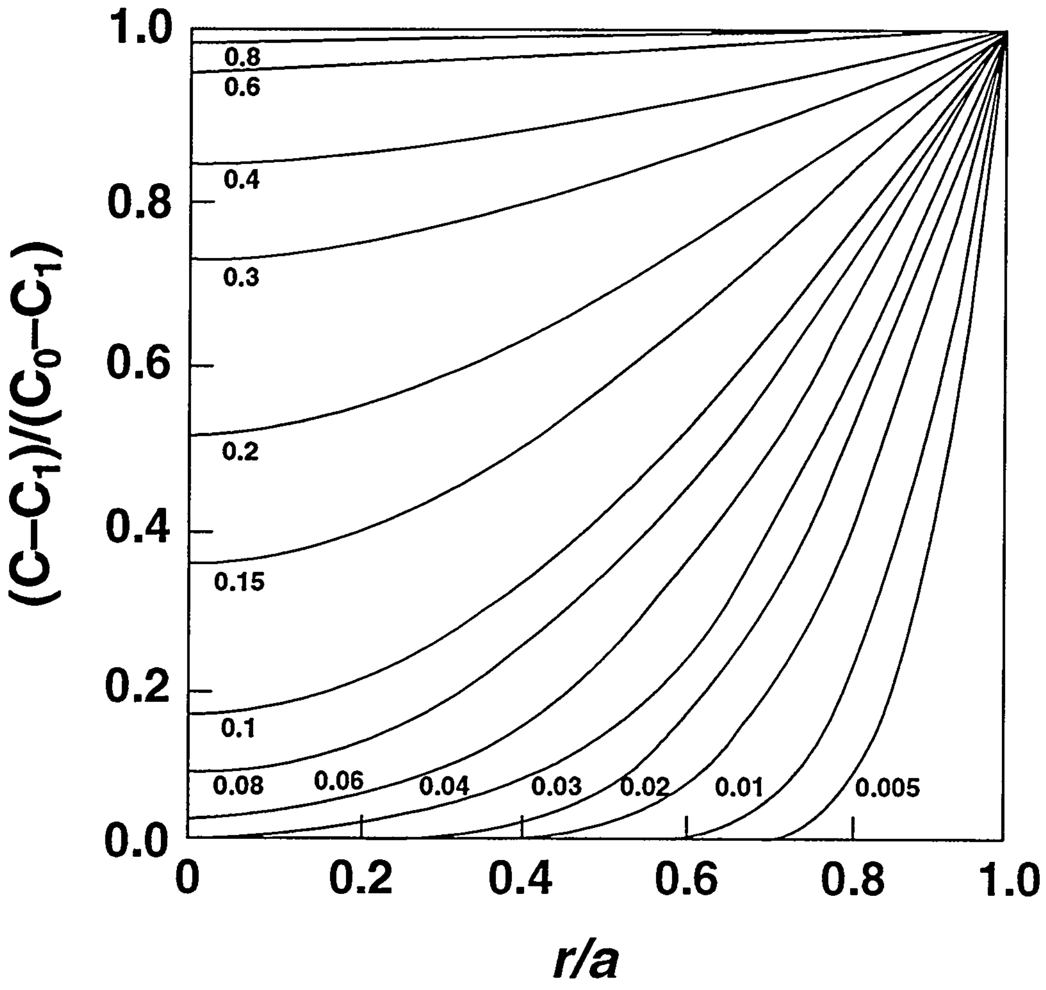

The calculation of a saturation time for specimen preparation was accomplished via the principles of solid state interstitial diffusion. The objective was to allow sufficient time to obviate the compositional gradient over radial distances within the solid rod specimens used in the kinetic studies of carbide precipitation. For these calculations, boundary and initial conditions were assumed for the specimen after a continuous carbide coating was produced. The composition of carbon in tantalum at the coating/substrate interface was taken to be equal to that defined by the terminal carbon solid solubility at the saturation temperature. In the initial set of calculations, this value for composition was taken from the solvus line in the carbon-tantalum binary phase diagram presenting both a boundary condition and an initial condition:

$$C = C_o \quad \text{for} \quad r = a,\ t \geq 0$$

Where 'C' is the carbon composition at a specific radial position, '$C_o$' is the solid solubility of carbon in tantalum at the saturation temperature, 'a' is the complete radius of the solid rod specimen, and 'r' is fractional radius (r = a is the position at the coating/substrate interface). Based on the principle of chemical equilibrium, the activity of carbon must be equal across the substrate/coating interface. Therefore as long as the coating is present during the saturation, the activity will be fixed at one boundary. Another assumption defining an initial condition is that carbon was absent from the interior of the specimen at the onset of saturation processing:

$$C_1 = 0 \quad \text{for } 0 \leq r < a, \quad t = 0$$

During the saturation process, the concentration changes with time and position based on the diffusion behavior of the interstitial carbon. Therefore the composition in terms of the carbon content can be expressed in general:

$$C \equiv f\ (r,t\ )$$

The diffusion equation provided by Crank assumes a uniform initial composition throughout the material. The uniform initial composition is taken as zero for the present case. Crank provided a specific expression for the compositional gradient within solid, cylindrical geometry:

$$\frac{C - C_1}{C_o - C_1} = 1 - \frac{2}{a} \sum_{n=1}^{\infty} \left[ \frac{J_{o(r\alpha_n)} \cdot e^{-Dt\alpha_n^2}}{\alpha_n \cdot J_{1(a\alpha_n)}} \right]$$

where $J_o$ and $J_1$ are Bessel functions with respective arguments in terms of 'r', 'a', and individually specified terms of the summation.

The unitless plot generated by the above diffusion equation appears in the text by Crank and is reproduced in Figure 19. Notice that the individual curves in that plot are labeled for constant $Dt/r^2$ values. The time associated with a specific extent of completeness can be extracted from the position on a selected curve. A detailed description of the equations' functionality was not presented by Crank and was not readily found in other sources. Therefore, in an effort to describe the functionality of the diffusion equation the solution to a first term in the series has been rigorously determined here for illustrative purposes.

Note that with the uniform initial composition set at zero, the left side of the diffusion equation can be abbreviated:

$$C_1 = 0 \therefore \frac{C - C_1}{C_o - C_1} = \frac{C}{C_o}$$

It can be seen from inspection that

$$\frac{\text{Lim}}{t \rightarrow \infty}\left(\frac{C - C_1}{C_O - C_1}\right) = 1$$

Which is the steady-state condition defined. Specifically, in this case, $C_1=0$. With $C_o$ defined as the equilibrium solubility limit, the steady-state condition can be further defined

$$\frac{\text{Lim}}{t \rightarrow \infty}\left(\frac{C - C_1}{C_O - C_1}\right) = \left(\frac{C_O - C_1}{C_O - C_1}\right) = 1$$

However, the rate at which $(C-C_1)/(C_o-C_1)$ approaches unity is dictated by the specific values for 'D', the diffusion coefficient for the interstitial species, and $\alpha_n$. Each root of the Bessell function $J_o$ dictates the value for the corresponding $\alpha_n$ by setting the value for the argument $(a \cdot \alpha_n)$. This is the only variable index within the argument because the numerical value of 'a' is fixed for a specific cylindrical radius. Note that $\alpha_n$ is in units of reciprocal linear distance, $cm^{-1}$ in the present case, which retains the required unitless argument for the Bessell functions.

For the present case 'a'= 0.159cm, and 'r'= 0.0794cm (defined by the dimensions of the specimens used in the kinetic studies).

To perform the calculation at 1800°C, the diffusion coefficient was calculated using the values for the pre-exponential rate constant and the activation energy published by Powers and Doyle:

$$D_{1800C} = 0.0061EXP[^{-38510}/1.987(1800+273)] = 5.309x10^{-7}cm^2/sec$$

The value for the first Bessell function of the first order ($J_1$) was determined by entering the argument of the first Bessell function of zero order ($J_o$) and finding the root. For example, in the first term of the series (n=1):

$$J_{o(a\,\alpha_n)} = 0 \therefore (a\,\alpha_n) = 0.520 \Rightarrow \alpha_n = 15.16$$

$$J_{o(r\,\alpha_n)} = J_{o(0.795\,\bullet\,15.16)} = 0.6710$$

It is noted that the value of $\alpha_n$, which appears in the argument of both Bessell functions, is defined only in terms of the root of the Bessell function of zeroth order, $J_o$.

Solutions for a range of normalized 'r' values, r/a, and $(C-C_1)/(C_o-C_1)$ values constitute the ordinate and abscissa respectively in the construction of the accompanying plot from Crank (see Figure 19).

The solution presented below is for a 13hr period (46800sec) and the location defined by r/a=0.5 which corresponds to an area element at 50% radial penetration.

$$\frac{C}{C_o} = 1 - \frac{2}{0.159}\left[\frac{e^{(-5.136\times10^{-7})(15.16)^2(46800)} \times 0.671}{(15.16)(0.520)}\right] \approx 0.996$$

The calculation indicates that the saturation process is virtually complete at the selected radial position. (A value of 0.9 = $Dt/r^2$ was identified as corresponding to virtually complete saturation in the solubility studies by Fromm and Roy). Subsequent calculations of this type confirmed that virtually complete saturation is achieved over all positions in the specimens with a minimum saturation time of 13hr.

Calculated saturation behavior at selected temperatures is shown in Table 7. The tabulation shows the effect of increasing temperature on the amount of saturation achieved over time.

### 7.2.7 Theoretical carbide precipitate growth rates

The theoretical treatment of precipitation growth rates as described by Porter and Easterling[92] was used to predict the amount of precipitate growth expected as a function of time and temperature during aging. This provided an estimation of heterogeneous precipitate thicknesses as a function of time and temperature during aging. This treatment is based on the growth rate being exclusively dependent on the diffusion rate for the interstitial species, carbon in the present case.

Table 7. Selected times and temperatures with corresponding completeness of saturation. The calculated values indicate the time and temperature dependence on the diffusion-controlled saturation process. Diffusion coefficients for carbon in tantalum were extracted from Powers and Doyle data. Calculations are for a tantalum rod of 0.318cm diameter.

| T($^{o}$C) | CONDITION: $Dt/r^2=0.90$ TIME (hrs) | CONDITION: $Dt/r^2=0.95$ TIME (hrs) |
|---|---|---|
| 2000 | 5.21 | 5.5 |
| 1800 | 11.87 | 12.53 |
| 1700 | 19.06 | 20.12 |
| 1600 | 32.21 | 33.99 |

This is a simplification, but is useful for approximating the aging regime used in this campaign. The expression is presented here:

$$W = \frac{\Delta X_o}{(X_b - X_e)} * \sqrt{Dt}$$

where W is the width of the precipitate in cm, $\Delta X_o$ is the degree of supersaturation - in this case as mole fraction carbon, $X_b$ is the mole fraction carbon in the precipitating phase, and $X_e$ is the equilibrium carbon mole fraction in the matrix at the precipitation temperature.

The diffusion coefficient for carbon at a specified temperature is D ($cm^2/sec$), and t is time in seconds. Based on this formula, a set of calculated precipitation thicknesses were generated and presented in Table 8.

As previously stated, the Porter and Easterling approximation is based on the assumption that there are no other rate effects other than diffusion. This assumption neglects crystallographic effects relating to the degree of coherency between the nucleated precipitate and the matrix. The model used to calculate precipitation behavior assumes complete incoherency - the most favorable interfacial condition for precipitate growth. Any additional crystallographic effects will increase the energy requirement for growth and therefore decrease the growth rate. The experiments conducted in this project reveal the significances of additional rate effects.

Other rate effects in precipitate growth include the degree of overlap between adjacent regions depleted in carbon consumed in the transformation of neighboring carbide precipitates. This is indirectly a function of nucleation site density. The distribution of nucleation sites could also affect growth rate by invoking the impingement of adjacent precipitates. That would be a condition of mutually inhibited growth of both particles.

In this project, precipitate growth rates were extracted directly from experimental data. All rate-affecting contributions to the growth phenomena were reflected in the rate expression which describes observed growth.

However, using the estimation for growth rate based solely on diffusion of the interstitial species, a logical starting point for conducting the aging treatments was established.

Table 8. Calculated precipitation behavior using treatment described by Porter and Easterling. Specimens quenched from 1800°C saturation processing. The carbon solubility data used was from the published work by Rudy and Harmon. The only rate factor is the interstitial diffusion coefficient for carbon in tantalum.

| T(°C) | $D_{(T)}$ $cm^2/sec$ | time (hrs) | Calculated Precipitate width (microns) |
|---|---|---|---|
| 1400 | 5.7E-08 | 2 | 4.4 |
| 1400 | 5.7E-08 | 4 | 6.3 |
| 1400 | 5.7E-08 | 8 | 8.9 |
| 1400 | 5.7E-08 | 32 | 17.8 |
| | | | |
| 1300 | 2.7E-08 | 2 | 3.1 |
| 1300 | 2.7E-08 | 4 | 4.4 |
| 1300 | 2.7E-08 | 8 | 6.2 |
| 1300 | 2.7E-08 | 32 | 12.3 |
| | | | |
| 1200 | 1.2E-08 | 2 | 2.0 |
| 1200 | 1.2E-08 | 4 | 2.9 |
| 1200 | 1.2E-08 | 8 | 4.1 |
| 1200 | 1.2E-08 | 32 | 8.1 |

## 7.3 Experimental details

The laboratory techniques used in the production of specimens for the kinetic investigations is provided herein. The furnace operation was detailed in Standard Operating Procedures constructed for both the carburization/saturation and the aging treatments conducted in this project. The procedures were followed in a step-wise fashion to assure consistency and to reduce the safety hazards associated with use of the RF furnace.

### 7.3.1 Thermal processing of specimens

The procedure for specimen preparation to obtain the precipitation rate data is described below:

1) Out-gas specimen by vacuum heating to remove interstitial oxygen and nitrogen.

2) Bring specimen to carburization/saturation temperature.

3) Produce carbide coatings by gas-phase reaction.

4) Dwell at temperature to load the matrix with interstitial carbon.

5) High-speed gas-assisted quench to room temperature.

6) Remove section and conduct metallographic examination and image analysis.

7) Machine off excess coating and the adjacent fine grain region.

8) Elevate to saturation temperature and equilibrate to re-invoke the single-phase solid solution.

9) Rapid quenching to one of the selected aging temperatures, "$TA_i$".

10) Dwell for a selected time at $TA_i$ to invoke the growth of $Ta_2C$ precipitates.

11) High-speed gas-assisted quench to room temperature.

12) Perform metallography to determine the precipitate width after aging.

No more than one aging step was performed on a specimen. This assured that the same initial condition of super-saturation was provided at the onset of each aging treatment. An illustrative representation of this processing strategy is shown in Figure 20. A schematic representation of the reactor is presented in Figure 21.

The carburization/saturations were conducted under a 3.7 torr system pressure with 0.250sccm total flow (240.0 sccm argon and 10.0 sccm methane). A gas jet nozzle directed at the specimen provided delivery of the quench gas.

Figure 20. Graphical description of experimental matrix of processing temperatures used in this campaign. The indicated values of TA-*i* are the aging temperatures at which precipitate growth was surveyed. Note that according to the phase diagram construction, the degree of supersaturation is the same at each aging temperature.

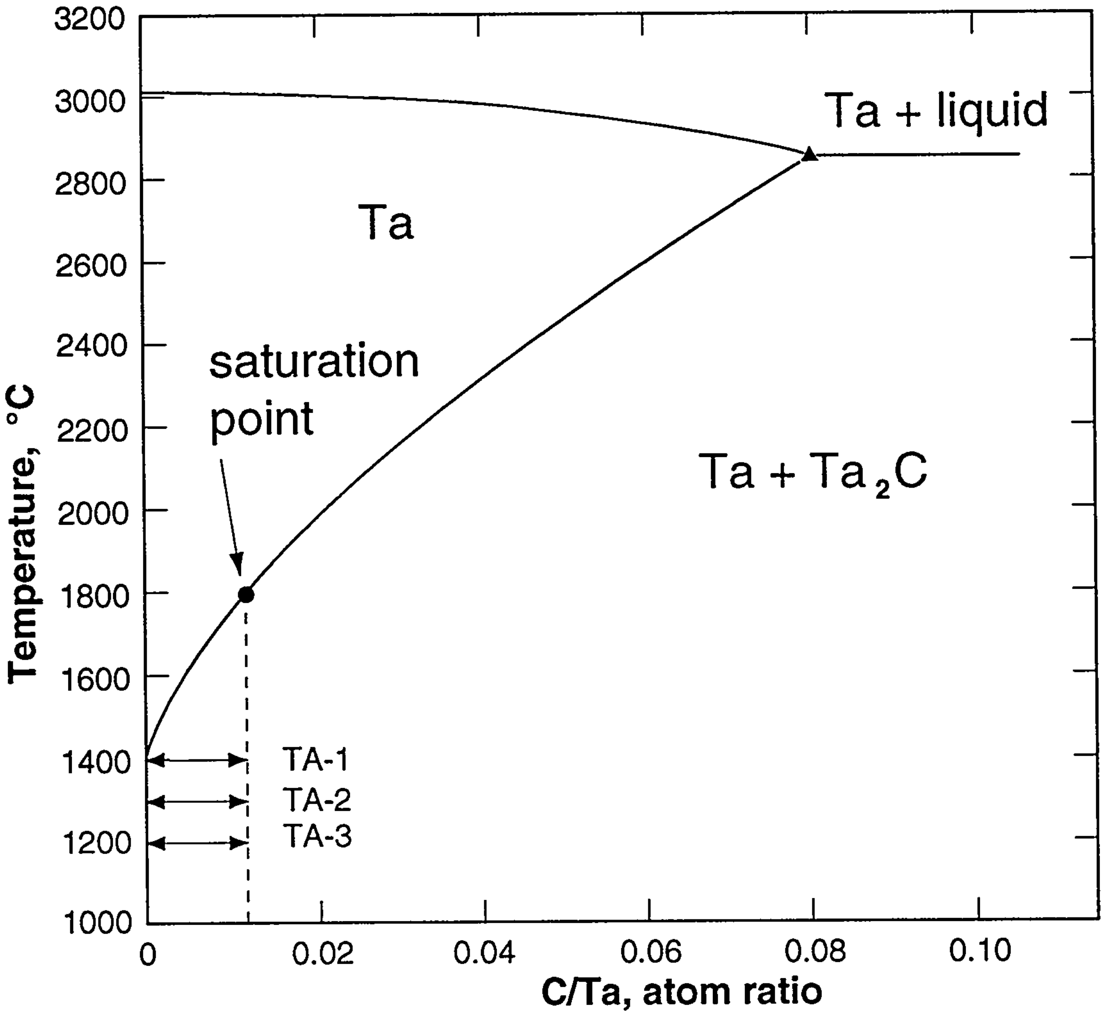

Figure 21. Schematic representation of the specimen arrangement within the reactor. Scale is approximately 2:1. A 0.5cm I.D. quartz tube was placed concentrically around the graphite fixture. A gas jet nozzle (not shown here) was aligned for direct flow of the quench gas into the quartz tube.

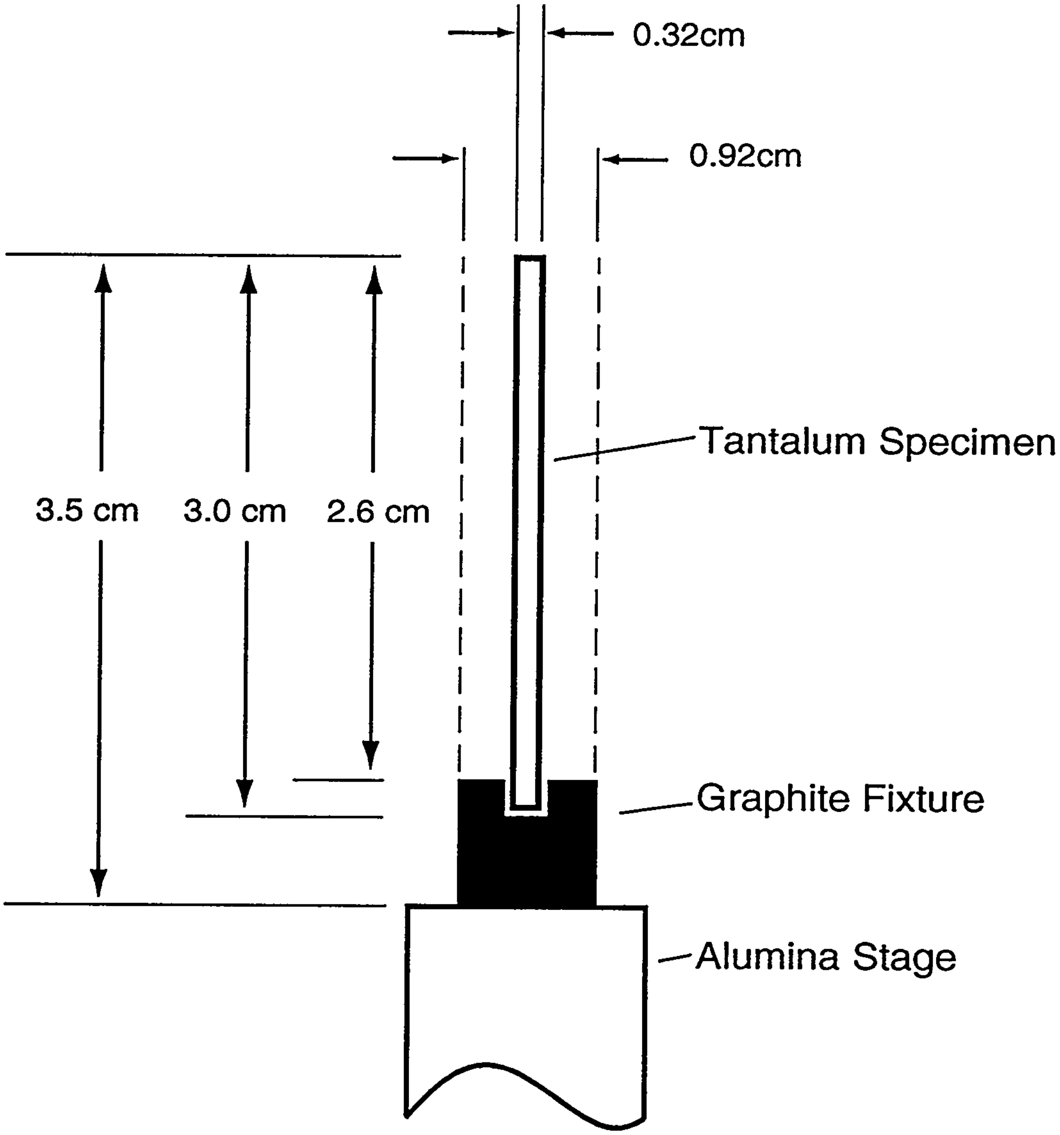

### 7.3.2 Metal finishing operations

The high-purity tantalum specimens were cut to length using a low-speed metallographic saw with an oil-cooled diamond cutting wheel, polished to a uniform #32 finish on all surfaces, then cleaned 10min ultrasonically in acetone followed by 10min ultrasonic cleaning in isopropyl alcohol. Specimen weights were recorded and then the specimens were loaded into the reaction chamber.

After reaction the specimens were dry polished with fabric cloth to remove any pyrolytic graphite deposits and then weighed. Sections were removed from the top region and prepared for metallographic examination. Metallography was conducted to determine the coating thicknesses, confirm the nucleated condition, and determine the depth of material to be machined off prior to aging. The machining was necessary as the carbide coating extended into the adjacent fine grain region and created a zone of effectively high carbon content not representative of the equilibrium carbide content within the central region. Figure 22 shows the grain structure adjacent to the surface carbide coating in a specimen after carburization/saturation. To remove this region of fine grain structure and carbide penetration, 0.025-0.030cm was machined off the diameter of each specimen.

Due to the hardness of the carbide coating and the close machining tolerance required, a unique diamond-tipped grinding device developed at Los Alamos National Laboratory was utilized. After machining, the specimens were ultrasonically cleaned and loaded into the reactor for the aging treatments.

Figure 22. Reflected light photomicrograph of the alloy after carburization/saturation processing. Note the carbide layers at the surface and the adjacent fine grain structure within the matrix of the substrate. The material on the far right hand side is the epoxy mounting media. Adjacent to the epoxy is the TaC layer followed from right to left by the $Ta_2C$ layer and then the tantalum-based substrate with carbide observed within the matrix.

The aging treatments involved an initial 1hr soak at 1800°C to regenerate the single-phase solid solution. This assured that the system was in the supersaturated condition at the onset of aging. After the dwell time at 1800°C, the furnace temperature was dropped to the aging temperature and held for a prescribed aging time. After the elapsed time, the specimen was rapidly quenched to room temperature. The gas composition during this operation was 3.7 torr pressure of pure argon at 0.250sccm flow.

### 7.3.3 Quenching technique

A theoretical treatment was conducted to determine a quench rate for this study. It was determined by both the subsequently presented calculations and experimental verification that the carbon would be removed from the solution as nucleated carbide inclusions over all practicable quenching rates.

This calculation involved a technique described by Atkins[93] in which diffusional distances are estimated over non-constant temperature conditions. This was applied to determine a mean diffusional path length for the interstitial species, carbon, over intervals of the elapsed cooling time. This revealed that the half-length between nuclei was a feasible diffusional distance during the higher temperature interval of the 1800-900°C/6.7sec cooling. Only the time required to reach ~1313°C, the initial 3.15sec of cooling, was considered in this numerical treatment.

The analysis involved separating the recorded cooling curve into intervals less than 0.5sec. An average temperature was associated with each time increment, and a diffusional path was estimated using the formula presented by Atkins. Then, the sum of the diffusional lengths was compared to the half-length between the nucleated particles. The premise was that if the diffusional path was at least equal to the distance between nuclei, then the carbon could have theoretically been removed from solution to an effectively complete degree. The data extracted from the cooling curve for a specimen cooled at a rate of 1800-900ºC/6.7sec are presented in Table 9.

A typical inter-nuclei distance is 3 microns as evidenced in Figure 23 which shows the microstructure in the quenched condition. Therefore, a typical half-length (nominal diffusional path) is 1.5 microns. Taking a diffusion coefficient for the average temperature in each of the above intervals, the technique described by Atkins has been applied:

$$< X > = \int_0^{\infty} x\, e^{-(x^2)/(4Dt)}\, dx = 2(Dt / \pi)^{1/2}$$

where < X > is the mean distance over which the intersticial particle diffuses over time. This distance must be at least equal to the half-length between nuclei to acheive the necessary condition for complete carbon depletion during quenching. The diffusion coefficient for each temperature was calculated from the most accepted source, Powers and Doyle. The calculated incremental diffusional paths are shown in Table 10.

Table 9. Cooling rate data for the numerical analysis of the interstitial diffusional path length during cooling.

| Initial Temp. | Final Temp. | Temp. Average | Time Increment |
|---|---|---|---|
| 1800 | 1725 | 1763 | 0.45 sec |
| 1725 | 1665 | 1695 | 0.45 sec |
| 1665 | 1530 | 1598 | 0.45 sec |
| 1530 | 1455 | 1493 | 0.45 sec |
| 1455 | 1395 | 1425 | 0.45 sec |
| 1395 | 1335 | 1365 | 0.45 sec |
| 1335 | 1290 | 1313 | 0.45 sec |

A theoretical diffusional path of 0.002cm was calculated as the summation over the significant, higher temperature stage of the quenching. The half-length between nuclei is an order of magnitude less than the calculated diffusional path.

Therefore, it is feasible that the carbon could have completely been removed from the supersaturated solution during cooling at this rate and that the carbon in the system was completely accounted for in the form of the carbide nuclei.

Figure 23. Micrograph of a typical specimen quenched from 1800°C, the carburization/saturation temperature used in this campaign.

Table 10. Data obtained in numerical analysis of interstitial diffusional paths. Values of $D_o$ = 0.0061 and $E_{ac}$ = 38510cal were taken from Powers and Doyle for the calculation of diffusion coefficients at the selected temperatures.

| time (sec) | AVE. Temp(C) | AVE. Temp(K) | Diffusion coefficient $cm^2/sec$ | X (path in cm) |
|---|---|---|---|---|
| 0.45 | 1763 | 2036 | 4.48E-07 | 5.07E-04 |
| 0.45 | 1695 | 1968 | 3.22E-07 | 4.30E-04 |
| 0.45 | 1598 | 1871 | 1.93E-07 | 3.33E-04 |
| 0.45 | 1493 | 1766 | 1.05E-07 | 2.45E-04 |
| 0.45 | 1425 | 1698 | 6.73E-08 | 1.96E-04 |
| 0.45 | 1365 | 1638 | 4.43E-08 | 1.59E-04 |
| 0.45 | 1313 | 1586 | 3.01E-08 | 1.31E-04 |
|  |  |  |  | SUM=0.00200 |

An effort was conducted to elucidate the time rate of transformation for the generation of $Ta_2C$ precipitates during cooling. A series of progressive cooling rates were conducted on otherwise identical carburized/saturated specimens. The cooling rates from 1800-900°C were surveyed using the two-color pyrometer linked to a strip chart recorder. To acquire high-precision cooling rate data for the initial stages of cooling, the range of the chart recorder was set to 900°C full scale. The study involved six cooling rates varying from 18.5sec to 1.7sec from 1800°C to 900°C.

Over this temperature range, the principle mechanism of heat loss is radiative relating to the fourth power of the absolute temperature. Therefore, the cooling rate dropped off exponentially with temperature as was observed in the recorded cooling curves. The interior wall of the furnace was lined with graphite felt to enhance radiative heat loss. The variations in cooling rates were obtained by delivery of a gas jet of room temperature helium directly onto the specimens. By changing the helium flow rate through the jet nozzle, variations in specimen cooling were affected. The gas delivery system was synchronized with the furnace controller so that the gas flow was initiated simultaneous to the termination of furnace power. Once the furnace power was discontinued, the radiative heat loss caused immediate specimen cooling. The conductive heat loss due to helium gas contact accelerated the cooling rates and provided for the series of cooling rate variations.

### 7.3.4 Mass spectrometry

In an ancillary study, mass spectrometry of the furnace ambient gas was conducted to acquire further carburization processing information. To establish background corrections due to contributions from the unreacted gas and from possible methane decomposition within the mass spectrometer, the gaseous speciation was characterized for the methane-argon mixture prior to furnace heating. The oxygen, hydrogen, and nitrogen signals were all below the detection limit for the instrument. A trace amount of hydrogen was detected in the system and is reflected as a background correction.

The mass spectrum was again surveyed for 15min immediately after the system was elevated to 1800°C. The results are presented in Table 11.

The specimen processed during the mass spectrometry gained 0.0060gm in 19.03hr carburization time. The specimen weight change was related to the addition of carbon and correspond directly to the amount of methane consumed during the carburization. The mass spectral analysis presented the amount of methane reacted in real time via the partial pressure of hydrogen as a reaction product. However, due to the nonlinear time-rate of the carburization reaction, mass spectral data could not be directly correlated to the total moles of decomposed methane.

Although data on the insitu generation of hydrogen could be quantitatively extracted from the mass spectrum, data would need to be surveyed over the complete elapsed time of carburization. The moles of decomposed methane could then be determined through integration over the total elapsed time.

The moles of methane per unit volume of reactant gas was calculated for the initial stage of carburization based on the measured hydrogen partial pressure during that time. The methane decompositional reaction on the specimen surface can be expressed as

$$CH_4 + Ta \Leftrightarrow TaC + 2H_2$$

The above equation is valid for the initial stage of carburization where the assumption can be made that the intermediate surface phases are absent.

Table 11. Gas phase speciation as determined by mass spectrometry during carburization of tantalum. The total system pressure during the analysis was ~4 Torr. The flow rate was 0.250sccm.

| SPECIES | PARTIAL PRESSURE |
|---|---|
| OXYGEN (DIATOMIC) | $1.0*10^{-3}$ |
| NITROGEN (DIATOMIC) | $1.5*10^{-3}$ |
| HYDROGEN (DIATOMIC) | $2.1*10^{-4}$ |
| ARGON | 0.95 |
| METHANE | BALANCE |

Based on the mass spectral data acquired at the onset of carburization, $\overline{P}_{H_2} = 2.1*10^{-4}$. $\therefore$ the decomposed methane corresponds to $\overline{P}_{\text{consumed } CH_4} = 1.05*10^{-4}$, the partial pressure associated with the methane removed from the system via reaction with the tantalum surface.

The total moles of methane decomposed during the carburization is a function of the processing time and system pressure.

$P_{\text{total}} = 3.7$ torr, $\therefore$ based on assumed ideal behavior for the gaseous mixture:

$(3.7/760) * 22.4 \text{ liters/moles} * 1.05*10^{-4} = 1.15*10^{-5}$ moles

This is the amount of decomposed methane *per liter* of gas flowing through the system during the initial carburization reaction.

Due to the inherent characteristics of induction heating, the tantalum part, which was coupled to the radio frequency, was the only component in the system at the selected elevated temperature, and therefore the methane decomposition could be exclusively associated with the surface reaction with the specimen as described above.

## 7.4 Specimen examinations

Although electron microprobe was used to characterize the composition of C-sat.Ta alloys used in the performance testing, it was realized that due to the fine microstructures produced in quenched specimens, microprobe analysis was not appropriate. An explanation is provided which describes the instrumental limitations of this analytical technique.

### 7.4.1 Relevant limitations of electron microprobe for examination of quenched specimens

In quenched specimens, the precipitate diameters and their adjacent matrix regions were in the order of a single micron. Point counts on either the matrix or the precipitates could not be accomplished without potential beam interactions within adjacent phases. This analytical limitation is related to the electron beam penetration depth which dictates the spatial resolution for the material.

The spatial resolution for each phase in the system has been calculated using the Kanaya-Okayama expression presented below:

$$R = 0.0276A(E_o)^{1.67}/(\rho Z^{0.889})$$

where R is the spatial resolution, $\rho$ is the substance density, $E_o$ is the accelerating voltage, and Z is atomic number. The calculated spatial resolutions for the relevant system substances appears in Table 12.

Table 12. Calculated spatial resolutions for electron probe microanalysis of phases in the tantalum-carbon alloy system.

| Substance | Spatial Resolution (microns) |
|---|---|
| $Ta^o$ | 0.307 |
| $Ta_2C$ | 0.313 |
| TaC | 0.321 |

As stated, the microprobe was used to identify the stoichiometries of the carbon phases. This allowed for the TaC and $Ta_2C$ layers to be distinguished on reacted specimens. The minimum detectable limit (MDL) for carbon in tantalum is affected by relatively high absorption of the incident electrons by tantalum.

This instrumental limitation is encountered for cases in which quantitative data are required on systems having elements with large differences in atomic numbers. The MDL for carbon in the tantalum-carbon alloy system was calculated from the Ziebold expression[94]:

$$C_{MDL} > 3.29 \cdot a/[(tP(P/B)]^{0.5}$$

where 'a' is the Ziebold correction factor, specific to the matrix substance (tantalum). The collection time is 't', and 'P' is the pure element counting rate. The peak/background ratio for the signal appears as the term P/B.

Based on this generalized calculation, a nominal value for $C_{MDL}$ is 0.04 wt %. However, this value neglects any beam contamination due to a partial pressure of carbon or carbon containing species in the sample chamber. A practical value for $C_{MDL}$, assuming maximum vacuum operation, is more likely an order of magnitude greater (~0.4 w/o).

### 7.4.2 Application of optical metallography and computerized image analysis

Due to the inapplicability of the microprobe, optical metallographic techniques and computerized image analysis were employed. The author has developed relevant experience through previous metallographic examinations conducted on carbon-tantalum alloys produced by a number of different procedures including both gas phase and packed bed carburization as well as coating deposition techniques.

This included examinations of materials produced at Battelle Columbus Laboratory, Lawrence Livermore National Laboratory, Ceradyne Inc., Ultramet Inc., and Thermal Technologies Inc.

In the present work, image analyses were conducted on specimens in the quenched condition to characterize the microstructure with regard to carbide nucleation. The slow cooled specimen was examined by image analysis to establish the carbide content after equilibrium cooling. The aged specimens were examined by optical metallography to extract precipitate width data.

### 7.4.3 Examination of the slow-cooled specimen

The slow-cooled specimen was examined in the stain-etched condition, and the reflected light images were taken with dark field illumination. A reflected light photomicrograph of this specimen appears in Figure 24. The cooling rate of 2°C/min was considered sufficiently slow for the specimen to retain equilibrium during cooling. Based upon this assumption, all the carbon came out of solution and created the maximum area fraction of carbide possible for a specimen saturated at 1800°C.

Although no crystallographic orientation between the hexagonal $Ta_2C$ structure and the bcc tantalum matrix can achieve complete coherency, an orientation relationship has been well established in crystallographic investigations by Dahmen[95]. In that work, precipitates of $Ta_2C$ carbide within a tantalum matrix were observed to always establish a near parallel orientation between the close packed planes.

Figure 24. Micrograph of the internal region of the slow cooled specimen examined metallographically and by image analysis.

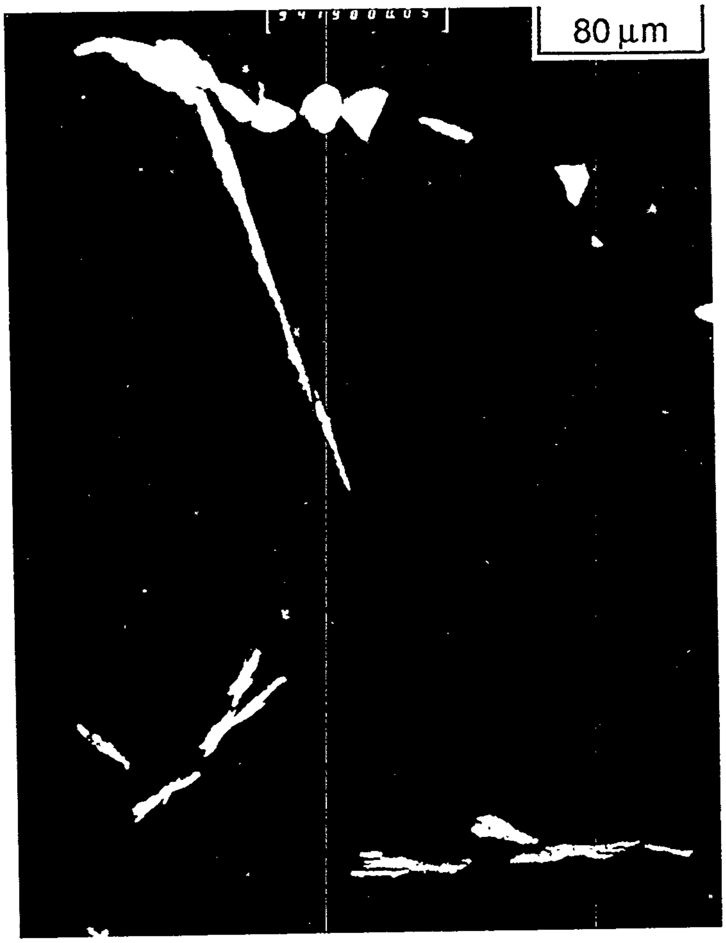

Based on interpretations of matrix/precipitate composite diffraction patterns, Dahmen reported that the close packed directions deviated a single degree at the interface. Metallographic examination of the slow cooled specimen revealed that the elongation of intragranular precipitates proceeded normal to the faceted planes. This indicates that the faceted planes observed in the intragranular precipitates were in fact crystallographically semi-coherent interfaces. It follows then that the observed directional growth was associated with migration of the less coherent interfaces. This explains the observation of numerous intragranular carbide inclusions with aspect ratios greater than 10:1.

Additional views of the microstructure within the slow cooled specimen are provided to illustrate this metallographic observation (see Figure 25). These micrographs show the spheroidal morphology of the precipitates along the grain boundaries and the semi-faceted inclusions grown within adjacent grains. The grain boundaries appear towards the left of each view (distinguished by the arrows). Note that the precipitates within the grains have a more faceted morphology.

The slow-cooled specimen was comprised of 0.0142 area/volume fraction precipitates. This information was then used to calculate the system molar composition. Then, based on the assumption that the alloy was a single phase material at the processing temperature (1800°C), and that the system had reached the equilibrium solubility at that temperature, the carbon content indicates the solubility limit at 1800°C.

Figure 25. Additional micrographs of the slow cooled specimen. The grain boundaries appear towards the left of each view (distinguished by arrows). Note that the precipitates within the grains have a more faceted morphology than those at the grain boundaries.

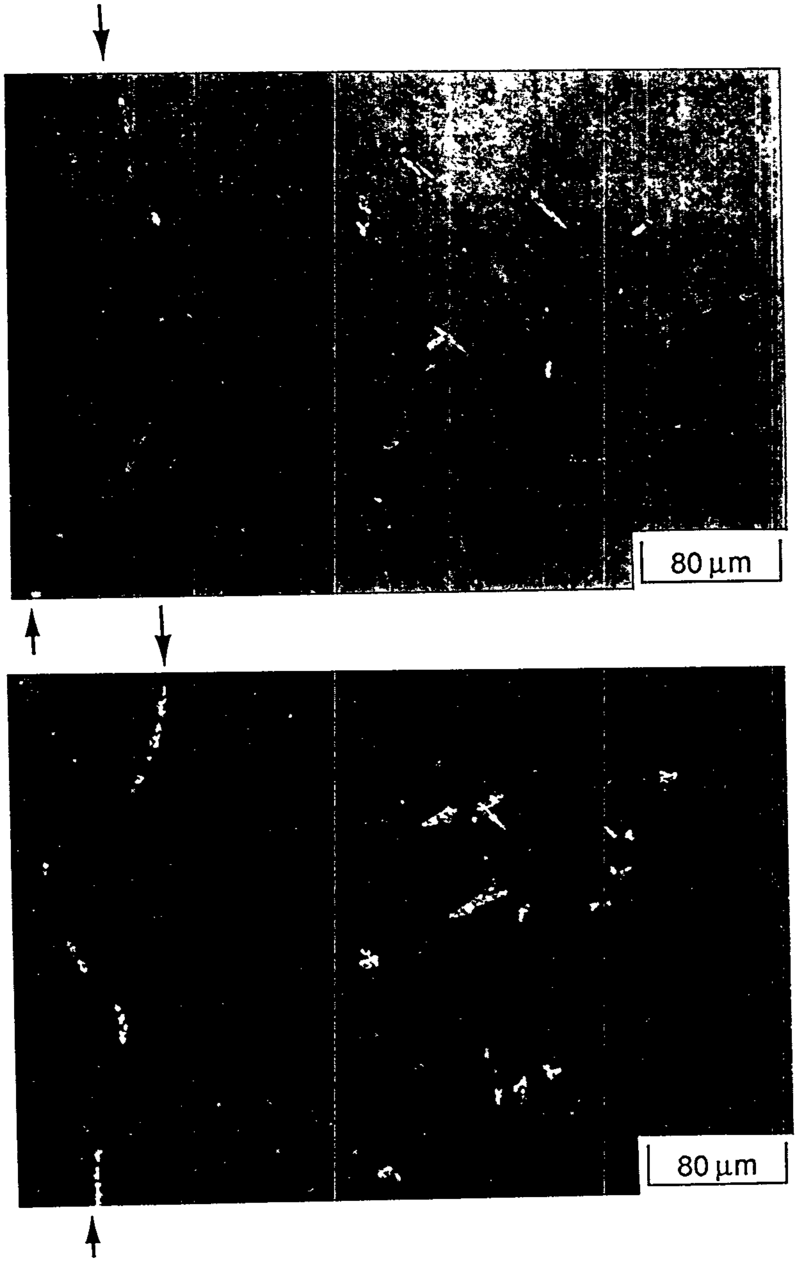

The calculations are provided here:
Normalizing the datum for a $1.0 cm^3$ sample, the volume fraction carbide data provides: $0.0142 cm^3$ $Ta_2C$, and $0.9858 cm^3$ Ta (matrix).

$\rho_{Ta} = 16.60$ gm/cm$^3$, $\rho_{Ta2C} = 14.95$ gm/cm$^3$
at.wt. Ta = 180.95 gm/mole, molec.wt. $Ta_2C$ = 373.9 gm/mole

$14.95 gm/cm^3 \cdot 0.0142 cm^3 = 0.212$ gm $Ta_2C$ in a $1.0 cm^3$ volume.

0.212 gm $Ta_2C$ per cm$^3$/373.9 gm/mole = 5.68E-4 moles $Ta_2C$

Therefore, the $Ta_2C$ in 1 cm$^3$ sample would consist of 5.68E-4 moles carbon and 1.135E-3 moles tantalum.

16.60 gm/mole Ta $\cdot$ 0.9858cm$^3$ = 16.36 gm tantalum/cm$^3$

16.36 gm tantalum/180.95 gm/mole = 9.04E-2 moles tantalum/cm$^3$
mole ratio carbon/tantalum = 5.68E-4/(1.135E-3 + 9.04E-2)
= 0.0062

mole % carbon = 5.68E-4/(1.135E-3 + 9.04E-2 + 5.68E-4)

= 0.62 %

The solubility limit as calculated by image analysis is in fairly close agreement with the data point at 1800°C in the construction of the solvus line by Rudy and Harmon. In that work, the solubility limit was reported as 0.011 mole ratio carbon/tantalum (1.1 mole % carbon).

### 7.4.4 Examinations of quenched specimens

To determine the fraction of carbide present in each of the rapidly cooled specimens, metallographic examinations with computerized image analyses were conducted on sections in the stain-etched condition. The image analysis was performed to determine the area fractions of carbide in two sections taken from each specimen. The area fraction data correspond to the degree of transformation and were recorded as a fractional amount of carbide by comparison to the "equilibrium cooled" specimen subjected to identical carburization saturation processing. The specimen considered to be equilibrium cooled was cooled at an extremely slow rate (2°C/min).

The slow cooling was conducted in an effort to invoke complete transformation of carbide from the solid solution phase.

Upon metallographic examination, the carbide distribution was found to be nearly indistinguishable in all of the quenched specimens. The carbide precipitate sizes were observed to be in the order of a single micron. Typical distances between the precipitates were 3-5 microns. The regions within approximately 20 microns of the grain boundaries contained no precipitates. The grain boundaries were slightly higher in carbide population than the intragranular regions. In all cases, the carbides were individually distinguished and did not combine to form platelets.

The size distribution was considerably different in the equilibrium cooled specimen in which the majority of precipitates had grown larger than 25 microns.

However, the same total area fraction of carbide was observed in all cases. Apparently, the rapidly cooled specimens were fully nucleated and had sufficient growth such that a vast population of precipitates were optically resolved. Partial transformation of the equilibrium carbide phase could not be accomplished over the cooling rates possible in this campaign. Comparison of specimens quenched at rates as fast as 1800-900°C/1.7sec contained the same area fraction of carbide as in the slow, equilibrium cooled specimen. This supports the calculations presented above.

It is noted that Rudy and Harmon quenched a specimen from 2200°C into liquid tin. They claimed a quench rate of 1000°C/sec.

Subsequent X-ray diffraction analysis confirmed the presence of $\alpha$-$Ta_2C$ with identical lattice parameters as the equilibrium phase. This confirms the absence of any non-equilibrium precursors and validates the use of the density of that phase in the molar calculations conducted on quenched specimens in the present work.

### 7.4.5 Examinations of aged specimens

Reflected light photomicrographs of the aged specimens provided the data for precipitate width which was measured directly off the micrographs using an optical loop with filar reticle. Each metallographic examination involved photographing a central core region greater than half of the total specimen cross section.

The number of images required to survey the selected field varied with magnification. The carbide precipitate width measurements were taken only within the grain boundary fields. In surveying the optical field, care was taken not to count the fused precipitates. The fused precipitates form from the abutment and combination of adjacently growing singular precipitates. These combined precipitates are typically larger and can be identified by their discontinuous edges. Width measurements were taken only from singular precipitates with continuous curvature.

An extensive central region of each specimen was metallographically surveyed in two sections removed from each specimen. The metallographic region surveyed in each section encompassed a central core of half the total specimen diameter. This field of view is schematically represented in Figure 26. The two sections were separated by a minimum longitudinal distance of 0.318cm to assure that they displayed separate regions of the microstructure.

The microstructure of an aged specimen (8hr at 1400°C) is provided in Figure 27. Note the grain boundary delineation by carbide precipitates.

## 7.5 Results from specimen examinations

Quantitative data on the materials behavior was extracted from metallographic examinations and chemical analysis. The information is presented separately for the examinations of carburized/saturated specimens and for specimens in the aged condition.

Figure 26. Schematic representation of field surveyed in the metallographic examinations of aged specimens. The squares represent the region covered with individual micrographs. The actual number of photographs required to compass the central core varied with the magnification of the images.

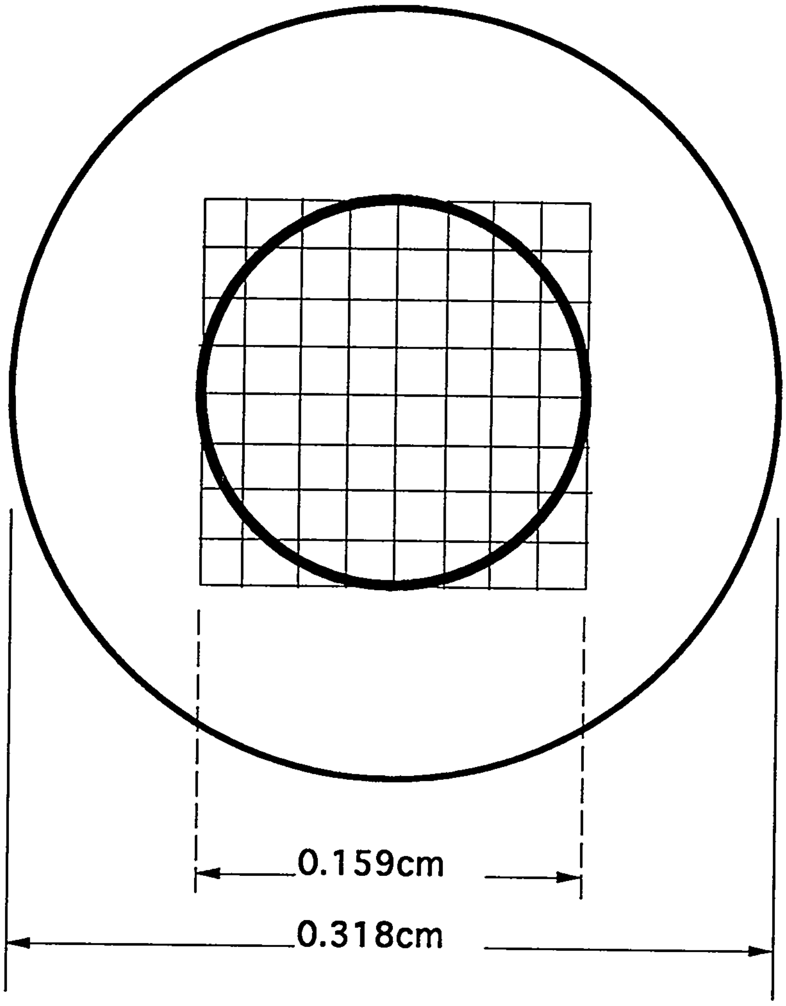

Figure 27. Microstructure within a specimen after aging for 8hr at 1400C. Note the delineation of the grain boundary by carbide inclusions.

### 7.5.1 Results from specimens examined in the carburized/saturated condition

To verify the exact carbon content within the specimens after saturation processing, three specimens were submitted to Leco corporation, St. Joseph MI, to be analyzed on the state-of-the-art Leco model CS-444 "Carbon Determinator". To assure that no carbon contribution was present from coating or localized penetration zones into the substrate, the materials were first machined down from 0.318 to 0.288cm diameter. Metallographic examinations confirmed that the remaining material was of a uniform nucleated microstructure.

The mean value for carbon composition was reported to be 0.997 mole% carbon with a standard deviation of 0.015 mole%. This value falls between the value acquired by image analysis in the current work and the value reported by Rudy and Harmon. This value was taken to calculate the $\Delta X_o$ term in the Porter and Easterling precipitate growth model.

It is worth noting that the high precision value for carbon composition establishes the correct placement of the solvus curve at 1800°C to be at 0.997 mole % carbon.

Another rigorous image analysis campaign was conducted on several of the specimens quenched from the carburization/saturation process. The cooling rates varied between 1800-900°C/16.7sec to 1800-900°C/1.7sec. The area fractions of carbide in the quenched conditions were determined to be virtually identical to that of the slow cooled specimen. This revealed that the completely nucleated condition could not be suppressed over all practicable quenching rates.

Image analysis examination was conducted on all the specimens proceeding to the aging part of the campaign to confirm that they had similar microstructures and were in the fully nucleated condition prior to the subsequent processing treatments. The consistent area fraction of carbide was taken as confirmation of a fully nucleated condition and established that all samples used in the aging experiments were of initially identical constitution. Data acquired from the metallographic examination of quenched specimens are presented in Tables 13 and 14.

Nominal surface areas were used in the calculation of carburization times. True surface area reflects surface topography and texture effects. Therefore, microscopic details greatly increase the true surface area. Since the carburization is a surface reaction, the extent to which a specimen is carburized is proportional to the amount of exposed surface area. To eliminate any associated problems, all specimens were prepared to a precise #32 finish which provided a uniform surface condition.

Several insights are made by comparing the observed layer growth with the calculated values. First, the measured values reflect variances in coating thicknesses. This is most significant with regard to the $Ta_2C$ layer. The $Ta_2C$ layer was adjacent to the metal substrate, and thicknesses varied over a range of ~19% depending on localized penetration depths. This is speculated to be an artifact of orientation relationships. The carburization reaction, and hence the penetration of the reaction zone, can be expected to proceed at slightly different rates depending upon the crystallographic plane exposed to the surface.

Table 13. Coating thicknesses recorded from specimens carburized at 1800°C. Calculated coating thicknesses are included for comparison. The calculations were based on 1800°C growth rates reported by Krikorian.

| TIME CARBURIZED (hrs) | TaC COAT THICKNESS (cm) OBSERVED | TaC COAT THICKNESS (cm) CALCULATED | $Ta_2C$ COAT THICKNESS (cm) OBSERVED | $Ta_2C$ COAT THICKNESS (cm) CALCULATED |
|---|---|---|---|---|
| 11.13 | 0.0012 | 0.0040 | 0.0004 | 0.0023 |
| 14.5 | 0.0013 | 0.0045 | 0.0004 | 0.0026 |
| 16.72 | 0.0016 | 0.0049 | 0.0004 | 0.0028 |
| 17.00 | 0.0021 | 0.0049 | 0.0007 | 0.0028 |
| 17.10 | 0.0036 | 0.0049 | 0.0006 | 0.0028 |
| 17.50 | 0.0028 | 0.0050 | 0.0007 | 0.0028 |
| 17.75 | 0.0030 | 0.0050 | 0.0008 | 0.0029 |
| 18.97 | 0.0024 | 0.0052 | 0.0006 | 0.0030 |
| 19.05 | 0.0030 | 0.0052 | 0.0012 | 0.0030 |
| 19.30 | 0.0032 | 0.0052 | 0.0007 | 0.0030 |
| 19.57 | 0.0025 | 0.0053 | 0.0015 | 0.0030 |
| 20.13 | 0.0042 | 0.0054 | 0.0010 | 0.0030 |

Table 14. Weight gains during carburization of specimens prepared for use in the kinetic investigations of precipitate growth. Calculated weight gains are based on the growth rate data reported by Krikorian.

| TIME CARBURIZED (hrs) | PERCENT WEIGHT GAIN OBSERVED | PERCENT WEIGHT GAIN CALCULATED | NORMALIZED WEIGHT GAIN ($gm/cm^2$) OBSERVED | NORMALIZED WEIGHT GAIN ($gm/cm^2$) CALCULATED |
|---|---|---|---|---|
| 11.13 | 0.3138* | 0.3785 | 0.0039 | 0.0047 |
| 14.5 | NA** | 0.4335 | NA** | 0.0053 |
| 16.72 | NA** | 0.4595 | NA** | 0.0056 |
| 17.00 | 0.1512 | 0.4658 | 0.0019 | 0.0058 |
| 17.10 | NA** | 0.4759 | NA** | 0.0058 |
| 17.50 | 0.2506 | 0.4700 | 0.0031 | 0.0059 |
| 17.75 | 0.2521 | 0.4761 | 0.0031 | 0.0059 |
| 18.97 | 0.1765 | 0.4923 | 0.0022 | 0.0061 |
| 19.05 | 0.1287 | 0.3402 | 0.0016 | 0.0061 |
| 19.30 | 0.1488 | 0.4991 | 0.0018 | 0.0062 |
| 19.57 | 0.1775 | 0.5029 | 0.0022 | 0.0062 |
| 20.13 | 0.2775 | 0.5074 | 0.0034 | 0.0063 |

* Intractable pyrolytic film observed after reaction.

** Weight change during reaction not recorded.

This effect is submitted in explanation of the observed variations in $Ta_2C$ layer thicknesses. The observed variations in layer thicknesses must have been an issue in previously reported layer growth rates, specifically the Krikorian study which included the equations used to predict layer growth in the present work. The author remains dubious of the high precision in layer thickness measurements reported in previous investigations.

Considering that the coatings produced were in the order of 10μm wide, the agreement between the calculated and observed layer thicknesses are acceptable. The calculations of predicted coating thicknesses served to estimate the carburization times selected in this investigation. For that purpose, they were extremely beneficial.

In all cases, an excess coating was retained during the saturation process. The diffusion calculations for saturation processing were based on a fixed composition at the outer radial position (the coating/substrate interface). The confirmed presence of excess coating after saturation assured that the required boundary condition was satisfied. Calculated weight gains were generated from the predicted coating thicknesses again using the Krikorian expression for layer growth rates. The observed weight gains were not consistent with the calculated values. Intuitively, this could be corresponded to the variance between predicted and observed layer thicknesses. However, an additional influence is recognized: It is noted that the observed weight gains did not correlate directly with the observed thicknesses. This is attributed to the adhesion of a pyrolytic film on the specimens. Upon removal from the reactor, a deposition of pyrolytic graphite was visually observed on some of the specimens. The extent of coverage varied for the specimens prepared with no correlation found to processing conditions. An effort was made to clean the surfaces after reaction and prior to the final weighing. However, in some cases the pyrolytic film was physically entrained on the surface and was not readily removed.

The microscopic amounts of pyrolytic graphite accounts for measurable amounts of weight gains within the scale of masses being recorded.

It is significant to mention that the pyrolytic film was generated on specimens prepared by gas phase carburization (both by acetylene and methane) but was never observed in the packed-bed preparations performed in earlier stages of this campaign. It is proposed that the pyrolytic film is an artifact of the carbonaceous gas decomposing on the hot surface of the specimens but without the production of the metal carbide reaction product. This is not a relevant issue in the case of packed-bed carburization where carbon is initially presented to the specimen surface in its elemental form.

### 7.5.2 Results from specimens examined in the aged condition

Optical metallography was conducted on all specimens in the aged condition. Precipitate width measurements were taken directly off of reflected light photomicrographs. Two sections were removed from each aged specimen and the reported measurements include data collected from both sections.

The metallographic preparation involved stain-etching as described earlier. Measurements were taken exclusively of precipitates within the grain boundary regions. By surveying the grain boundary precipitates exclusively, a level of consistency was achieved within the measurements. The grain boundary carbides share similar ambient crystallographic conditions.

Crystallographic conditions within the grain boundary regions provided incoherent interfaces which induced the spheroidal morphology possessed by all surveyed precipitates.

Width measurements were taken along the elongated linear dimension of the regular spheroids. Fused precipitate combinations were not measured. It is noted that fused carbides were frequently observed in the specimen aged for 32hr at 1400°C. The occurrence of fused precipitates in this specimen can be readily understood as being a function of the extended aging treatment. Adjacent precipitates frequently became abutted and were allowed sufficient aging time to fuse. Since the fusion of adjacent carbides was prevalent in this specimen, the total number of singular carbide inclusions available for measurement was markedly reduced.

An anomalous feature was observed in the specimen aged at 1400°C for 4hr. Similar to the 32hr age at that temperature, a high population of fused precipitates were observed. This was not observed in the 8hr aging at 1400°C. As stated above, the fusion of adjacent nuclei is an understood observation in the extended aging treatment but is anomalous behavior when observed after 4hr of aging and not after the intermediate 8hr aging.

A possible explanation is submitted for the high population of fused precipitates; If the specimen aged for 4hr initially contained an atypical amount of impurities, a greater number of successful nucleation sites could have been operative. This would provide a closer proximity of growing precipitates due to their increased initial population density. Under that circumstance, an increased frequency of fused precipitates could be expected.

Figure 28 shows typical grain boundary regions in specimens aged for different temperatures at 1400°C. The micrographs illustrate the change in grain boundary precipitate size as a function of elapsed aging times. Note that the micrographs of each specimen represent a region in the order of a single percent of the total area surveyed for width measurements. Data acquired from the metallographic examinations of aged specimens are presented in Table 15. The precipitate growth behavior at each aging temperature is plotted in Figures 29, 30, and 31.

In prelude to the further discussion of results, calculated theoretical precipitate widths have been provided (Table 16) using the model presented by Porter and Easterling and the solubility data corrected by the carbon determinations conducted in this work.

The observed growth rates were less than predicted by the Porter and Easterling model. The actual precipitate growth behavior is described herein and a set of rate effecting parameters in addition to the interstitial diffusion coefficient are recognized as active.

Figure 28. Micrographs of specimens aged at 1400°C for varying times:

| View A | View B | View C | View D |
|---|---|---|---|
| 2hr aging | 4hr aging | 8hr aging | 32hr aging |

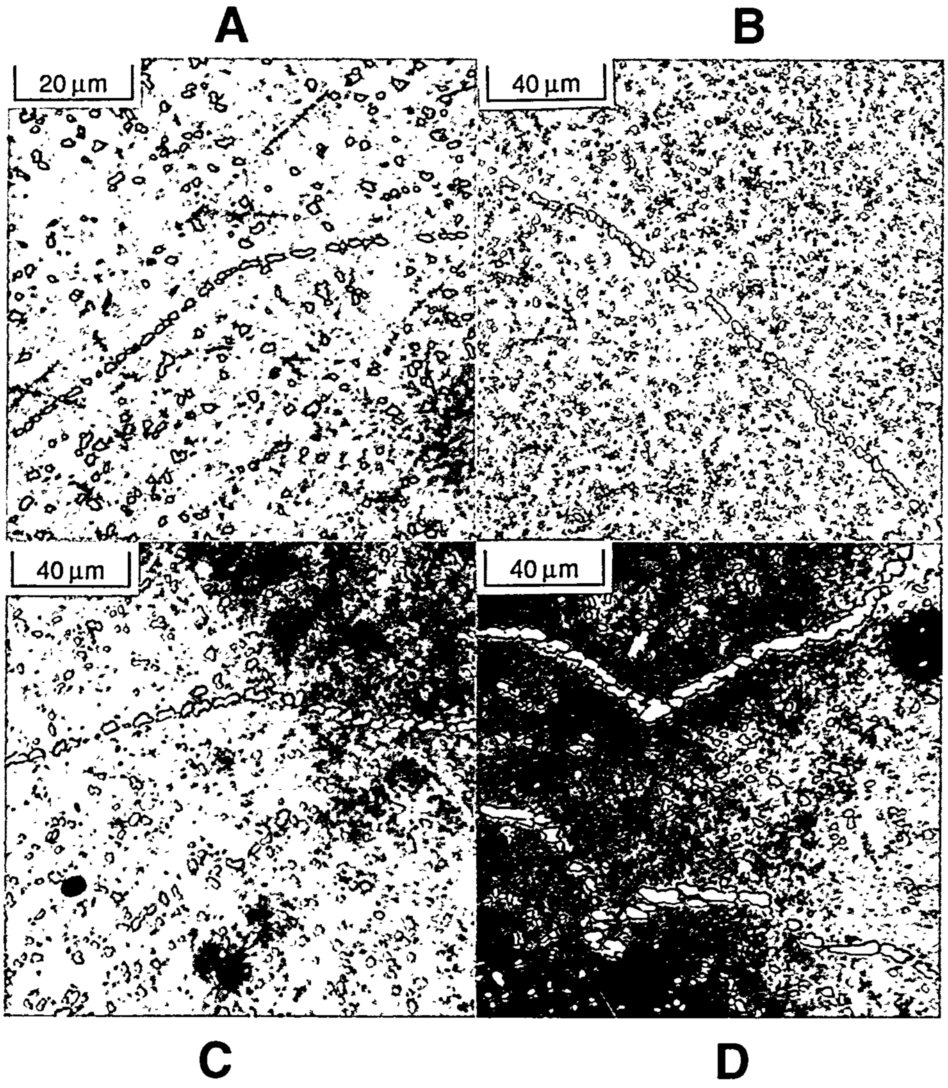

Table 15. Precipitate widths after aging treatments conducted as part of this campaign.

| AGING TIME(hrs) | AGING TEMP(°C) | PPT WIDTH(μm) | STANDARD DEVIATION |
|---|---|---|---|
| 2.0 | 1200 | 1.3* | 0.2 |
| 2.0 | 1300 | 1.2 | 0.4 |
| 2.0 | 1400 | 1.1* | 0.1 |
| | | | |
| 4.0 | 1300 | 2.9 | 0.2 |
| 4.0 | 1400 | 2.9** | 0.2 |
| | | | |
| 8.0 | 1200 | 2.1 | 0.3 |
| 8.0 | 1300 | 3.8 | 0.6 |
| 8.0 | 1400 | 4.7 | 0.7 |
| | | | |
| 32.0 | 1200 | 2.6 | 0.2 |
| 32.0 | 1300 | 4.4 | 0.5 |
| 32.0 | 1400 | 7.8** | 0.9 |

*Not all carbon accounted for as precipitated carbide.

** Larger amount of fused carbide precipitates at grain boundaries.

Figure 29. Graphical representation of precipitate width change during aging at 1400°C. The logarithmic expression is provided as an empirical description of the observed precipitate width as a function of time.

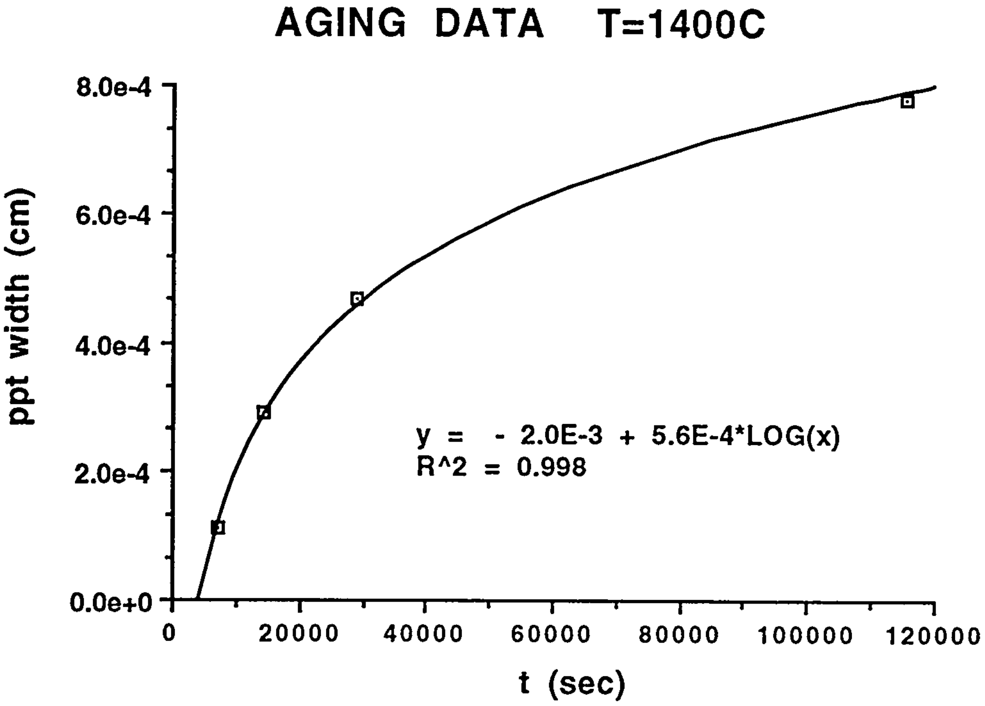

Figure 30. Graphical representation of precipitate width change during aging at 1300°C. The logarithmic expression is provided as an empirical description of the observed precipitate width as a function of time.

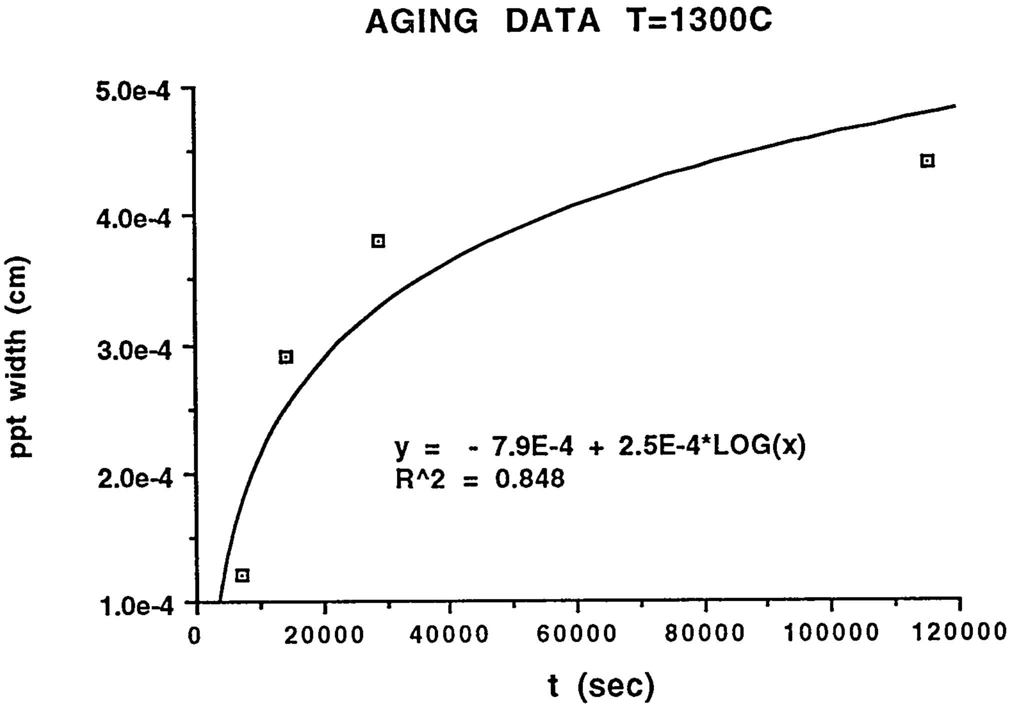

Figure 31. Graphical representation of precipitate width change during aging at 1200°C. The logarithmic expression is provided as an empirical description of the observed precipitate width as a function of time.

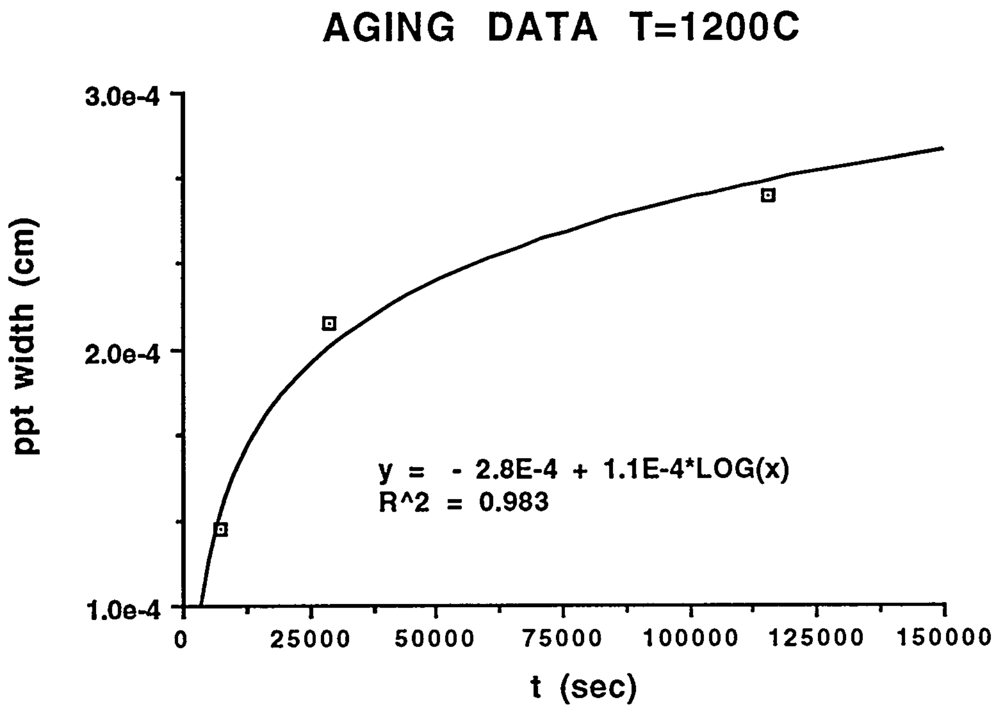

Table 16. Theoretical precipitate widths after aging as calculated with Porter and Easterling model using current solubility data. In this form of the model, the only rate term is the interstitial diffusion coefficient for carbon in tantalum.

| AGING TIME (hrs) | AGING TEMP (°C) | PPT WIDTH (μM) |
|---|---|---|
| 2.0 | 1200 | 1.8 |
| 2.0 | 1300 | 2.8 |
| 2.0 | 1400 | 4.0 |
| | | |
| 4.0 | 1300 | 3.9 |
| 4.0 | 1400 | 5.7 |
| | | |
| 8.0 | 1200 | 3.6 |
| 8.0 | 1300 | 5.5 |
| 8.0 | 1400 | 8.0 |
| | | |
| 32.0 | 1200 | 7.3 |
| 32.0 | 1300 | 11.1 |
| 32.0 | 1400 | 16.0 |

It must be recognized that the Porter and Easterling model was provided to describe general growth trends. The only temperature dependent term in the model expression is the interstitial diffusion coefficient, which is also the only appearance of a rate term in the expression.

By rearrangement of the Porter and Easterling expression, the rate term can be isolated. This identifies a quantity "$D_\Sigma$" which fits the data. The parameter $D_\Sigma$ is defined as a summation of contributing rate effects which dictate the observed growth rate:

$$D_\Sigma = [(W_{cm} \bullet (X_b - X_e)) / \Delta X_o]^2 / t_{sec}$$

The individual values for the above defined $D_\Sigma$ term were calculated for each data set and are presented in Table 17. Non-linear least squares analysis of the observations (width vs. time/temperature data) generated $D_\Sigma$ values which fit the data at each temperature. These $D_\Sigma$ values are presented in Table 18 along with the interstitial diffusion coefficients which are provided for comparison. The data for the 2hr agings were not included in the least squares analysis because of the lack of distinguishing temperature effects in those agings.

The physical significance of $D_\Sigma$ is described in terms of the sum of rate effects which influence the experimentally observed growth rate:

$$D_\Sigma \equiv \Sigma \; D_{int} + D_{GB} - D_\sigma - D_\gamma$$

where $D_{int}$ is the diffusion coefficient of the interstitial species at the specific temperature, $D_{GB}$ represents the rate effect of accelerated diffusion along grain boundaries, $D_{\sigma}$ is a rate term for transformational strain, and $D_{\gamma}$ represents interfacial effects on growth due to lattice disregistry.

Table 17. Individual $D_{\Sigma}$ values calculated for each data pair for width (cm) vs.time (sec) at temperature (K).

| AGING TIME(hrs) | AGING TEMP(°C) | $D_{\Sigma}(t,T)$ (cm$^2$/sec) |
|---|---|---|
| 4.0 | 1300 | 6.5E-9 |
| 4.0 | 1400 | 6.5E-9 |
| | | |
| 8.0 | 1200 | 1.7E-9 |
| 8.0 | 1300 | 5.6E-9 |
| 8.0 | 1400 | 8.5E-9 |
| | | |
| 32.0 | 1200 | 6.5E-10 |
| 32.0 | 1300 | 1.9E-9 |
| 32.0 | 1400 | 5.9E-9 |

Table 18. The experimentally determined rate parameters for precipitate growth reflecting least squares fit of the observations. The diffusion coefficients for interstitial carbon in tantalum have been included for comparison.

| TEMPERATURE ($^{\circ}$C) | $D_{interstitial}$ (cm$^2$/sec) | $D_{\Sigma}$ (cm$^2$/sec) |
|---|---|---|
| 1200 | $1.2\text{x}10^{-8}$ | $7.9\text{x}10^{-10}$ |
| 1300 | $2.7\text{x}10^{-8}$ | 2.6E-9 |
| 1400 | $5.7\text{x}10^{-8}$ | $6.4\text{x}10^{-9}$ |

The diffusion coefficient used in the Porter and Easterling model is for bulk diffusion. It must be considered that the grain boundaries are virtual tributaries for solid state diffusion, especially under the quenched condition which invokes excess vacancy concentrations. The growth rate of a secondary phase within the grain boundary regions is enhanced by this induced gain in overall diffusion. Measurement of the grain boundary diffusion independent of the bulk phenomenon would be intractable. Therefore a numerical value of the parameter $D_{GB}$ is not submitted.

However, the sign convention is presented with consistency to the construction of $D_\Sigma$ as the grain boundary diffusion contributes positively to overall diffusion and therefore accelerates the growth rate.

The parameter $D_\sigma$ introduced in association with transformational strain has been presented as a negative rate effect. As the lower density secondary phase inclusions grow, the localized volume changes exhibit a compressive force on the matrix, specifically the adjacent grains. The effects are orientation dependent as the individual crystals adjacent to the impinging precipitate will not compress uniformly. The numerical value of this parameter is not needed to describe the observed growth rate. The effect is incorporated into the parameter summation, $D_\Sigma$. A negative sign is associated with $D_\sigma$ as it appears in the summation. This again preserves consistency as $D_\sigma$ is considered to present a deleterious effect on growth rate.

The remaining term of the summation, $D_\gamma$ represents the change in growth rate due to lattice misfit at the precipitate/metal interface. The growth rate is controlled by crystallographic features which are pronounced through their influences on the mobility of the individual interfaces. This effect is less significant in the case of grain boundary precipitation since the highly disordered crystallographic ambiance does not promote distinct variances in mobility with respect to orientation. The precipitates within the grain boundaries are free of faceted edges which in itself reveals the absence of crystallographic effects on interface mobility.

Albeit recognized as a relatively small quantity in circumstances of grain boundary precipitate growth, it is included for completeness. By the previously defined sign convention, $D_\gamma$ is presented as a negative contribution to the growth parameter summation, $D_\Sigma$.

Based on the description of $D_\Sigma$ provided, the behavior should be independent with time. By analogy to the diffusion coefficient, a unique value for $D_\Sigma$ should correspond to a selected temperature. The analogy was extended by constructing an Arrhenius plot of the least squares values for each of the three temperatures of aging. The natural log of the $D_\Sigma$ values were plotted as a function of reciprocal temperature in Figure 32. The log of the pre-exponential factor in the Arrhenius expression is the intercept of the linear equation and the activation energy is extracted from the slope:

$$\text{Slope} = {}^{-}E_{ac}/R = -2.58E+4$$

$$\text{Intercept} = -3.39$$

Therefore, the activation energy, $E_{ac}$, for the summation of rate effects inclusive to $D_\Sigma$ is 51300cal/mole, and the pre-exponential factor for the Arrhenius equation is EXP[-3.39] =.0337. This produces a rate expression for the growth of grain boundary precipitates from the supersaturated condition:

$$D_\Sigma = .0337\text{EXP}[-51300/RT] \quad \text{cm}^2/\text{sec}$$

Figure 32. Arrhenius plot of $D_\Sigma$ values to extract activation energy and the pre-exponential factor.

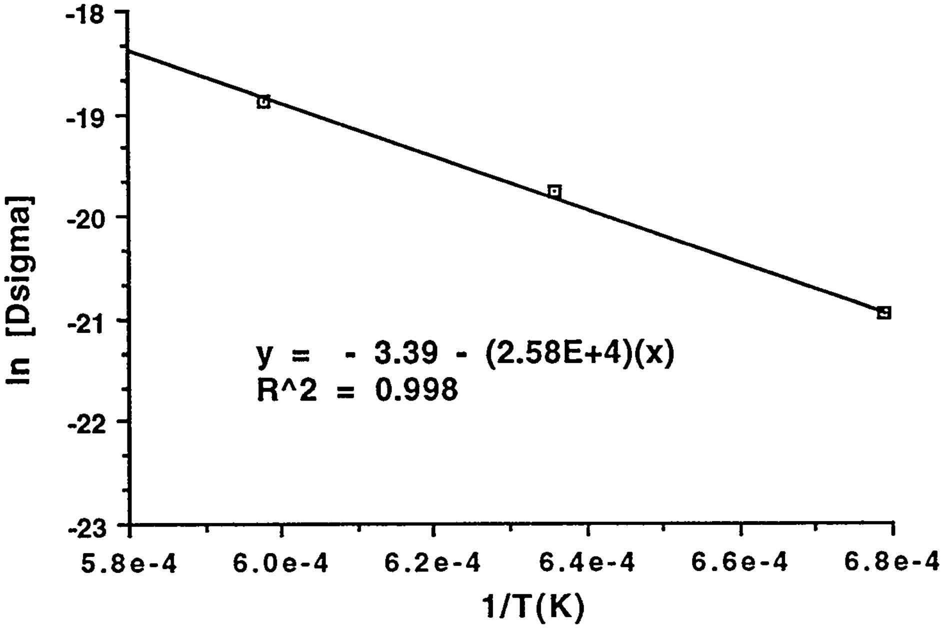

# 8.0 SUMMARY AND CONCLUSIONS

A proven methodology for the selection and evaluation of construction materials for severe applications has been developed and executed in this work. Specifically, this investigation has included the successful demonstration of an alternative construction material for use in severe metallurgical processing. The performance criteria for the alternative material were defined for the pyrometallurgical processing of plutonium. The C-sat.Ta alloy has been proven to outperform all previously tested metallic construction materials for these applications. By virtue of its corrosion resistance to high-temperature reactive gasses and molten metals, this material is suitable for a broad range of applications beyond the processing of plutonium.

Specific microstructural features of the alloy have been identified which provide the extreme corrosion resistance. These features have been identified via metallographic examinations and supporting analytical services. Grain boundary occupancy by the $Ta_2C$ phase is associated with the corrosion resistance to liquid metal. In addition, the enhanced corrosion resistance to chlorine has been attributed to the intragranular distribution of carbide inclusions. It has been demonstrated that the required grain boundary occupancy by $Ta_2C$ can be achieved only from the supersaturated condition.

The alloy development reported herein has focused on the production of these corrosion resistant attributes and included a quantitative treatment of carbide growth kinetics.

The operation of collective rate determining effects have been identified. This has experimentally proven that the precipitate growth rate is not dictated solely by the diffusion rate of the interstitial species. The interstitial diffusion coefficient is included in a collective growth rate parameter, $D_\Sigma$, which also reflects other rate determining effects.

Based on growth rate data collected over the temperature range of 1200-1400°C, an activation energy for precipitate growth at the grain boundaries has been quantified and a rate expression for growth of grain boundary precipitates has been provided:

$$D\Sigma = .0337\mathrm{EXP}[-51300/RT] \quad \mathrm{cm}^2/\mathrm{sec}$$

An expression which describes precipitate growth within the grain boundary field has also been provided. This expression is based on the equation presented by Porter and Easterling to describe precipitate growth and utilizes the parameter summation $D_\Sigma$:

$$W = \frac{\Delta X_o}{(X_b - X_e)} * \sqrt{t \bullet 0.0337\, e^{-51300/RT}}$$

where W is the width of the precipitate in cm, $\Delta X_o$ is the degree of supersaturation, $X_b$ is the mole fraction carbon in the precipitating phase, and $X_e$ is the equilibrium carbon mole fraction in the matrix at the aging temperature. The time, t is in seconds, and the activation energy appearing in the exponential is in cal/mole.

In addition, a high precision value for carbon content in tantalum was determined in this work as it was required for supersaturation measurements. This establishes the placement of the solvus curve at 1800°C in the carbon-tantalum binary phase diagram to be at 0.997 mole % carbon.

### 8.1 Discussion of carbide growth behavior

The quenched condition at the onset of aging presented an excess vacancy concentration which accelerates interstitial diffusion. Also, rapid diffusion along the grain boundaries must be considered to enhance the rate of growth for intergranular precipitates. Therefore, the carbon migration, and subsequently precipitate growth, would be assumed to be more rapid than under equilibrium conditions. This was not the observed case. Growth inhibiting effects have been qualitatively described in the construction of $D_{\Sigma}$, a rate parameter which fits the observed precipitate growth. Apparently, rate inhibiting effects counteract the growth rate enhancement due to accelerated diffusion. The observed growth had an experimentally determined activation energy 33% greater than the activation energy of interstitial diffusion for carbon in tantalum. The growth rate model presented by Porter and Easterling is now considered over simplified. The observed growth rate from supersaturated solutions can be considered as a sum of competing rate determining influences. The net effect produces a suppressed growth rate compared to the predicted growth rate of the model which considers interstitial diffusion as the exclusive rate-determining mechanism.

## 8.2 Discussion of materials performance

The most successful performance in service has been observed in C-sat.Ta with extensive grain boundary occupancy by carbide inclusions. Specimens with the most corrosion resistance had nearly complete grain boundary occupancy by the carbide inclusions. Metallographic examinations of specimens exposed to liquid plutonium at 900°C revealed grain boundary migration of the liquid metal, and subsequent intercalation was observed in the post-mortem condition. When the grain boundaries were not sufficiently decorated with carbide inclusions, the liquid plutonium was observed to solidify in place on the specimen by physical adhesion.

# 9.0 ACKNOWLEDGMENTS

This report describes a Ph.D. thesis project in materials science at the Colorado School of Mines. The author recognizes his thesis advisor, Dr. Gerald DePoorter of the CSM Metallurgical and Materials Engineering Department, for invaluable technical guidance in this work. Appreciation is also expressed to the Ph.D. thesis committee, Drs. John Hager, Nalini Mitra, Robert Witters, and William Law, for their time and effort and for teaching excellent courses which provided much of the education reflected in this work. Special thanks to committee member Joel Williams of Los Alamos who has helped through advisement in this work and in other applied materials research projects. Ramiro Pereyra of Los Alamos is recognized for developing and performing the metallographic preparations described herein. Appreciation is expressed for technical discussions with Dr. Terry Wallace of Los Alamos, and Dr. Jean dePruneda of Lawrence Livermore National Laboratory who also provided some of the materials examined in this study. Also acknowledged are Charles West and Pat Doherty of Northwestern University for the design, construction, and operation of the furnace used for processing specimens. Peter Lopez of Los Alamos is recognized for his contribution in the materials tesing and demonstration.

The author takes this opportunity to express his appreciation for the continued mentorship of Dr. Robert Sheldon of Los Alamos. The author is fortunate to have had the benefit of working with Dr. Sheldon on a number of research projects and is grateful for the insights gained through many technical discussions.

## 10.0 REFERENCES

---

1 K.M. Axler and R.I. Sheldon, J. Nuc. Mat., 187, 1992.

2 K. M. Axler, "Phase Investigations of DOR Product Materials", Presentation at the 6th Pyrochemical Workshop, Los Alamos, NM, October, 1986.

3 P.C. Lopez, T.R. Jarosch, K.M. Axler, R.A. Pereyra, G.T. Chandler, S.D. Fink, J.E. Marra, D.F. McLaughlin, "Investigation of Silicon Nitride Performance in Plutonium Pyrochemistry", Los Alamos National Laboratory Report LA-12322-MS, June, 1992.

4 K.M. Axler and E.M. Foltyn, "High-Temperature Materials Compatibility Testing of Refractory Crucible Materials: TaC, $Y_2O_3$, $Y_2O_3$-Coated MgO, and BN", Los Alamos Report LA-11586-MS, September, 1989.

5 K.M. Axler, H.D. Ramsey, R.I. Sheldon, L.E. McCurry, "Thermochemical Modeling and Verification Testing of the Plutonium Electrorefining Process", Los Alamos National Laboratory Report LA-11802-MS, April, 1990.

6 K.M. Axler, "Materials Development for Pyrochemical Applications in the Weapons Complex Reconfiguration", The 1992 Nuclear Materials Technology Division Annual Report, Los Alamos National Laboratory Report LALP-92-41, June, 1992.

---

7 K.M. Axler, "Compatibility Testing of Alternative DOR Crucible Materials", Presentation at 7th Pyrochemical Workshop, Denver, CO, November, 1987.

8 K.M. Axler, "LANL Studies of Refractory Crucible Materials" invited talk at Rockwell International Rocky Flats Plant, Golden, CO, May, 1989.

9 K.M. Axler, P.C. Lopez, G.D. Bird, A.J. Vargas, V. Dole, "Developments in Alternate Materials for Application in Pyrochemistry", Presentation at the 15th Actinide Separations Conference, Charleston, SC, June, 1991.

10 K.M. Axler, "Compatibility Studies of Alternate Crucible Materials for Plutonium Processing", Presentation at the 14th Actinide Separations Conference, Gatlinburg, TN, May, 1990.

11 L.M. Bagaasen, G.L. DePoorter, K.M. Axler, E.M. Foltyn, J.M. Espinoza, Trans. American Nuclear Soc.,62, 240, 1990.

12 K.M. Axler, Los Alamos National Laboratory Internal Report NMT-3:91-164, 1991.

13 L.M. Bagaasen, G.L. DePoorter, K.M. Axler, "Investigations of Coated Refractory Metals for Plutonium Processing", Transactions of the American Nuclear Society, 62, 240, 1990.

14 K.M. Axler, "Thermochemical Modeling of Alternate Crucible

---

Materials", invited talk at the Rockwell International Rocky Flats Plant, Golden, CO, April, 1990.

15 K.M. Axler, "The Development of Alternate Materials for Pyrochemistry - Current Investigations", Presentation at Symposium on Development and Evaluation of Alternate Materials for Pyrochemical Processing,EG&G Rocky Falts Plant, Golden CO., May, 1991.

16 K.M. Axler, "Evaluation of Candidate Materials for Application in Pyrochemical Operations", Presentation to the Joint Organization of Weapons Oriented Groups, SUBWOG-30A, Atomic Weapons Establishment, Aldermaston, England, July 1991.

17 G.L. DePoorter, K.M. Axler, R.I. Sheldon "Application of Chemical Thermodynamics for the Selection of Materials for Pyrochemical Processing", Presentation at the 94th American Ceramics Society Meeting, Minneapolis, MN, April, 1992.

18 K.M. Axler, N.J. Pugh, T.G. Chart, H. Daniels, G.S. Perry, "Calculated Phase Equilibria for the $CaCl_2$-KCl-$MgCl_2$ System" National Physical Laboratory Report DMM(D) 123, National Physical Laboratory, Teddington, UK, December, 1991.

19 W.F. Chambers and D.H. Doyle, Sandia National Laboratory Report SAND90-1703, 1990.

20 F.F. Schmidt, W.D. Klopp, D.J. Maykuth, H.R. Ogden and

---

R.I. Jaffee,"Investigation of the Properties of Tantalum and Its Alloys," Battelle Memorial Institute Technical Report WADD 61-106, May, 1961.

21 A.E.Van Arkel,Physica,4,1924.

22 K. Becker and F. Ebert, Z.Physik,.31,1925.

23 M. Schwarz and O. Summa, Metallwirtschaft,12, 1933.

24 L.P. Molkov and A.V. Chochlova, Redkie Metal.,1, 1935.

25 P.M. McKenna, Ind. Eng. Chem.,28, 1936.

26 A.E. Kovalski and J.S.Umanski, Zhur. Fiz. Khim.,20,1946.

27 H. Krainer and K. Konopicky, Berg. Huttenmann Monatsh.,92, 1947.

28 H. Nowotny and R. Kieffer, Z. Metallkunde,38, 1947.

29 J.T. Norton and A.L. Mowry, Trans AIME, 185, 1949.

30 W.G. Burgers and J.C.M. Basart, Z. Anorg. Chem.,216, 1934.

31 F.H. Ellinger, Trans ASM, 31, 1943.

32 H. Hauser & M.G. Bowman, in "Fundamentals of Refractory Compounds", Plenum Publishing, NY, NY, 1968.

33 A.L. Bowman, N.H. Krikorian, N.G. Nereson, and G.N.

Rupert, Etude des Transformations Cristallines a Haute Temperature, 205, 1971.

34 E. Freiderich, and L. Sittig, Z. Anorg., Chem, 144, 174, 1925.

35 C. Agte and H. Alterthum, Z. Techn, Physik, 11, 185, 1930.

36 G.A. Geach and F.O. Jones, Met. Abstr., 24, 366, 1957.

37 L.D. Brownlee, J. Inst. Met.,87, 58, 1958.

38 M.R. Nadler and G.P. Kempter, J. Phys. Chem., 64, 1468, 1960.

39 C.F. Zalabak, NASA Report, NASA-TN-D-761, 1961.

40 M.G. Bowman, Presentation at the 5th Plansee Seminar, Reutte, Tirol, Austria, 1964.

41 E. Rudy and D.P. Harmon, "Ternary Phase Equilibria In Transition Metal-Boron-Carbon-Silicon Systems, Part I. Related Binary Systems, Volume V. Ta-C System", Air Force Materials Laboratory Report AFML-TR-65-2, Part I,5, Wright-Patterson AFB, December, 1965.

42 F.H. Ellinger, Trans. Am. Soc. Met., 31, 89, 1943.

43 F.A. Shunk (ed), "Constitution of Binary Alloys, Second Supplement", Genium Publishing, Schenectady, NY, 1991.

---

44 M. Hansen (ed), "Constitution of Binary Alloys", Genium Publishing, Schenectady, NY, 1991.

45 R. Keiffer and F. Benesovsky, "Hartstoffe", Springer Publishing, Vienna, Austria, 1963.

46 E.K. Storms and N.H. Krikorian, J. Phys. Chem.,64, 1960.

47 K.M. Axler, Los Alamos National Laboratory Internal Report, NMT-3:92-313, 1992.

48 E. Rudy, "Compendium of Phase Diagram Data", Air Force Materials Laboratory Report AFML-TR-65-2, Wright-Patterson AFB, June, 1969.

49 W.G. Moffat (ed), "The Handbook of Binary Phase Diagrams, Genium Publishing, January, 1990.

50 E.K. Storms, "The Refractory Carbides", Academic Press, NY, NY, 1967.

51 K.M. Axler, E.M. Foltyn, D.E.Peterson, R.I. Sheldon, and W.B. Hutchinson, Journal of Nuclear Materials, 161, 1989.

52 G. Horz, K. Lindenmaier, and R. Klass, J. Less Common Metals, 35, 97, 1974.

53 F.H. Ellinger, Trans. ASM, 31,89, 1943.

54 M.K. Pochon et al., in "Reactive Metals", W.R. Clough (ed.), Interscience, NY, 327, 1959.

55 D.A. Vaughan et al., Trans. AIME, 221, 937, 1961.

56 V.I. Smirnova and B.F. Ormont, Doklady Akad. Nauk, 96, 937, 1954.

57 E.K. Storms, Los Alamos National Laboratory Report LA-MS-2674, March, 1962.

58 E. Fromm and U. Roy, J. Less Common Metals, 8,73, 1965.

59 R.A. Pereyra, Los Alamos National Laboratory Internal Report NMT-1:94-005, 1993.

60 N.H. Krikorian et al., "The Formation of Carbide Surfaces on Tantalum and Tantalum Alloys", Proceedings of the 3rd International Symposium on High-Temperature Technology, Pacific Grove, CA, September, 1967.

61 T.C. Wallace, "Diffusion & Chemical Kinetics Related to Problems in High-Temp. Chemistry of the Refractory Carbides", Presentation at UCLA, Los Angeles, CA, February, 1967.

62 G.L. DePoorter and T.C. Wallace in "Advances in High Temperature Chemistry", L. Eyring (ed.), Academic Press, NY, NY, 1971.

63 R. Resnick, R. Steinitz, L. Seigle, Trans. Met. Soc. AIME, 233, 1965.

---

64 R.W. Powers and M.V. Doyle, J Applied Physics, 30,4, 1959.

65 J.L. Snoek, Philips Research Reports, 1, 5, 1945.

66 P. Son, S. Ihara, M. Miyake, and T. Sano, J. Japanese Institute of Metals, 20, 1137, 1966.

67 G. Horz, H. Speck, E. Fromm, and H. Jehn, "Gases and Carbon in Metals, Part IX, Group Va Metals,3, Tantalum", in Physics Data, 5-9, Fachinformationszentrum Energie, Physik, Mathematik, H. Berehns and G. Ebel (ed.s), Karlsruhe, Germany, 1981.

68 R. Resnick and L. Seigle, Trans Met soc. AIME, 236, 1966.

69 D.R. Mosher, D.R. Diercks, and C.A. Wert, Met. Trans., 3, 1972.

70 D.R. Dierks and C.A. Wert, Met. Trans., 3, 1972.

71 R.K. Viswanadham and C.A. Wert, Met. Trans.,5, 1974.

72 R.W. Powers and M.V. Doyle, J. App. Phys.,28, 2, 1957.

73 J.L. Snoek, Physica, 8, 711, 1941.

74 U. Dahmen, Lawrence Berkeley Labortatory Report LBL-8661, January, 1979.

75 J.A. Leary & L.J. Mullins, Los Alamos Scientific Laboratory Report LA-3356-MS, July, 1965.

---

76 P.C. Lopez, W.J. Griego, K.M. Axler, D.L. DePoorter, R.A. Pereyra, "Current Studies in Materials Development for Plutonium Pyrochemistry", Proceedings of the International Synposium on Actinides: Processing & Materials, at the TMS Annual Meeting, March, 1994.

77 R.L Andelin et al., Los Alamos Scientific Laboratory Report LA-3631, January, 1967.

78 K.M. Axler, G.D. Bird, and P.C. Lopez, "Evaluation of Corrosion Resistant Materials for Use in Plutonium Pyrochemistry", Proceedings of the 180th Meeting of the Electrochemical Society, Electrochemical Society Press, Phoenix, AZ, 1991.

79 K.M. Axler, Los Alamos National Laboratory Internal Report, NMT-3:91-354, 1991.

80 M. Avrami, Journal of Chemical Physics, <u>7</u>, 1103, 1939.

81 V. Lappe, Sensors, 12, August 1993.

82 Shankar Krishnan, Containerless Research Inc., private communication, October, 1993.

83 Y.S. Touloukian and D.P. DeWitt, "Thermophysical Properties of Matter Volume 8, Plenum Press, NY, 1972.

84 Uli Dahmen, private communication, 1994.

85 E. Veleckis, Dissertation, Illinois Institute of Technology, 1960.

86 M.W. Mallett, and I.E. Campbell, J. Am. Chem. Soc., 73, 1951, 4850-4852.

87 A. Seiferts and A. Gotta, Z. Anorg. Chem., 172, 1, 1928.

88 T.C. Wallace and D.P. Butt, "Diffusion and Vaporization of Transition Metal Carbides as it Relates to Diffusion Coupled Carburization Processes: A Review", Los Alamos National Laboratory Report LAUR-93-2903, 1993.

89 Uli Dahmen, Lawrence Berkeley Laboratory, private communication, November, 1993.

90 T.C. Wallace, Los Alamos National Laboratory, private communication, November 1993.

91 J. Crank, "The Mathematics of Diffusion 2nd Edition", Clarendon Press, Oxford, England, 1975

92 D.A. Porter and K.E. Easterling, "Phase Transformation in Metals and Alloys second edition", Chapman and Hall, London, 1992.

93 P.W. Atkins, "Physical Chemistry", 3rd edition, W.H. Freeman Co., N.Y. pp.679

94 Scanning Electron Microscopy and X-Ray Microanalysis, J.I. Goldstein et al. (ed.s), Plenum Press, NY, 1991.

---

95 U. Dahmen, "Microstructures and Phase Transformations in Interstitial Alloys of Tantalum" Lawrence Berkeley Laboratory Report LBL-8661, January, 1979.

*U.S. GOVERNMENT PRINTING OFFICE 1995-0-673-029/7063